

ATOM CAVITY INTERACTIONS WITH
HOT AND COLD ATOMIC VAPORS

BY

ARIJIT SHARMA

A THESIS SUBMITTED TO THE JAWAHARLAL NEHRU UNIVERSITY
FOR THE DEGREE OF DOCTOR OF PHILOSOPHY

DEPARTMENT OF LIGHT AND MATTER PHYSICS
RAMAN RESEARCH INSTITUTE

BANGALORE 560 080

MAY 2012

© Arijit Sharma, 2012.

Typeset in $\text{\LaTeX}2_{\epsilon}$.

Certificate:

This is to certify that the thesis entitled “**Atom Cavity Interactions with Hot and Cold Atomic Vapors**” submitted by Arijit Sharma for the award of the degree of Doctor of Philosophy of Jawaharlal Nehru University is his original work. This has not been published or submitted to any other University for any other Degree or Diploma.

Prof. Ravi Subrahmanyam
(Director)
Raman Research Institute
Bangalore 560 080
India

Dr. Sadiqali Rangwala
(Thesis Supervisor)

Declaration:

I hereby declare that the work reported in this thesis is entirely original. This thesis is composed independently by me at Raman Research Institute under the supervision of Dr. Sadiqali Rangwala. I further declare that the subject matter presented in this thesis has not previously formed the basis for the award of any degree, diploma, membership, associateship, fellowship or any other similar title of any university or institution.

Dr. Sadiqali Rangwala

Arijit Sharma

Light and Matter Physics
Raman Research Institute
Bangalore 560 080
India

Dedicated to
Maa and Baba

Acknowledgements

I am grateful to my supervisor Dr. Sadiqali Rangwala for his guidance, encouragement, help and support in accomplishing this work. I am thankful to him for giving me the opportunity to work in his lab for my phd.

I would like to thank Prof. V. A. Raghunathan, Prof. Andal Narayanan, Prof. Hema Ramachandran and Prof. Reji Phillip for their helpful discussions and advice. In particular I am indebted to Prof. Reji Phillip for granting my request for writing the written exam at RRI. Without his kind help I would not have managed to work as a graduate student at RRI. I was extremely fortunate to have Prof. Raghunathan and Prof. Andal as my academic committee members. They have always been there to help me whenever I faced problems with my academic issues.

I would like to extend my sincerest thanks to Prof. Ajay Sood (Indian Institute of Science, Bangalore, India) who gave me the opportunity to work as Indian Academy of Sciences (IAS, Bangalore, India) summer research fellow in his group at IISc, Bangalore prior to my joining RRI as a graduate student. I would like to Dr. Ajay Singh Negi (currently Assistant Professor, IISER Bhopal, India) for his support and patience in teaching me the experiments and also explaining the nitty-gritties of life as a graduate student in India.

My special thanks to Dr. Saikat Ghosh (Reader, Satyendra Nath Bose National Centre for Basic Sciences, Kolkata, India) for his insightful comments and suggestions on cavity physics and fiber optics. A very sincere note of thanks to Prof. Guenter Werth (Johannes-Gutenberg Universitat Mainz, Germany) for teaching us the basic physics of ion trapping and helping us experimentally operate the ion trap in the cold atom-cold ion experimental set-up.

A very special note of thanks to Prof. Dmitry Budker (University of California, Berkeley, CA, USA) for giving me the opportunity to work on laser cooling of Dysprosium with Nathan Leefer (graduate student at UC Berkeley, USA). Nathan has been extremely patient in teaching me the operation of CW Dye lasers, building electro-optic modulators and iodine spectroscopy. I would also like to thank Dr. Victor Acosta (now a postdoctoral researcher, HP Labs, Palo Alto, CA, USA) and Dr. Derek F. Jackson Kimball (California State University, East Bay, CA, USA) for their collaboration on the electric field experiments with paraffin coated vapor cells which was a fruitful learning experience for us in the early days of our lab. Thanks also to Dr. Vaibhav Prabhu Desai (Scientist, Tata Institute of Fundamental Research, Mumbai, India) for his patience and help in setting up the electric field experiment at our lab in RRI. I am grateful to Byung Kyu Park (Andrew) from UC Berkeley for helping us out in the vapor cell based cavity experiments.

My sincerest thanks and regards to Ravi, Tridib, Seunghyun and Jyothi for being such wonderful lab mates and future scientists in making. I am deeply indebted to Ravi for jointly shouldering the responsibilities in the initial days of setting up of our lab. I am also deeply indebted to Tridib and Jyothi for helping me put together a consolidated effort in realizing the atom-cavity experimental set-up in the ultra-high vacuum (UHV) system assembly. I am thankful to Seunghyun for the wonderful pasta parties we had. Additional thanks to Tridib

for helping me sort out computer issues and ensuring booking of flight and train tickets at the shortest possible notice. I sincerely wish him a happy and successful married life with Harsha Mohan. I would also like to thank Ritayan, Ghazal, Daniel, Siddharth, Puneet and Gary for helping us out in our experimental efforts.

My heartiest thanks to my friends Wasim, Nandan, JayaKumar, Yogesh, Satyam, Nagaraju and Peeyush for their company. In particular I am indebted to Wasim and Nandan for being there at all times. Nandan has been with me ever since my days at IIT Kanpur. I shall never forget his logical insights even in the most non-sensical issues. I fear and admire Wasim for his ability to have healthy discussions whenever the opportunity arose. JayaKumar has been a great company in a number of trips we had together with Ravi and Nandan. I was completely overwhelmed by the warmth and hospitality we received at his house whenever we managed to visit his parents. A lot of thanks to Peeyush for inviting us to his wedding with Divya, which ensured a wonderful trip to Delhi and an amazing culinary experience at the Karims. I would like to thank Yogesh for putting up together the fight which ensured monetary as well as hostel facilities during the last year of my stay at RRI.

I also thank Anirban, Deepak, Chaithra with Amrita, Anupam, Debasish, Rajib, Arnab, Anjan, Samim, Prasad and Renu for their friendship. Sincere thanks to Deepak for discussing physics and experimental issues whenever I requested his assistance. I enjoyed the company of Anirban most when we were playing football or when his senses were completely overpowered by alcohol. A sincere note of thanks to Chaithra and Amrita for being such amazing hosts during the late night tea parties and organizing birthdays for friends at the RRI RMV hostel. Of special mention would be Soumyakanti Ganguly, former VSP at the LAMP group RRI (currently a graduate student at IISc, Bangalore),

who made life enjoyable with his amazing antiques, comments and caricatures of people in and around RRI. Additional thanks to Tarun Johri for being there to fight with Soumyakanti Ganguly whenever the situation was favorable.

I was lucky to have Brindaban, Dipanjan, Sajal with boudi, Sutirtha, Kripa, Arif, Abhijit, Antara, Radhakrishnan A.V., Alok Laddha, Abhishek Choudhuri with boudi, Dibyendyu, HariKrishna (with Mithi bhabi) and Bibhu as my seniors. I learned many scientific things as well as enjoyed a lot of discussions (both academic and non-academic) with them. I enjoyed the beer drinking sessions with Dipanjan, A. V. Radhakrishnan and Sutirtha. A special note of thanks to Arif and Antara for being there to provide sumptuous lunches and dinners on weekends. Special thanks to Abhijit for being the encyclopedia on people in academics and his delightful comments and anecdotes in this context.

I am thankful to the RRI General Workshop and the RRI Precision Workshop for their invaluable contribution in fabricating crucial parts essential for the experimental set-up and the diode laser blocks. In particular I would like to thank Mr. C. M. Ateequlla, Mr. Duraichelvan R., Mr. Narayanaswamy N., Mr. Venu V., Mr. Acchan Kunju and Mr. Dhamodaran V. My thanks to Mrs. Sujatha S. of RAL department for technical assistance in electronics. She has been patiently handling all electronics issues whenever required. I would also like to thank Mrs. Purnima Katti for helping us out with electronics in the very early days of our lab. A very special note of thanks to Shiva and Manju, our colleagues at the LAMP group for extending overwhelming support in every infrastructural issue we had.

I would like to thank Mr. Y. M. Patil, Dr. Meera B. M. and all the staff members of the library for their assistance and helpful attitude throughout my Ph. D. work.

I thank Mr. Krishnamaraju, Mr. Subramanya P. V., Mrs. Latha, Mrs. Harini, Mrs. Radha and Mrs. Marisa for making official matters very easy. I was glad to be the student representative of the RRI Canteen Committee along with Marisa, Prof. Dwarkanath, Mr. R. Somsekhar and Mr. Narayanaswamy N. I had the utmost attention of Mrs. K. Radha in every academic issues I had queries with. Thanks a lot to her for explaining to me the various rules and regulations pertaining to the academics at RRI.

I thank the computer section and team purchase for their assistance. I would like to thank Mr. Krishnamurthy S., Mr. Sridhar B. and Mr. Jacob Rajan for sorting out computer issues whenever the need arose. I also thank to all the hostel staff members, canteen staff members and everyone at RRI for their sincere cooperation and help. In addition I would like to thank Mr. Suresh G. B. and Mr. Sasidharan R. for helping us renovate our lab from scratch. I would also like to thank Mr. Haridass for being there whenever technical issues and faults arose with the electrical connections or we were plagued by UPS problems. In addition I would like to thank Mr. Sreedhar S. for helping us sort out air conditioning problems and repairing and renovating old non-functional emergency flash lamps.

I am grateful to beautiful RRI and RRI RMV Hostel environment and the Bangalore weather for making my stay enjoyable. I am happy to have enjoyed playing football at the RRI lawn for the last three years with my friends. It was a refreshing change from the work in the lab, although unfortunately I was stuck being the goal-keeper for almost all the games for the last two years.

I am deeply indebted to my cousins Sambit, Subha-da, Rahul, Toton, Sourav, Mou, Piu and Rumpa for being there to talk to me whenever I felt down or exhausted. A special note of thanks to Sumana for being the perfect host and a

great friend during the last few years of my stay at RRI. Sambit and Subha-da have always been there to help me out in case of any eventuality. My deepest regards and gratitude to my Dida who had been there as a constant support for me till the last day of her life. I wish she had been alive to see me graduate. I was fortunate to have the company of Toton, Sourav and Rahul whenever I went home during vacations. My sincerest thanks to all my other relatives and well wishers for their enduring support during my tenure as a graduate student at RRI.

Last, but not the least, my deepest gratitude and sincerest regards to my parents, my brother and my sister-in-law for their constant support and encouragement throughout this period. Without their support and encouragement, this work would not have been possible. I am very fortunate to have such a wonderful family who have stood by me through both good and bad times.

Synopsis

In this thesis we present experiments that investigate the interaction of atoms with resonant light utilizing an optical cavity. The cavity is envisioned as a frequency sensitive detector at low light levels. The physics of interactions between atoms (either at room temperature or in the cold regime) and optical cavities of varying finesse, in both the steady state and transient regime, has been discussed and presented in this thesis. Till date, to the best of our knowledge, detection of cold and ultracold molecules is largely destructive utilizing either trap loss mechanisms or mass spectrometry methods relying on the creation of molecular ionic species from the parent molecules, which are then subsequently detected on a channel electron multiplier (CEM) or from techniques that allow reversion of the molecules to its constituent atoms using Feshbach resonances. A cavity could enable frequency sensitive, non-destructive detection of molecular states by coupling the weak molecular fluorescence over and above the atomic fluorescence, if any, to the mode of the cavity. Experiments with cold atoms interacting with optical cavity modes is a precursor to the experiments to be done with cold molecules in the near future. The experiments reported in this thesis form the key towards our objective of utilizing the optical cavity as a low light level, frequency sensitive detector.

The first chapter motivates the study of experiments that have been reported in this thesis. A few of the long standing issues in the field of cold molecules are the techniques to synthesize molecules from cold atoms in large numbers, trapping these molecules for long enough time to conduct useful experimentation and lastly detection of cold molecules. In this context, our goal was to build a hybrid trapping apparatus that enables us to form, trap and detect molecules from cold atoms. Given the problems associated with the detection of molecules in low numbers using conventional imaging techniques such as spatial filtering, we highlight the possibility of using an optical cavity that could enable frequency sensitive detection of molecules in low numbers. We then provide a background of low atom number detection using cavities in the context of the Purcell effect. We give a very brief overview of atom cavity experiments that have been reported in literature using both hot and cold atoms. We also describe briefly the state of the art experiments that have demonstrated low atom number detection utilizing optical cavities in this context. We then provide a brief outline of the thesis and mention the physics problems that were investigated in improving our understanding of the atom-cavity system using atomic vapor at room temperature and cold atoms. The physics problems reported in the thesis are the initial experiments undertaken towards using the optical cavity as a frequency sensitive low light level detector.

The second chapter contains a review of the theoretical tools necessary for the experiments reported in this thesis. We start with the basic description of an optical cavity and introduce and explain the physical significance of the terms like finesse, free spectral range, quality factor, etc. of an optical cavity. We next discuss the physical origin of the eigen-modes of a resonator. We then introduce the concept of higher order modes that can be realized in an optical cavity and discuss origin and significance of the Hermite-Gaussian and Laguerre-Gaussian modes in this context. We then move into the atom-cavity interactions and discuss the Jaynes-Cummings model in the context of

the quantum theory of a two level atom interacting with a field of a single cavity mode. Using the Jaynes-Cummings model we describe the interaction of a single atom located at the center of a single mode cavity in both the ideal and in the dissipative regime using an analytical approach. Following this we move into the atomic physics segment for the remaining portion of the chapter. We discuss briefly the atomic properties of the Rubidium (Rb) atom and explain the origin of resolving the spectral lines of Rb using saturated absorption spectroscopy. We then describe the interaction of atoms with static magnetic fields that gives rise to Zeeman effects. We next describe atoms interacting with an external laser field that gives rise to coherent and incoherent processes. In this context we discuss the optical Bloch equations for a two level atom interacting with an external light field. Following this we discuss the AC Stark shifts that arise when the atomic energy levels are perturbed by the electric field of the external light field. We next discuss the spontaneous force that acts on an atom as a result of the incoherent process mentioned earlier. We then discuss the physics of laser cooling and optical molasses and finally conclude with the magneto-optical trap.

The third chapter is documented in the following manner. As a precursor to performing the actual experiments with cold atoms in ultra high vacuum conditions, we tried to see whether we could stimulate light from atoms in a room temperature vapor cell to couple into a cavity mode. In this aspect, we first describe the relevance and context of the experiments reported using a vapor cell placed inside an optical cavity at room temperature. We then briefly review previous research on all optical switches. In the next section we introduce the experimental apparatus, describe the cavity characterization and optical system set-up relevant for negative logic switching, follow it up with the experiments performed in relation to the negative logic switching and conclude with results and discussions. Both steady state and transient changes in the transmitted intensity are recorded for both cases of operation. Following this

we shall present the experimental set-up and results for positive logic switching and compare the results with the negative logic switching experiments discussed in the previous section. In the next section we discuss the physical process behind the operation of the switching mechanism by invoking a simple model. Finally we conclude by discussing the results of both switching experiments in the context of all optical switching utilizing a vapor cell encompassed within an optical cavity.

The fourth chapter is organized in the following manner. We introduce the context and relevance of optical cavities in exploring cold and ultracold molecule formation, cold atom - cold ion interaction and of course the rich physics that can be explored using only cold atoms itself. We next project clearly the physics goals that are of primary interest and the technological issues that need to be addressed in order to realize the stated physics objectives. In the following section we describe the design and construction of the UHV chamber housing the experiment. We point out the key components that have been incorporated to address the physics goals that we want to address. Following this is the subsection where we describe in detail the design, mounting, alignment and characterization of the optical Fabry-Perot cavity, which is the key tool for the experimental observations reported in this chapter. In the next subsection we discuss very briefly the design, construction and mounting of the thin wireframe trap that has been constructed overlapping the mode of the optical cavity. We then discuss in detail about the imaging system to detect atomic fluorescence from the MOT and light detection out of the cavity. We also discuss in detail about the characterization of the various optical elements and the respective detectors in the context of the imaging system that has been incorporated. In the following section we move into characterizing the magneto-optical trap (MOT) realized experimentally in the UHV system constructed by us and follow it up with a description of the experimental realization of coupling light from cold atoms trapped in the MOT into cavity modes.

Next we focus on the dynamics of atomic population by a periodic modulation on the MOT repumper beam as measured by the photo-multiplier tubes (PMTs) placed along the cavity axis in transmission and the spatial filter assembly to pick up fluorescence from trapped atoms in the MOT. In the next section we shall try to explain qualitatively the dynamics of the atomic population measured by the PMT along the MOT spatial filter axis by an effective simplified four level system using a density matrix approach. Following this section is we shall try to give a qualitative understanding of the dynamics of the composite atom cavity system using a simplified system of a two level atom in a cavity for the experimental observations. After the discussion on the above two qualitative models, we shall demonstrate the realization of collective strong coupling achieved in the composite atom cavity system through the experimental observation of normal mode splitting for cold atoms trapped in the MOT and located at the mode of the optical cavity. Finally we conclude by summarizing the experiments and observations reported in this chapter.

The fifth chapter is the concluding chapter where we summarize the work done in this thesis. We also project possible future aims and experimental goals that can be followed up with cold atoms using the optical cavity, in the ultra-high vacuum system, that has been extensively characterized both with and without atoms.

Publications from this thesis:

1. Cavity based all-optical switch in Rubidium atomic vapor

Arijit Sharma, Tridib Ray, Byung Kyu Park, Ghazal Sheikholeslami, Lee Seunghyun, K. Ravi, S. A. Rangwala. (*Manuscript in preparation*)

Other publications co-authored:

1. Electric-field-induced change of the alkali-metal vapor density in paraffin-coated cells

D. F. Jackson Kimball, Khoa Nguyen, K. Ravi, **Arijit Sharma**, Vaibhav S. Prabhudesai, S. A. Rangwala, V. V. Yashchuk, M. V. Balabas, and D. Budker
Phys. Rev. A 79, 032901 (2009)

2. Three-dimensional lattice of ion traps

K. Ravi, Seunghyun Lee, **Arijit Sharma**, Tridib Ray, G. Werth, and S. A. Rangwala. Phys. Rev. A 81, 031401 (2010)

3. Transverse laser cooling of a thermal atomic beam of dysprosium

N. Leefer, A. Cingoz, B. Gerber-Siff, **Arijit Sharma**, J. R. Torgerson, and D. Budker. Phys. Rev. A 81, 043427 (2010)

4. Combined ion and atom trap for low-temperature ion-atom physics

K. Ravi, Seunghyun Lee, **Arijit Sharma**, G. Werth, and S. A. Rangwala
Appl. Phys. B: Lasers and Optics DOI 10.1007/s00340-011-4726-6

Contents

Acknowledgements	vi
Synopsis	xii
1 Introduction	5
1.1 Introduction	5
1.2 Atom-cavity interactions: Purcell effect	9
1.3 Experiments on cavity QED	10
1.4 A brief introduction to low atom number detection using cavities .	11
1.5 Thesis outline	13
References	16
2 Fundamental Concepts and Theory	22
2.1 Introduction	22
2.1.1 Basic properties of a resonator	23
2.1.2 Gaussian beam properties of a spherical mirror cavity . .	28
2.1.3 Eigenmodes of a resonator	33
2.1.4 Transverse modes of a resonator	40

2.1.5	Atom Cavity Interactions	42
2.1.6	Quantum theory of a two level atom interacting with a field of a single cavity mode: The Jaynes-Cummings model	43
2.1.7	Analytical solution of the Jaynes-Cummings model for a system without dissipation	48
2.1.8	Analytical solution of the Jaynes-Cummings model for a system with dissipation	50
2.2	Laser cooling: Basics and theoretical background	59
2.2.1	Atomic properties of Rubidium	59
2.2.2	Interaction of static magnetic fields with atoms: Zeeman effect	64
2.2.3	Interaction of light with atoms: Coherent and incoherent processes	67
2.2.4	Optical Bloch equations for a two level atom	71
2.2.5	AC Stark shifts from external laser field	75
2.2.6	Spontaneous force on an atom	77
2.2.7	Laser cooling and optical molasses	77
2.2.8	Magneto-optical trap	80
	References	85
3	Cavity based all optical switching in room temperature atomic vapor	91
3.1	Experiments using a vapor cell cavity at room temperature	91
3.2	All optical switching	93
3.3	Brief overview of past research on all optical switching	96
3.4	Experimental arrangement and setup for negative logic switching	99
3.4.1	Cavity Assembly	99
3.4.2	Optical System Setup	99

3.4.3	Cavity Characterization	104
3.4.4	Optical bistability and hysteresis in negative logic switching	106
3.4.5	Characterization of all optical switching in negative logic .	109
3.4.6	Partial switching regime in negative logic	112
3.5	Experimental arrangement and setup for positive logic switching	116
3.5.1	Optical bistability and hysteresis in positive logic switching	117
3.5.2	Transient dynamics in positive logic switching	118
3.5.3	Investigation of small signal gain in positive logic switching	120
3.6	Qualitative model for estimating time constants of switching in negative and positive logic	122
3.7	Conclusion	131
References		133
4	Experiments with cold atoms in a cavity	137
4.1	Introduction	137
4.2	Experimental requirements	140
4.3	Design and construction of UHV system	141
4.3.1	Cavity alignment and characterization	147
4.3.2	Wireframe trap construction	150
4.4	Imaging system set-up for atom and cavity light detection and characterization of PMTs	152
4.5	Cold atom trap characterization	157
4.6	Why study atom cavity dynamics with cold atoms?	160
4.7	Cold atom emission into cavity modes	161
4.8	Dynamics of atomic population on MOT repumper beam switching	167
4.9	Qualitative model for estimating fluorescence decay time con- stant along MOT spatial filter assembly axis	171
4.10	Qualitative model for estimating fluorescence decay time con- stant along cavity axis	178

4.11 Normal mode splitting from cold atoms	184
4.12 Conclusion	191
References	193
5 Conclusion	200
5.1 Summary	200
5.2 Future Directions	205

1

Introduction

1.1 Introduction

The physics of cold dilute atomic gases has thrown up a range of possibilities for new types of experiments. Among these is the study of cold molecular gases. Cold molecule experiments represent the next generation of experiments in the domain of cold dilute gases. Molecular gases bring in structural complexity and therefore internal degrees of freedom to the problem of cold dilute gases. Thus, they are a necessary and nontrivial extension of the enterprise. Within the field, the experimental techniques to achieve these molecular gases are still under development. Cold molecules are nearly impossible to make using the laser cooling techniques that very efficiently cool atoms due to the non-availability of closed cycle transitions. Thus new methods need to be invented for this purpose. One major direction towards this goal is the formation of bonds between cold atoms to directly synthesize cold molecules. Lasers of suitable frequency could be used to forge bonds either between the

same atomic species (homo-nuclear molecules like Rb_2 , Cs_2 , etc.) or multiple atomic species (hetero-nuclear molecules like KRb , NaCs , RbCs , etc.). Another possible route towards the formation of cold molecules and the study of cold molecular ions is to allow interaction of cold atoms and cold ions in sufficient numbers with each other within a small spatial volume. The long range anisotropic ion-atom interaction potential is expected to catalyse formation of cold molecular ions.

Another issue dominating the study of cold molecular gases is the efficient detection of cold molecules formed from cold atomic gases. Atom detection has been established very reliably using conventional spatial filtering methods that image the fluorescence from cold trapped atoms in a MOT (magneto-optical trap) onto either a PMT (photo-multiplier tube) or a CCD (charge coupled device) camera. Absorption methods can also be implemented reliably to detect temperature and density of a cold dilute atomic gas. In contrast, detection of cold and ultracold molecules [1–14] till date, to the best our knowledge, is largely destructive utilizing either trap loss mechanisms or mass spectrometry methods relying on the creation of molecular ionic species from the parent molecules, which are then subsequently detected on a channel electron multiplier (CEM) or from techniques that allow reconversion of the molecules to its constituent atoms using Feshbach resonances.

We wanted to build an instrument capable of simultaneously creating, trapping and detecting cold molecules formed from cold atoms. Long trapping times are desirable in the context of useful experimental measurements. Cold atom preparation can be routinely achieved using standard laser cooling techniques. One could also obtain a spatially localized cloud of cold atoms in a magneto-optical trap (MOT). Typically 10^7 atoms could be trapped in a MOT with an \approx cloud size of 1mm. To generate cold hetero-nuclear molecules one needed additional atomic species of interest that could be simultaneously trapped in the same spatial region. This would generate 2×10^7 atoms over a

spatial diameter of ≈ 1 mm. Assuming that it is possible to convert 2 out of every 10^3 atoms to cold molecules, one shall end up with 10^4 molecules. This is a very small number of molecules that have been created from the entire cold atomic ensemble. Given the weak decay rates of molecular states compared to atomic dipole transitions it is very difficult to efficiently detect molecules in low numbers created from cold atoms.

The low production efficiency of molecules (typical rates of photo-association $\approx 10^3 - 10^5$ molecules per sec) leads to lower density compared to atoms in the MOT ($\approx 10^{10}$ atoms per cm^3). Hence in effect there is a lower fluorescence from the molecules (formed from cold atoms) compared to trapped atoms in the MOT. The collection of fluorescence is also limited by solid angle constraints imposed by vacuum chamber view-ports. Enhancement of signal to noise ratio (which in this case is background fluorescence from laser cooled atoms) even by spatial filtering becomes a challenge which in effect is a frequency insensitive technique. Further, the use of a spatial filter assembly would not enable the distinction between the atomic and molecular fluorescence over and above the background of the atomic fluorescence signal reaching the detector. In this aspect a cavity could possibly enhance the weak molecular fluorescence by stimulating decay along the cavity mode and thus enabling frequency sensitive detection of the weak molecular fluorescence. An additional advantage could be the realization of an optical dipole trap in the mode of the cavity allowing simultaneous trapping of the cold molecules formed with the added benefits of in-situ detection.

We envisaged the use of a Fabry-Perot cavity for the frequency sensitive detection scheme at low light levels. The cavity could be initially tuned to the reference frequency for best possible finesse. A cavity could lead to enhanced emission by a factor $2F/\pi$, where F is the cavity finesse. The idea is to stimulate emission of the photons from molecules in excited states into the cavity mode. The cavity might enable re-interrogation of molecules and a large signal to

noise ratio by selectively discriminating against the atomic fluorescence and not allowing it to get coupled to the cavity mode. This could pave the way for efficient detection of molecular states. We did not know a priori whether this method could work for molecules. Hence the first step would be to check it on atoms to verify and estimate whether this technique is efficient or not. Carefully chosen atomic transitions could either enhance or suppress emission of photons into the cavity mode. This was a key factor for investigating atom-cavity interactions with atoms at room temperature and in the cold regime.

In order to establish the protocol for detection of molecular states using the cavity, we needed to understand the dynamics of atom-cavity interactions. Towards this end, we embarked upon the experiments initiated with a Rubidium(Rb) vapor cell placed in a cavity. Exploring the atom-cavity interactions at room temperature enabled us with the requisite understanding and framework necessary to probe the interactions of laser cooled atoms placed in the cavity. The transient studies in both the room temperature and the cold regimes were motivated by the issue of detector response towards cold molecule formation, if, and when external electro-magnetic fields could be used to influence the formation of such molecules from cold atoms.

This thesis focuses on the initial experiments towards using the cavity as a frequency sensitive detector at low-light levels. As a precursor towards utilizing the cavity for detection of molecular states, experiments with atoms (both at room temperature and the cold regime) interacting with optical cavities of varying finesse are presented. These experiments have been conducted both in the steady state and in the transient regimes of atom cavity interactions. The experiments with Rubidium (Rb) atoms in a vapor cell (placed inside an optical cavity) at the room temperature were motivated by the investigation of gain/stimulated emission in such systems using an optical cavity and to investigate the possibility of using the cavity as a frequency sensitive low light level detector. We realized that the transmission of the cavity encompassing

the vapor cell could be manipulated using appropriate transitions of the Rb atom. This led to the investigations and experiments related to the all optical switching phenomena observed and reported in this thesis. The experiments with cold atoms was a natural extension of the investigations done with Rb atoms at room temperature. The experimental apparatus designed to study the simultaneous formation, trapping and detection of cold molecules or cold molecular ions is non-trivial in concept and design. The need to facilitate overlap of the cavity mode with the neutral atom trap and the molecular trapping apparatus was of prime concern to achieve and understand the above stated goal. Characterization of the optical cavity in the ultra-high vacuum (UHV) system and the investigations on the transient and steady-state dynamics of the composite atom-cavity system using a cloud of laser cooled Rb atoms (confined in a magneto-optical trap) located at the center of the optical cavity are also presented in this thesis.

Keeping in view the above perspective, a brief review to the experiments investigating atom-cavity interactions using thermal atoms as well as cold atoms is presented. The state of the art experiments utilizing optical cavities as detectors of low atom numbers are also discussed briefly in this context. A very brief outline of the thesis is included at the end.

1.2 Atom-cavity interactions: Purcell effect

The study of atom-cavity interactions gained importance after the publication of a small note by Purcell [15] in the Proceedings of the American Physical Society, 1946 where he pointed out that the spontaneous emission probability of nuclear magnetic moment transitions can be considerably enhanced when the system is coupled to a resonant electrical circuit. The physical significance of the work reported by Purcell implied the possibility of altering or enhancing the rate of spontaneous emission of atoms within a resonator when the

atoms are subject to electro-magnetic conditions having boundary conditions differing from that in free space. Thus the afore-mentioned article by Purcell became one of the most influential references in works on cavity quantum-electrodynamics (CQED) as it is one of the foremost articles on the “Purcell effect” in CQED. The spontaneous emission enhancement factor η [16] (also known as the Purcell factor) is given as

$$\eta = \frac{3}{4\pi^2} \frac{Q\lambda_c^3}{V} \quad (1.1)$$

where $\lambda_c = 2\pi c/\omega_c$ is the wavelength of the cavity field which is resonant with the atomic transition ω_a . Here c is the speed of light, Q the quality factor of the cavity and V denotes the mode volume of the cavity. An important application of the Purcell effect could be the detection of single atoms with high efficiency using cavity-aided fluorescence detection and thus count small numbers of atoms with very good resolution using either or a combination of fluorescence and absorption methods. This technique of atom detection could well be extended to the detection of molecular states where one could stimulate the molecules to decay along the cavity mode with suitable pumping schemes. The cavity would then enable frequency sensitive detection of molecular states over and above the background of atomic fluorescence (if for example, the molecules are prepared from an ensemble of cold/ultracold atoms).

1.3 Experiments on cavity QED

The first experiments in atomic physics were conducted in the 1980’s using thermal molecular [17] and atomic beams [18]. Early experiments utilized Rydberg atoms in microwave cavities. Rydberg atoms were a natural choice for the experiments in cavity QED due to their large dipole moments and the availability of super-conducting high-Q cavities allowing a strongly coupled system.

Enhanced spontaneous emission was first demonstrated in such a system [18], and in a similar setup like the one in [18] a one-atom maser was realized [20]. Experimental demonstration of inhibited spontaneous emission was also first observed using Rydberg atoms [21] after the proposal of Kleppner [22].

Experiments using single atoms in the optical domain were first realized by the group of Heinzen et al. [23]. They experimentally measured enhanced and inhibited emission rates of a thermal beam of Ytterbium (Yb) atoms traversing a confocal optical cavity. By controlling the flux of atoms traversing the optical cavity, one could attain the regime of single atoms occupying the cavity mode and this led to interesting atom-cavity effects, such as the observation of normal mode spectrum [24–26] of the composite atom-cavity system. The optical analogue of the famous one-atom maser (then dubbed microlaser) was also demonstrated in such a system [27].

The experimental realization of laser cooling [28–31] leading to the magneto-optical trapping of neutral atoms [32–36] further refined these experiments since the atoms could be delivered into smaller volume cavities in a more controlled way: by dropping them from a MOT [37] or pushing them from below in an atomic fountain [38]. The transit and even the trajectory of a single atom could be inferred from the cavity transmission signal. Trapping and cooling of single atoms for up to 3 seconds [39, 40] was demonstrated using this signal. Further an atomic “conveyor belt” [41] to guide atoms has been realized using a dipole trap formed in the cavity mode.

1.4 A brief introduction to low atom number detection using cavities

In this section we shall briefly review some of the state of the art experiments demonstrating low or even single atom detection with very high fidelity using

an optical cavity. An important quantity in characterizing cavity enhanced detection is the single atom cooperativity factor [42] $C = g^2/2\kappa\Gamma$, where g is the single-photon Rabi frequency at the peak of the cavity intensity distribution, κ is the cavity linewidth (full width at half maximum), and Γ is the natural atomic linewidth. The cooperativity factor physically signifies two important aspects of the atom-cavity system: (a) it determines the effect of a single atom on the cavity spectrum and (b) it also governs the rate of fluorescence into the cavity. For more than one atom located in the mode of a cavity, the cooperativity factor is given by $C_{eff} = CN_{eff}$, where N_{eff} [43] is the effective atomic number given by

$$N_{eff} = \int_0^L \int_{-\infty}^{\infty} \int_{-\infty}^{\infty} |\chi(\vec{r})|^2 \rho(\vec{r}) d^3\vec{r} \quad (1.2)$$

where $\chi(\vec{r}) = \sin(2\pi z/\lambda)\exp[-(x^2 + y^2)/w^2]$ defines the cavity field mode function, L defines the cavity length, and $\rho(\vec{r})$ denotes the atomic density with λ being the wavelength. For low atomic numbers present inside the cavity mode volume, single-atom physics dominates, whereas, at higher densities, multi-atom effects become important [43].

Cavity assisted atom detection can be implemented via absorption methods [44–46] or fluorescence [47–49] since the emission of light into the cavity mode is enhanced by the Purcell factor $2F/\pi$, where F is the cavity finesse. The early attempts at investigating the possibility of detection of single atoms using optical cavities were reported by Horak et. al. [42]. They suggested the possible use microcavities of sufficiently high finesse to be built around the trapped atomic ensemble to enable detection of a single atom in the trap with $10 \mu\text{s}$ of integration.

Following this protocol, M. Trupke et. al. [50] demonstrated the use of a microfabricated optical cavity, which combined a very small mode volume with high finesse to allow atoms and molecules to interact strongly with the photons in the cavity for the purposes of detection and quantum-coherent manipulation. One of the key features of their experiment was to use an optical fiber mounted

in situ with one of the resonator mirrors which enabled them to avoid sensitive coupling optics to couple light into the cavity.

Single atom detection using an optical cavity was demonstrated experimentally by Teper et. al. [51]. Here the atomic sample initially prepared from a MOT was trapped magnetically using suitable current carrying wires integrated on a chip. Using fluorescence techniques to detect atoms, they have been able to detect single atoms with 75% efficiency using $250\mu\text{s}$ of integration time. They have also demonstrated single atom detection in absorption by measuring the attenuation of the cavity transmission due to presence of atoms in the cavity mode with a resolution of about 1 atom.

In a recent work by Goldwin et. al. [52] local density measurements were performed on clouds of laser cooled ^{87}Rb atoms by dropping them through a high-finesse optical microcavity. The experimental apparatus is similar to the one described earlier in [53]. They show that effects of atomic fluctuations could be suppressed while making local density measurements on clouds of cold atoms by using the combined effects of nonlinearities and multi-atom statistics. They show that even at densities on the order of one atom per cavity mode volume, the effects of atomic shot noise are heavily suppressed. They demonstrate atom detection with fidelities in excess of 97% with $10\mu\text{s}$ of integration time which can be enhanced to reach a fidelity value of 99.9% using $30\mu\text{s}$ integration time.

1.5 Thesis outline

The work presented in this thesis includes the experimental realization of an all optical switch using a Rubidium(Rb) vapor cell enclosed within an optical cavity and design and construction of the experimental apparatus which tries to explore atom cavity interactions using laser cooled Rb atoms confined within a magneto-optical trap and located at the center of the cavity. A brief outline of

the thesis is presented in this section.

Fundamental concepts and theoretical background necessary for understanding resonator physics, atom cavity interactions and light-atom interactions are discussed in chapter 2. Here we discuss the various aspects of Fabry-Perot cavities like free-spectral range (FSR), finesse, eigen-modes and higher order transverse modes. We also discuss atom-cavity interactions using the Jaynes-Cummings model both in the ideal and dissipative regimes. We next focus our discussion on the atomic properties of the Rb atom and describe the hyperfine structure of Rubidium and also discuss the spectrum of Rb obtained by Doppler free saturated absorption spectroscopy in this context. We then discuss the optical Bloch equations for a two level atom and introduce the physics of laser cooling leading to the discussion on the magneto-optical trap(MOT).

Chapter 3 introduces the concept of optical switches and a brief review of the earlier work in the context of all optical switching is discussed. We then present our experiments on all optical switching using a Rb vapor cell enclosed within an optical cavity. We show switching realized in the negative and positive logic by manipulating the transmission of the cavity using appropriate transitions of ^{87}Rb . We investigate hysteresis effects in both positive and negative logic switching. We characterize the transient responses of the cavity transmission when an external control beam, incident from the transverse direction of the cavity axis, is modulated in intensity using an acousto-optic modulator (AOM). We explain qualitatively the origin of the two timescales associated with the transient dynamics of the system.

In Chapter 4 we present our experimental set-up incorporating an optical cavity spatially overlapping with the centers of a magneto-optical trap and an ion trap. We discuss the design and construction of the ultra-high vacuum (UHV) system in the context of the physics goals to be pursued and related technical issues that needed to be addressed. We present detailed methodology of the alignment and characterization of the optical cavity which is one

of the key components for the experiments that have been done with cold ^{85}Rb atoms. We then present the characterization of the detection apparatus (spatial filters and imaging system) for the MOT and cavity transmission. We next present our experiments related to measurement of the linewidth of cavity modes formed due to emission of photons from the cold atoms trapped in the MOT and characterization of the linewidth of these modes with respect to total number of atoms in the MOT. We then describe our experiments on the transient dynamics of the atom-cavity system by switching the MOT repumper beam. We also discuss the two models which qualitatively describe the transient responses measured by the photo-multiplier tubes (PMTs) placed after the MOT spatial filter assembly and along the cavity axis respectively. We finally demonstrate the capability of our composite atom-cavity system to enter the regime of strong coupling.

We finally conclude the thesis with chapter 5 by summarizing the contents of the entire thesis and provide future aims and directions that can be implemented and investigated experimentally using cold atoms located in the mode of the optical cavity.

References

- [1] J. D. Weinstein, R. deCarvalho, T. Guillet, B. Friedrich and J. M. Doyle. Magnetic trapping of calcium monohydride molecules at millikelvin temperatures. *Nature* 395 148-150 (1998).
- [2] S. Inouye, M. R. Andrews, J. Stenger, H-J Miesner, D. M. Stamper-Kurn and W. Ketterle. Observation of Feshbach resonances in a Bose-Einstein condensate. *Nature* 392, 151 (1998).
- [3] H. L. Bethlem, G. Berden and G. Meijer. Decelerating neutral dipolar molecules. *Phys. Rev. Lett.* 83, 1558-1561 (1999).
- [4] J. Weiner, V. S. Bagnato, S. Zilio and P. S. Julienne. Experiments and theory in cold and ultracold collisions. *Rev. Mod. Phys.* 71, 1 (1999).
- [5] E. A. Donley, N. R. Claussen, S. T. Thompson and C. E. Wieman. Atom-molecule coherence in a Bose-Einstein condensate. *Nature* 417, 529 (2002).
- [6] J. Herbig, T. Kraemer, M. Mark, T. Weber, C. Chin, H-C. Nagerl and R. Grimm. Preparation of a pure molecular quantum gas. *Science* 301, 1510 (2003).

-
- [7] S. Jochim, M. Bartenstein, A. Altmeyer, G. Hendl, S. Riedl, C. Chin, J. Hecker Denschlag and R. Grimm. Bose-Einstein condensation of molecules. *Science* 302, 2101 (2003).
- [8] M. Greiner, C. A. Regal and D. S. Jin. Emergence of a molecular Bose-Einstein condensate from a Fermi gas. *Nature* 426, 537 (2003).
- [9] C. A. Regal, C. Ticknor, J. L. Bohn and D. S. Jin. Creation of ultracold molecules from a Fermi gas of atoms. *Nature* 424, 47 (2003).
- [10] M. W. Zwierlein, C. A. Stan, C. H. Schunck, S. M. F. Raupach, S. Gupta, Z. Hadzibabic and W. Ketterle. Observation of Bose-Einstein condensation of molecules. *Phys. Rev. Lett.* 91, 250401 (2003).
- [11] J. M. Sage, S. Sainis, T. Bergeman and D. DeMille. Optical production of ultracold polar molecules. *Phys. Rev. Lett.* 94, 203001 (2005).
- [12] T. Khler, K. Gral and P. S. Julienne. Production of cold molecules via magnetically tunable Feshbach resonances. *Rev. Mod. Phys.* 78, 1311 (2006).
- [13] K. M. Jones, E. Tiesinga, P. D. Lett and P. S. Julienne. Ultracold photoassociation spectroscopy: long-range molecules and atomic scattering. *Rev. Mod. Phys.* 78, 483 (2006).
- [14] K-K Ni, S. Ospelkaus, M. H. G. de Miranda, A. Pe'er, B. Neyenhuis, J. J. Zirbel, S. Kotochigova, P. S. Julienne, D. S. Jin and J. Ye. A high phase-space-density gas of polar molecules. *Science* 322, 231 (2008).
- [15] E. M. Purcell. Spontaneous emission probabilities at radio frequencies. *Phys. Rev.* 69, 681 (1946).
- [16] Serge Haroche and Jean-Michel Raimond. *Exploring the Quantum - Atoms, Cavities and Photons*. Oxford University Press Inc., New York, 2006.

-
- [17] F. De Martini, G. Innocenti, G. R. Jacobovitz and P. Mataloni, Phys. Rev. Lett. 59 2955 (1987).
- [18] M.G. Raizen, R.J. Thompson, R.J. Brecha, H.J. Kimble, and H.J. Carmichael. Phys. Rev. Lett. 63, 240 (1989).
- [19] P. Goy, J. M. Raimond, M. Gross and S. Haroche. Phys. Rev. Lett. 50 1903 (1983).
- [20] D. Meschede, H. Walther and G. Muller. Phys. Rev. Lett. 54 551 (1985).
- [21] R. G. Hulet, E. S. Hilfer and D. Kleppner. Phys. Rev. Lett. 55 2137 (1985).
- [22] D. Kleppner, Phys. Rev. Lett. 47 233 (1981).
- [23] D. J. Heinzen, J. J. Childs, J. E. Thomas and M. S. Feld. Enhanced and inhibited visible spontaneous emission by atoms in a confocal resonator. Phys. Rev. Lett. 58, 1320-1323 (1987).
- [24] Q. A. Turchette, R. J. Thompson and H. J. Kimble. Appl. Phys. B60, 1 (1995).
- [25] R. J. Thompson, G. Rempe and H. J. Kimble. Observation of normal-mode splitting for an atom in an optical cavity. Phys. Rev. Lett. 68, 1132-1135 (1992).
- [26] J. J. Childs, K. An, M. S. Otteson, R. R. Dasari, and M. S. Feld. Normal-Mode Line Shapes for Atoms in Standing-Wave Optical Resonators. Phys. Rev. Lett. 77, 2901-2904 (1996).
- [27] K. An, J. J. Childs, R. R. Dasari and M. S. Feld. Microlaser: A laser with One Atom in an Optical Resonator. Phys. Rev. Lett. 73, 3375-3378 (1994).
- [28] William D. Phillips and Harold Metcalf. Laser Deceleration of an Atomic Beam. Phys. Rev. Lett. 48, 596-599 (1982).

-
- [29] Paul D. Lett, Richard N. Watts, Christoph I. Westbrook, William D. Phillips, Phillip L. Gould, and Harold J. Metcalf. Observation of atoms laser cooled below the Doppler limit. *Phys. Rev. Lett.* 61, 169-172 (1988).
- [30] A. Aspect, E. Arimondo, R. Kaiser, N. Vansteenkiste and C. Cohen-Tannoudji. Laser cooling below the one-photon recoil energy by velocity-selective coherent population trapping. *Phys. Rev. Lett.* 61, 826-829 (1988).
- [31] C. Salomon, J. Dalibard, W. D. Phillips, A. Clairon and S. Guellati. Laser Cooling of Cesium Atoms below $3 \mu\text{K}$. *Europhys. Lett.* 12 (8), pp. 683-688 (1990).
- [32] E. L. Raab, M. Prentiss, Alex Cable, Steven Chu, and D. E. Pritchard. Trapping of Neutral Sodium Atoms with Radiation Pressure. *Phys. Rev. Lett.* 59, 2631-2634 (1987).
- [33] C. Monroe, W. Swann, H. Robinson, and C. Wieman. Very cold trapped atoms in a vapor cell. *Phys. Rev. Lett.* 65, 1571-1574 (1990).
- [34] C. N. Cohen-Tannoudji and W. D. Phillips. New mechanisms for laser cooling. *Phys. Today* 43(10), 33(1990).
- [35] W. D. Phillips. Laser cooling and trapping of neutral atoms. *Rev. Mod. Phys.* 70 (1998).
- [36] H. J. Metcalf & P. van der Straten. *Laser Cooling and Trapping*. Berlin: Springer (1999).
- [37] C. J. Hood, T. W. Lynn, A. C. Doherty, A. S. Parkins and H. J. Kimble. The Atom-Cavity Microscope: Single Atoms Bound in Orbit by Single Photons. *Science*. 287, 1457 (2000).

-
- [38] P. Munstermann, T. Fischer, P. Maunz, P. W. H. Pinsky and G. Rempe. Dynamics of Single-Atom Motion Observed in a High-Finesse Cavity. *Phys. Rev. Lett.* 82, 3791-3794 (1999).
- [39] J. McKeever, J.R. Buck, A.D. Boozer, A. Kuzmich, H. C. Naegerl, D.M. Stamper-Kurn, and H.J. Kimble. State-Insensitive Cooling and Trapping of Single Atoms in an Optical Cavity. *Phys. Rev. Lett.* 90, 133602 (2003).
- [40] P. Maunz, T. Puppe, I. Schuster, N. Syassen, P.W.H. Pinkse, and G. Rempe. Normal-mode spectroscopy of a single bound atom-cavity system. *Phys. Rev. Lett.* 94, 033002 (2005).
- [41] J. A. Sauer, K.M. Fortier, M.S. Chang, C.D. Hamley, and M.S. Chapman. Cavity QED with optically transported atoms. *Phys. Rev. A* 69, 051804(R), (2004).
- [42] Peter Horak, Bruce G. Klappauf, Albrecht Haase, Ron Folman, Jorg Schmiedmayer, Peter Domokos and E. A. Hinds. Possibility of single-atom detection on a chip. *Phys. Rev. A* 67, 043806 (2003).
- [43] H. J. Carmichael and B. C. Sanders. Multiatom effects in cavity QED with atomic beams. *Phys. Rev. A* 60, 24972504 (1999).
- [44] A. Ottl, S. Ritter, M. Kohl, and T. Esslinger. *Phys. Rev. Lett.* 95, 090404 (2005).
- [45] P. Munstermann, T. Fischer, P.W.H. Pinkse, and G. Rempe. *Opt. Commun.* 159, 63 (1999).
- [46] J. McKeever, J. R. Buck, A. D. Boozer, and H. J. Kimble. *Phys. Rev. Lett.* 93, 143601 (2004).
- [47] C. S. Chuu, F. Schreck, T. P. Meyrath, J. L. Hanssen, G. N. Price, and M. G. Raizen. *Phys. Rev. Lett.* 95, 260403 (2005).

- [48] N. Schlosser, G. Reymond, I. Protsenko, and P. Grangier, *Nature*. 411, 1024 (2001).
- [49] S. Kuhr, W. Alt, D. Schrader, M. Muller, V. Gomer, and D. Meschede. *Science*. 293, 278 (2001).
- [50] M. Trupke, E. A. Hinds, S. Eriksson, E. A. Curtis, Z. Moktadir, E. Kukhareuka, and M. Kraft. Microfabricated high-finesse optical cavity with open access and small volume. *Appl. Phys. Lett.* 87, 211106 (2005).
- [51] Igor Teper, Yu-ju Lin, and Vladan Vuletic. Resonator-Aided Single-Atom Detection on a Microfabricated Chip. *Phys. Rev. Lett.* 97, 023002 (2006).
- [52] J. Goldwin, M. Trupke, J. Kenner, A. Ratnapala and E.A. Hinds. Fast cavity-enhanced atom detection with low noise and high fidelity. *Nat. Commun.* 2:418 doi: 10.1038/ncomms1428 (2011).
- [53] M. Trupke, J. Goldwin, B. Darquie, G. Dutier, S. Eriksson, J. Ashmore, and E. A. Hinds. Atom Detection and Photon Production in a Scalable, Open, Optical Microcavity. *Phys. Rev. Lett.* 99, 063601 (2007).

2

Fundamental Concepts and Theory

2.1 Introduction

Fabry-Perot (FP) cavities or resonators support discrete modes of the electromagnetic (EM) field, constrained by the EM boundary conditions [1, 2]. We can think of a cavity as a store-house for light or electromagnetic energy. Discovered by Charles Fabry and Alfred Perot [3], the Fabry-Perot cavity has proven its versatility in the multitude of experiments that have been possible in the domains of optics, atomic and molecular spectroscopy, metrology and atomic physics. The unique property of this device to act as a filter for frequency, intensity or beam jitter noise as well as act as a mode filter to clean up the spatial mode of a given beam has made it an important tool for atomic and molecular physicists and precision measurement experimentalists. Atoms in cavities [4]

(operating in either the optical and/or microwave regime) have made possible the visualization of novel quantum phenomena [5–8] by altering the vacuum field inside the cavity mode and thus modifying the mode density an atom experiences when placed inside the cavity.

The simplest cavity configuration would be that of two curved mirrors facing each other. One can in principle also construct a cavity with plane mirrors. However issues of maintaining the planar geometry to sub-wavelength accuracy combined with the “walking-off” of the input beam to the planar cavity after a few reflections between the two planar mirrors limit the use of such a configuration for practical purposes.

2.1.1 Basic properties of a resonator

We shall for simplicity consider a planar cavity configuration consisting of two plane mirrors and relate the important cavity parameters with the quality of the mirrors which is nominally specified by the reflectivity of the mirrors, the length of the cavity, the size and radius of curvature of the mirrors. Let us assume that the length of the cavity is L and the mirror reflectivities are R_1 and R_2 . The corresponding transmissions for the mirrors are specified by T_1 and T_2 respectively. For simplicity we set $R = \sqrt{R_1 R_2}$ and $T = \sqrt{T_1 T_2}$.

Let a laser beam of frequency ω and wave-vector $k = \frac{\omega}{c} = \frac{2\pi}{\lambda}$ be incident on one of the mirrors. Here ω is the frequency of the input laser beam, λ is the wavelength of the laser beam and c is the velocity of light. The incident laser beam shall be partially transmitted and partially reflected. The transmitted part enters the resonator and is reflected forth and back many times within the resonator, with a fraction leaking through either of the resonator mirrors each time on reflection. However this process being coherent will lead to addition of amplitudes of each of the reflections and thus result in an interference. This is depicted pictorially in Fig. 2.1.

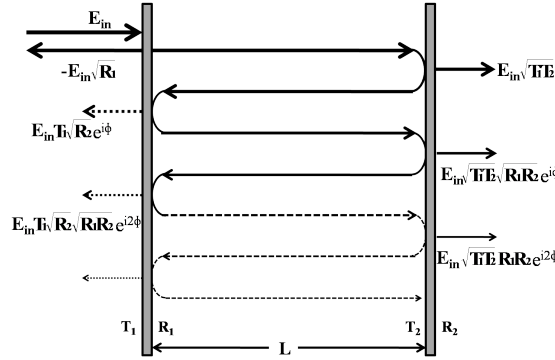


FIGURE 2.1: Basic two mirror planar Fabry-Perot cavity. Shown in the figure are successive reflections and transmissions after each round trip.

The transmitted field amplitude is the sum of all amplitudes after the second mirror given as:

$$E_{trans} = E_{inc}(T + TRe^{i\phi} + TR^2e^{i\phi} + \dots) = E_{inc} \frac{T}{1 - Re^{i\phi}}, \quad (2.1)$$

where $\phi = 2Lk$ is the round trip phase of the light wave in the resonator.

The transmitted intensity is proportional to the square of the above field and is expressed as:

$$I_{trans} \sim |E_{trans}|^2 = E_{inc}^2 \left| \frac{T}{1 - Re^{i\phi}} \right|^2 = E_{inc}^2 \frac{T^2}{(1 - R)^2} \frac{1}{1 + \frac{4R}{(1-R)^2} \sin^2(\frac{\phi}{2})} \quad (2.2)$$

It is easy to see that the maximal transmission $E_{inc}^2 \frac{T^2}{(1-R)^2}$ happens when the round trip phase ϕ is a multiple of 2π . This happens at the resonance frequencies ω_{res} when all reflections add up coherently. This condition is given by:

$$\frac{2L}{c}\omega = \phi = 2\pi.n, n = 1, 2, \dots \quad (2.3)$$

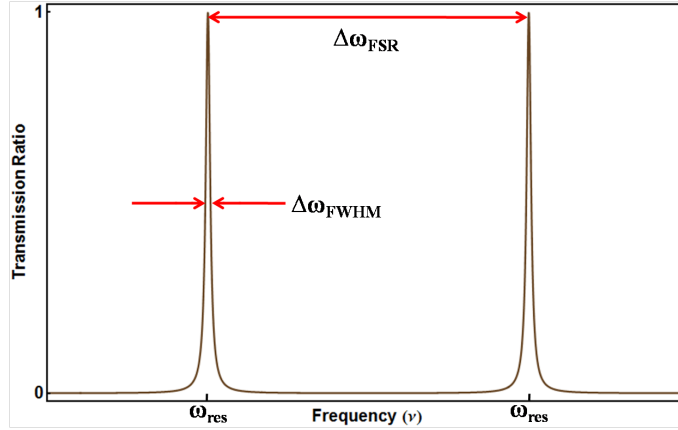


FIGURE 2.2: Transmission of a cavity versus frequency.

The frequencies at which this maximum transmission occurs are the resonance frequencies and are given by

$$\omega_{res} = 2\pi \frac{c}{2L} n = \Delta\omega_{FSR} \cdot n, n = 1, 2, \dots \quad (2.4)$$

The transmission spectrum of the resonator is thus periodic with a period $\Delta\omega_{FSR} = 2\pi \frac{c}{2L}$ called the free spectral range (FSR) of the resonator as illustrated in Fig. 2.2. Physically it signifies the round trip time taken by a photon to traverse the length of the cavity at the speed of light c . The round trip time of the photon is thus given $t_{rndtrip} = \frac{2L}{c} = \frac{2\pi}{\Delta\omega_{FSR}}$. From equation (2.2) we can calculate the linewidth $\Delta\omega_{FWHM}$ of the resonances as

$$\Delta\omega_{FWHM} = \Delta\omega_{FSR} \frac{1 - R}{\pi\sqrt{R}} = \frac{\Delta\omega_{FSR}}{F} \quad (2.5)$$

It is important to note that ideal reflectors suffer from zero losses on surfaces. Hence in the ideal configuration the widths of these resonances should be represented by Dirac-Delta functions. However, for practical purposes real cavities suffer from losses on surfaces which lead to leakage of light after reflection on each surface causing a damping of the cavity field amplitudes and

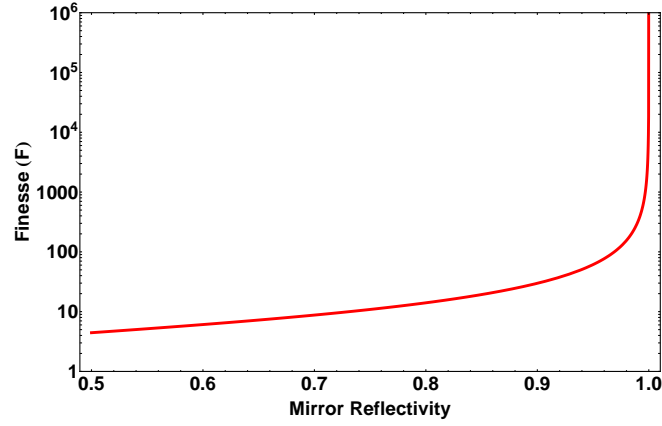


FIGURE 2.3: Finesse of a cavity versus reflectivity for a cavity with mirrors having identical reflectivity. One can see that the finesse reaches extremely high values as one approaches unity value in mirror reflectivity.

thus resulting in a broadening of resonances as illustrated in Fig. 2.2.

The quantity F is called the resonator finesse and is expressed by

$$F = \frac{\pi\sqrt{R}}{1-R} = \frac{\Delta\omega_{FSR}}{\Delta\omega_{FWHM}} \quad (2.6)$$

Physically the finesse signifies the number of bounces a photon makes between the resonator mirrors before exiting the resonator from one of its sides. As we can see from the above expression, the finesse F is purely determined by the quality of the mirrors R . Hence it is imperative to have extremely low lossy mirrors to get a high quality cavity at optical wavelengths. The variation in cavity finesse as a function of mirror reflectivity is shown in Fig. 2.3.

The quality factor of the cavity is denoted by Q and is given by

$$Q = \frac{\omega}{\Delta\omega_{FWHM}} = \frac{\omega F}{\Delta\omega_{FSR}} = \frac{\omega}{\Delta\omega_{FSR}} \frac{\pi\sqrt{R}}{1-R} \quad (2.7)$$

The cavity stores photons for a characteristic time τ_c , where τ_c is given by

$$\tau_c = \frac{F L}{\pi c} = \frac{F}{\Delta\omega_{FSR}} \quad (2.8)$$

τ_c gives the 1/e lifetime of a photon inside the cavity. This timescale is also equivalent to the rate of decay of intra-cavity intensity. The finite lifetime of the photons inside the cavity is due to the limited reflectivity of the mirrors. The decay rate of the cavity electric field is therefore $\kappa = \frac{1}{\tau_c}$. The mean number of reflections N in the cavity is hence given by

$$N = 2 \frac{\tau_c}{t_{rndtrip}} = 2 \frac{\Delta\omega_{FSR}}{2\pi\Delta\omega_{FWHM}} = \frac{F}{\pi} \quad (2.9)$$

For a symmetric resonator with $R_1 = R_2 = R$ and $T_1 = T_2 = T$, we have for very high reflectivity mirrors ($R \approx 1$), $T = 1 - R$. Thus the field inside the cavity, which forms a standing wave, has the resonant intra-cavity field strength at an antinode given by E_{cav} and is expressed as

$$E_{cav} \approx E_{inc} \frac{2}{\sqrt{1-R}} \quad (2.10)$$

The resonant intra-cavity intensity at an anti-node is then given by

$$I_{cav} = I_{inc} \frac{4}{1-R} \approx 4 \frac{F}{\pi} I_{inc} \quad (2.11)$$

This shows that the cavity enhances the intracavity intensity at an antinode by $4 \frac{F}{\pi}$. Hence one can in principle increase the strength of interaction between an atom and the field inside the cavity by several orders of magnitude as compared to that in free space. However, for the experiments reported in this thesis, the atoms are not localized to an anti-node along the resonator axis and hence they will see an average intensity over one or several periods of the

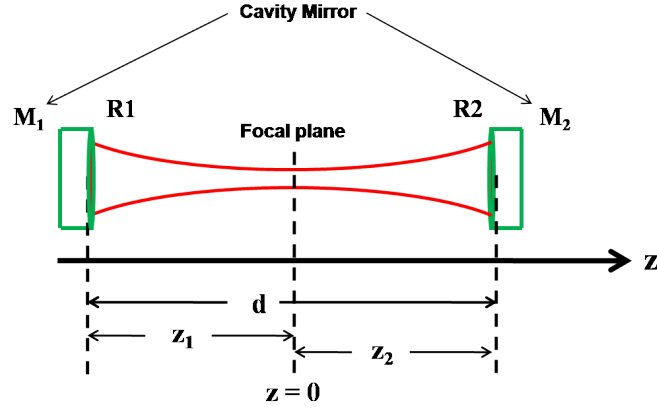


FIGURE 2.4: Spherical two mirror resonator configuration for Gaussian beam analysis.

standing wave along the resonator axis given by:

$$I_{cav}^{avg} = 2 \frac{F}{\pi} I_{inc} \quad (2.12)$$

2.1.2 Gaussian beam properties of a spherical mirror cavity

Let us consider a cavity composed of two spherical mirrors of radius of curvature R_1 and R_2 separated by a total distance d . Let us assume further that a Gaussian beam fits into the resonator and is focused at $z = 0$. Individually the mirrors are placed at distances z_1 and z_2 from the point $z = 0$ with the constraint that $z_1 + z_2 = d$ as shown in Fig. 2.4.

For stable cavity configuration, the radius of curvature of each mirror at a given point z within the cavity must be identical to the radius of curvature R of the Gaussian beam at the same point within the cavity. This condition gives

$$R(z_1) = -R_1 \Rightarrow R_1 = z_1 + \frac{z_R^2}{z_1} \quad (2.13a)$$

$$R(z_2) = +R_2 \Rightarrow R_2 = z_2 + \frac{z_R^2}{z_2} \quad (2.13b)$$

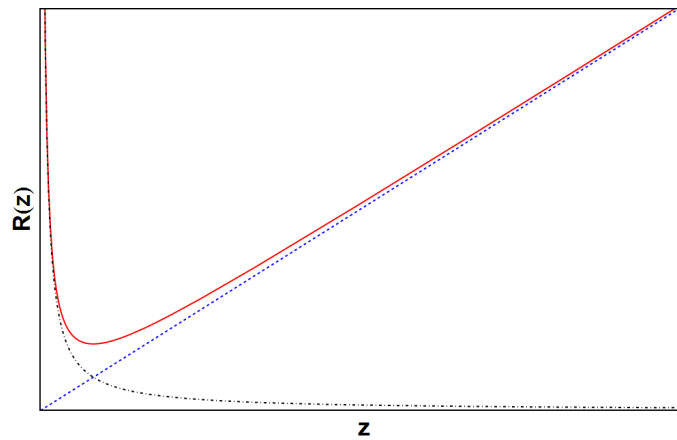


FIGURE 2.5: Variation of the radius of curvature R of a Gaussian beam from the distance z from the beam waist is shown by the red (solid line) curve. The black curve (dot dashed curve) shows the $\sim \frac{1}{z}$ variation while the blue curve (dashed curve) shows the z (linear) dependence (that is the spherical wavefront nature of the Gaussian beam). The point of intersection of the black and blue curves is the Rayleigh range of the beam.

The sign convention used here is taking into account the Gaussian wavefront curvature which is generally taken as positive for a diverging beam and negative for a converging beam for a beam propagating from left to right. The sign convention followed for the mirrors are that the radius of curvature for the mirrors are positive for mirrors that are viewed to be concave from within the cavity while negative for those which are viewed to be convex from within the cavity. We further assume that this treatment is being done in the paraxial wave approximation. A plot of the radius of curvature of the Gaussian beam as a function of z is shown in Fig. 2.5.

The quantity z_R is called the Rayleigh range and signifies the depth of focus for a Gaussian beam. Physically it implies the maximal usable working length for a given Gaussian beam at a wavelength λ with a minimum beam waist w_0 before the beam starts to diverge. A more commonly used quantity used in the context of Gaussian beam propagation is the confocal parameter $b = 2z_R$.

We further define the Gaussian beam stability parameters for the two mirrors

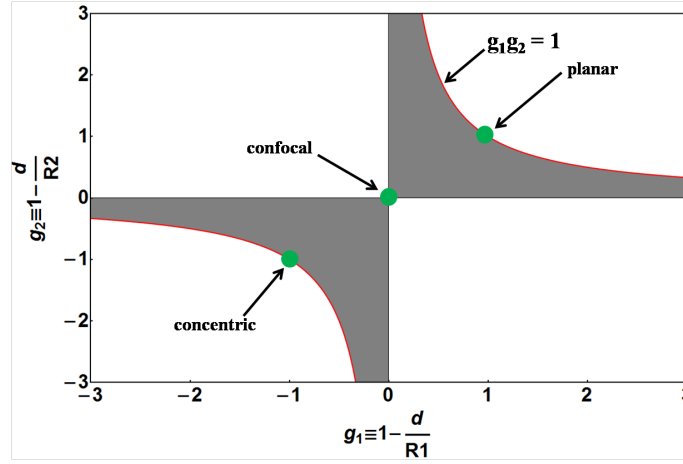


FIGURE 2.6: Stability diagram of a two mirror resonator. Resonators with parameters in the shaded regions are stable.

as g_1 and g_2 . These are expressed as

$$g_1 = 1 - \frac{d}{R_1} \quad (2.14a)$$

$$g_2 = 1 - \frac{d}{R_2} \quad (2.14b)$$

For resonator stability we have the criterion that

$$0 < g_1 g_2 < 1 \quad (2.15)$$

Fig. 2.6 depicts the regions of stability for which the resonator stability condition as given in equation (2.15) is satisfied for a two mirror resonator.

Solving the above equations (2.13) and (2.14) along with the constraint $z_1 + z_2 = d$ for the Rayleigh range z_R and the mirror locations z_1 and z_2 , in terms of the stability parameters g_1 and g_2 , we have as z_R

$$z_R^2 = \frac{d^2 g_1 g_2 (1 - g_1 g_2)}{(-2g_2 g_1 + g_1 + g_2)^2} \quad (2.16)$$

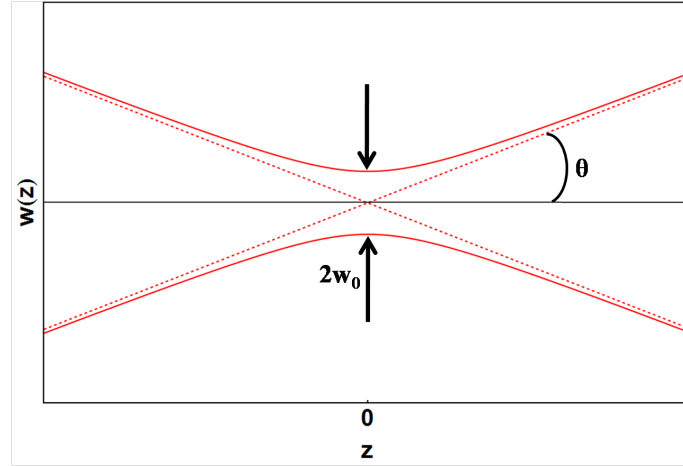


FIGURE 2.7: Dependence of the diameter or spot size $w(z)$ of a Gaussian TEM_{00} beam on the distance z from the beam waist. The angle θ is far field divergence angle and $2w_0$ is the beam waist at $z=0$.

and the mirror locations at z_1 and z_2 as

$$z_1 = \frac{d(1-g_1)g_2}{-2g_2g_1 + g_1 + g_2} \quad (2.17a)$$

$$z_2 = \frac{dg_1(1-g_2)}{-2g_2g_1 + g_1 + g_2} \quad (2.17b)$$

We can also express the minimum beam waist w_0 at the focus in terms of the above resonator parameters as

$$w_0^2 = \frac{d\lambda}{\pi} \sqrt{\frac{g_1g_2(1-g_1g_2)}{(-2g_2g_1 + g_1 + g_2)^2}} \quad (2.18)$$

The beam diameter $w(z)$ is expressed as

$$w(z) = w_0 \sqrt{1 + \frac{z^2}{z_R^2}} \quad (2.19)$$

From Fig. 2.7 we see that the beam diameter $w(z)$ has the following properties:

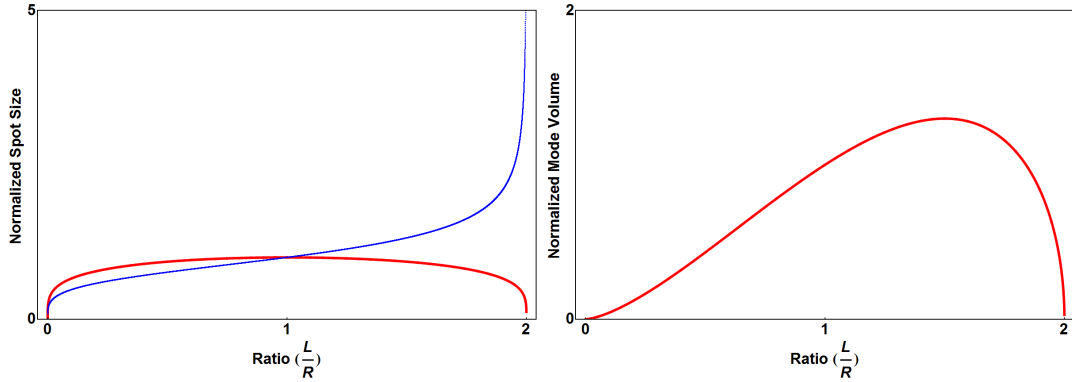


FIGURE 2.8: Comparison of several properties of a TEM_{00} mode in the whole stability region of a symmetric optical resonator. Both curves are normalized to the TEM_{00} mode of a confocal cavity where $L = R$. For the plot of beam spot size versus $\frac{L}{R}$, the red curve (solid line) shows the variation of the cavity waist w_0 as a function of $\frac{L}{R}$, while the blue (dashed line) curve shows the variation of the spot size at the mirror position versus $\frac{L}{R}$.

- $w(z = 0) = w_0$
- For $z \gg z_R$ the radius $w(z)$ has a linear dependence on z at the asymptotes given by

$$w(z) = w_0 \frac{z}{z_R} = \frac{\lambda}{\pi w_0} z \equiv \theta z \quad (2.20)$$

where $\theta = \frac{\lambda}{\pi w_0}$.

- At $z = z_R$, we get $w(z) = \sqrt{2}w_0$.

The beam waist (or the beam spot size) at the mirrors are then given by w_1 and w_2 which are expressed as

$$w_1^2 = \frac{d\lambda}{\pi} \sqrt{\frac{g_2}{g_1(1 - g_1g_2)}} \quad (2.21a)$$

$$w_2^2 = \frac{d\lambda}{\pi} \sqrt{\frac{g_1}{g_2(1 - g_1g_2)}} \quad (2.21b)$$

As seen from Fig. 2.8 the waist is minimum in both near-planar and near-concentric configurations, but the spot size on the mirror increases as the near-concentric case is approached. Further the mode volume is maximum for $\frac{L}{R} =$

$\frac{3}{2}$, and approaches zero in the near-planar ($L \rightarrow 0$) and near-concentric ($L \rightarrow 2R$) configurations.

The mode volume for the TEM₀₀ mode is given by V_{00} , where

$$V_{00} = \frac{\pi L w_0^2}{4} \quad (2.22)$$

The mode volume for higher order modes is given by V_{mn} , where

$$V_{mn} = V_{00}(m!n!2^{(m+n)}) \quad (2.23)$$

For a fixed set of mirrors with radius of curvature R , a cavity constructed in the confocal configuration always has the maximum waist w_0 . This is evident from the Fig. 2.8 where the waist, the spot size on the mirror and the mode volume have been plotted as a function of $\frac{L}{R}$ and all values have been normalized for a TEM₀₀ mode for the case of a confocal cavity. This is a particularly advantageous configuration for the experiments where the atom number in the cavity mode is of primary concern.

2.1.3 Eigenmodes of a resonator

The field inside the cavity is the solution of Maxwell equations with appropriate boundary conditions imposed by the mirror geometry. The wave equation for an electric field propagating along the z -direction in the paraxial regime is known as the Helmholtz equation and is given as

$$(\nabla^2 + 2ik\frac{\partial}{\partial z})\psi = 0 \quad (2.24)$$

Here ψ is the envelope of the wave and we assume that it varies slowly on the scale of λ , the wavelength of the field. Here $\nabla^2 \equiv \frac{\partial^2}{\partial x^2} + \frac{\partial^2}{\partial y^2}$ and $k = \frac{2\pi}{\lambda}$. The

implication of the smooth variation of the wave envelope over the scale of λ are as follows:

$$\frac{\partial\psi}{\partial z} \ll \frac{\psi}{\lambda} \quad (2.25)$$

which we can rewrite as

$$\frac{\partial\psi}{\partial z} \ll k\psi \quad (2.26)$$

and hence it follows that

$$\frac{\partial^2\psi}{\partial z^2} \ll k \frac{\partial\psi}{\partial z} \quad (2.27)$$

and thus we can neglect the $\frac{\partial^2}{\partial z^2}$ term in the Helmholtz equation.

For fields propagating along a given direction (assuming z-direction for the treatment reported here), the solution for the wave equation in the paraxial regime is well described by a Gaussian beam. To obtain the zero order solution of the wave equation above, we first introduce a trial solution of the form

$$\psi(x, y, z) = \psi_0 e^{\frac{ik(x^2+y^2)}{2q(z)}} e^{ip(z)} \quad (2.28)$$

The solution of equation (2.28) is then reduced to finding $q(z)$ and $p(z)$. The trial solution as given in equation (2.28) fixes the dependence on the transverse coordinates x and y and thus forces the solution to have a symmetric transverse profile as demanded physically by the field. A complex solution for q will lead to the terms introduced intuitively above. The final solution for the electric field amplitude ψ_0 is expressed as

$$\psi(x, y, z) = \psi_0 \frac{w_0}{w(z)} e^{-\frac{x^2+y^2}{w^2(z)}} e^{ikz - i \tan^{-1}(\zeta)} e^{ik \frac{x^2+y^2}{R(z)}} \quad (2.29)$$

where $w(z)$ is the beam waist as a function of z defined as

$$w(z) = w_0 \sqrt{\frac{z^2}{z_R^2} + 1} \quad (2.30)$$

with z_R being the Rayleigh length or Rayleigh range of the beam and given by

$$z_R = \frac{\pi w_0^2}{\lambda} \quad (2.31)$$

Further $R(z)$ is the radius of curvature of wavefronts and is expressed as

$$R(z) = z \left(1 + \frac{z_R^2}{z^2} \right) \quad (2.32)$$

while the $\tan^{-1}(\zeta)$ term is called that Guoy phase shift [9] and is given by

$$\tan^{-1}(\zeta) = \frac{z}{z_R} \quad (2.33)$$

The first exponential term along with the prefactors as given in equation (2.29) describes the amplitude factor which represents completely the intensity profile of the Gaussian beam. The second exponential term describes the longitudinal phase factor and since it depends only on z , it gives the on axis phase behavior for the Gaussian beam. The third exponential term in equation (2.29) is the radial phase factor and it describes the behavior of the beam phase in the x - y plane.

The Guoy phase shift describes the rapid phase change of the electric field when traversing the point of minimal beam diameter at $w_0 = 0$ (beam waist) and represents a small departure from planarity. Physically it signifies a phase retardation in comparison to the plane wave with the \tan^{-1} form implying a monotonically increasing retardation, amounting to a total of π phase change over all z . Gouy phase effects are generic to focusing-beam-type solutions to

the wave equation and are important in computing the resonant frequencies of optical resonators. Further the Guoy phase retardation implies that the phase velocity of a Gaussian beam is slightly larger than c , since the spacing between wave fronts is slightly larger than λ .

Another important quantity in the above analysis is the complex beam parameter $q(z)$ which is defined as

$$q(z) = z + iz_R \quad (2.34)$$

The complex beam parameter plays an important role in the analysis of Gaussian beam propagation, and especially in the analysis of optical resonator/cavities using ray transfer matrices. However, it is more commonly used in its reciprocal form and is expressed by

$$\frac{1}{q(z)} = \frac{1}{z + iz_R} = \frac{1}{R(z)} - i\frac{\lambda}{\pi w^2(z)} \quad (2.35)$$

The higher order solutions of the paraxial wave equation depends completely on the symmetry of the resonator/cavity mode structure and hence is related to the system of coordinates chosen to describe the structural mode symmetry in the resonator. Examples of such higher order modes are the Hermite-Gaussian modes, the Laguerre-Gaussian modes and the Ince-Gaussian modes which are related to the cavity mode structures having either rectangular, cylindrical or ellipsoidal symmetry.

Hermite-Gaussian modes

As mentioned earlier, Hermite-Gaussian beams are a family of structurally stable laser modes that have rectangular symmetry (and hence can be described by a cartesian coordinate system) along the propagation axis. The standard

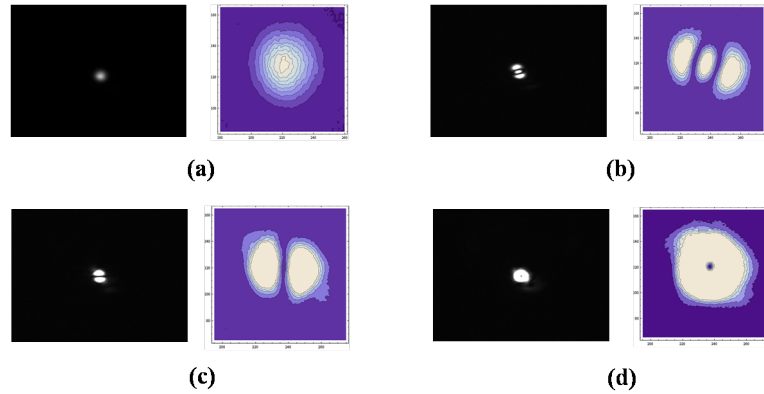


FIGURE 2.9: Hermite-Gaussian mode structure recorded for an experimental cavity in the lab by a charge coupled device (CCD) camera placed in transmission. The figures represent the images recorded and their corresponding intensity profiles as mapped by a contour plot over the plane of the CCD camera. Shown in figures (a), (b), (c) and (d) are the lowest Hermite-Gaussian modes TEM_{00} , TEM_{20} , TEM_{10} and TEM_{01*} . The TEM_{01*} is a very special mode, also known as doughnut mode, is a special case consisting of a superposition of two TEM_{01} modes, with each mode being oriented orthogonal to one another.

form of the Hermite-Gauss mode is given by

$$\psi_{m,n}(x, y, z) = \frac{1}{w(z)} \sqrt{\frac{2^{1-m-n}}{\pi m! n!}} H_m \left(\frac{\sqrt{2}x}{w(z)} \right) H_n \left(\frac{\sqrt{2}y}{w(z)} \right) \exp \left(\frac{ik(x^2 + y^2)}{2R(z)} - \frac{x^2 + y^2}{w(z)^2} \right) \times \exp^{-i\phi_{m,n}} \quad (2.36)$$

The order of the above solution is defined by $m+n$. Modes of the same order are degenerate in laser resonators or cavities. Here H_m and H_n are Hermite polynomials of order m and n respectively. Since the Hermite-Gaussian function for the electric field is scaled everywhere to the spot size $w(z)$ via the arguments of $\frac{x}{w(z)}$ and $\frac{y}{w(z)}$ of the Hermite polynomials, the intensity profile of any given TEM_{mn} mode changes size but not the shape/pattern as it propagates forward (in this case the z -direction) in a given direction. A particular TEM_{mn} mode looks exactly the same except apart being modified by a scaling factor as it propagates along the z -direction.

Apart from the Hermite polynomials, the other terms in equation (2.36) are

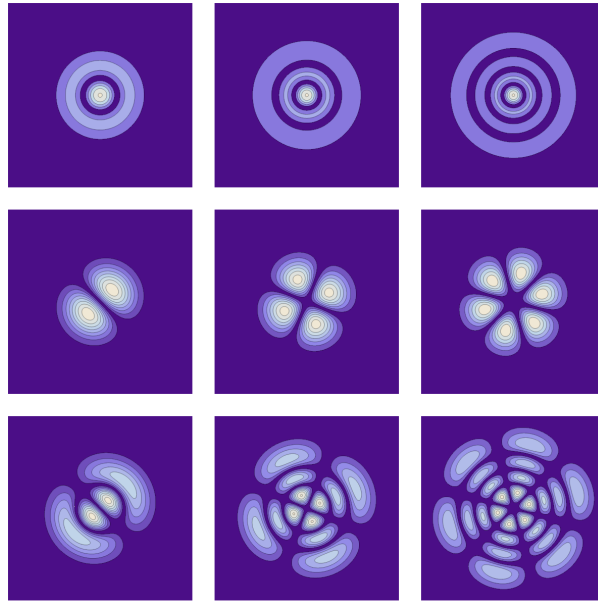


FIGURE 2.10: Representative Laguerre-Gaussian mode patterns obtained from theoretical plots of the electric field intensity as per the electric field amplitude given in equation 38. Starting from the top left corner, the first row of figures show the lower order Laguerre-Gaussian modes TEM_{10} , TEM_{20} , TEM_{30} . The middle row of figures (starting from the left) represent the modes TEM_{01} , TEM_{02} and TEM_{03} while the third row of figures (again starting from the left) represent the modes TEM_{11} , TEM_{22} and TEM_{33} .

the same as in equation (2.29) with a modified Guoy phase $\phi_{m,n} = (m+n+1)\tan^{-1}\left(\frac{z}{z_R}\right)$. The physical significance of the dependence of the Guoy phase on the indices m and n is the manifestation of higher resonant frequencies of higher order (transverse) modes in laser cavities and resonators. The constant term that normalizes the total intensity is given by $\sqrt{\frac{2^{1-m-n}}{\pi m! n!}}$. A few examples of the intensity patterns of Hermite-Gaussian modes recorded for an experimental cavity in our lab is shown in Fig. 2.9.

Laguerre-Gaussian modes

Another class of modes characterized by azimuthal and radial symmetry along their propagation axis rather than the rectangular symmetry exhibited by Hermite-Gaussian modes are known as the Laguerre-Gaussian modes. These modes

carry an intrinsic rotational orbital angular momentum of $i\hbar$ per photon. This intrinsic property of the Laguerre-Gaussian beams ensures that a object with a different refractive index placed along the propagation axis will experience a torque. This property of the Laguerre-Gaussian beams is of considerable physical significance and practical interest, particularly in the field of optical trapping and for driving micromachined elements with light. However it is important to note that this intrinsic rotational momentum is totally different from the angular momentum that arises due to the polarization of light. Some of the lower order Laguerre-Gaussian modes are shown in Fig. 2.10.

The standard form of the Laguerre-Gauss mode is given by

$$\begin{aligned} \psi_{m,n}(\rho, \theta, z) = & \frac{m!}{w(z)} \sqrt{\frac{2}{\pi m!(m+n)!}} \left(\frac{\rho}{w(z)}\right)^n L_m^n\left(\frac{2\rho^2}{w(z)^2}\right) \exp\left(-\frac{\rho^2}{w(z)^2} + \frac{ik\rho^2}{2R(z)}\right) \\ & \times \exp(i\phi_{mn}^L) \exp(in\theta) \end{aligned} \quad (2.37)$$

where ρ and θ are expressed as

$$\rho = \sqrt{x^2 + y^2} \quad (2.38)$$

$$\theta = \tan^{-1}\left(\frac{y}{x}\right) \quad (2.39)$$

with ϕ_{mn}^L being given by

$$\phi_{mn}^L = (n + 2m + 1) \tan^{-1}(\zeta) = (n + 2m + 1) \frac{z}{z_R} \quad (2.40)$$

and $R(z)$ being defined in the usual way as given in equation (2.32).

Here L_m^n is the generalized Laguerre polynomial of order m . It is evident from the above form of the Laguerre Gaussian beam that real part of the electric field amplitudes are rotationally/cylindrically symmetric around the axis z , and the number $(m+1)$ is the number of minima and maxima along a radial line from

the center $\rho=0$. Thus the modes of a Laguerre Gaussian beam are circles of constant intensity along the radial axis and have a $e^{in\theta}$ variation in the azimuthal direction. However one should keep in mind that the first minimum always occurs at $\rho = 0$, where the amplitude of the electric field vanishes. The number n defines the change of phase in terms of an integral multiple of 2π when one goes around the axis of propagation $\rho = 0$, and thus defines the chirality of the mode. Further Laguerre Gaussian beams exhibit similar Guoy phase shifts as the rectangular (Hermite-Gaussian) modes.

2.1.4 Transverse modes of a resonator

As seen from either the Hermite or Laguerre-Gaussian electric field amplitude expression given by equations (2.36) and (2.37) respectively, a Gaussian beam with transverse mode numbers m, n experiences a Guoy phase shift of $(m+n+1)\pi$ in passing through a focal region relative to a plane wave. The total Gouy phase shift is reduced in the case of a resonator since the the beam is confined to a finite region around the focal point which lies in the plane $z = 0$ as given in Fig. 2.4. The resonance condition is that the round trip phase shift $\phi_{m,n}(k) = 2\pi q$, where q is an integer denoting the axial mode number. Thus the round trip phase shift experienced by a beam of wavelength λ for a cavity of length L is now expressed by

$$\begin{aligned}\phi_{m,n} &= 2Lk - 2(m+n+1)(\tan^{-1}(\frac{L}{2z_R}) - \tan^{-1}(\frac{-L}{2z_R})) \\ &= \frac{2\pi}{\Delta\omega_{FSR}}\omega - 2(m+n+1)\cos^{-1}(1 - \frac{L}{R})\end{aligned}\quad (2.41)$$

Since the resonance condition is $\phi_{m,n}(k) = 2\pi q$, where $q = 1, 2, \dots$, we get,

$$\omega_{m,n} = \Delta\omega_{FSR}(q + \frac{1}{\pi}(m+n+1)\cos^{-1}(1 - \frac{L}{R}))\quad (2.42)$$

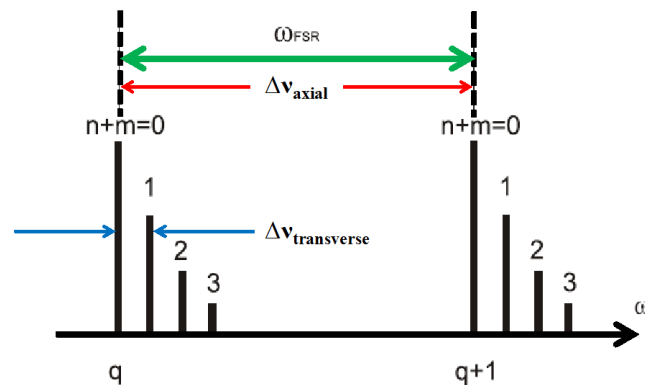


FIGURE 2.11: Lowest order transverse modes for a near-planar resonator ($L \ll R$).

where q is the longitudinal order denoting the number of antinodes in the resonator.

We can see that the frequencies of the transverse modes are in general not coincident with those of the axial modes (except in the case of a confocal cavity where $L=R$), and produces a complex and irregular pattern of fringes at the output as a function of the input laser frequency. The transverse modes are equispaced along the frequency axis with the modes of order $(m+n)$ being degenerate. As the transverse mode separation for a given longitudinal order depends on the length of the resonator, it is possible to measure very accurately the length of any given cavity from the measured separation between the transverse and an axial mode of a given order q . This is shown in Fig. 2.11. However, in practice one may excite many transverse modes of a resonator without using a mode matching lens assembly to preferentially couple light to a single axial mode of the resonator. For a given spot size of the fundamental transverse mode w on a mirror, the half-width of higher order transverse modes with index m is roughly $w\sqrt{m}$.

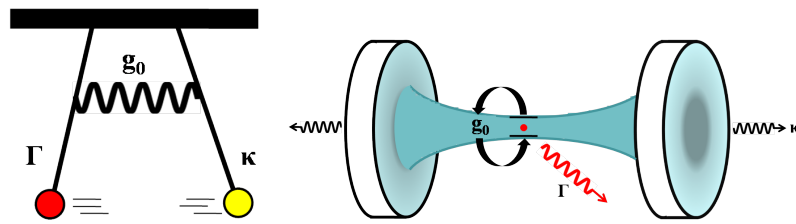


FIGURE 2.12: Left: A pair of a coupled oscillator analogue of the atom-cavity system. Right: Simplified schematic of a real system consisting of a two level atom coupled to the field of a single mode inside a cavity.

2.1.5 Atom Cavity Interactions

The basic interaction of an atom with the electromagnetic field of a single cavity mode is very well described by the Jaynes-Cummings model [10]. This model was first proposed by E. T. Jaynes and F. W. Cummings in 1963. Although their approach was purely quantum mechanical, we can understand many features of this inherent quantum mechanical system by a classical analogue of two harmonic oscillators as shown in Fig. 2.12. The atom is characterized by a damping rate Γ while the cavity is associated with a damping rate κ . When there exists no coupling between the oscillators, the normal modes of the system are degenerate.

The strength of the atom-cavity interaction is governed by a factor g_0 also known as the atom-cavity coupling strength. We can naively think of g_0 as a spring connecting these two harmonic oscillators and thus ensures that there is a coherent energy exchange between the oscillators, and the system has two nondegenerate eigenmodes. However if the coupling strength g_0 is smaller than either of the damping rates, the energy will be dissipated from the atom-cavity system before any coherent energy exchange takes place. Keeping this analogy in mind, we can proceed towards understanding the quantum mechanical treatment of the atom-cavity system.

2.1.6 Quantum theory of a two level atom interacting with a field of a single cavity mode: The Jaynes-Cummings model

We consider a simplified system consisting of a single point-like two-level atom at rest, coupled to a single quantized mode of the cavity. We also assume the system to be ideal such that there is no spontaneous decay of the atom from its excited to its ground state and further assume that there is no loss of photons from the cavity. We also consider a monochromatic field of frequency ω_c to be forming a standing wave inside the fundamental mode of the cavity, where $\frac{\omega_c}{2\pi}$ is the resonance frequency of the cavity.

We introduce photons by the method of canonical field quantization and express the the field operators in terms of creation and annihilation operators a^\dagger and a which add and remove monochromatic, polarized photons in the cavity mode respectively. They obey the canonical commutation relation

$$[a, a^\dagger] = 1 \quad (2.43)$$

The number of photons stored in the cavity is given by the expectation value of the photon number operator denoted by $\langle a^\dagger a \rangle$ and hence we can define the Hamiltonian for the single mode of the optical field as

$$H_{field} = \hbar\omega_c \left(a^\dagger a + \frac{1}{2} \right) \quad (2.44)$$

Here $\hbar\omega_c$ is the energy of a single photon of the field present inside the single mode of the cavity, where \hbar is $(1/2\pi)$ times the Planck constant h . The energy eigenstates are photon number states $|0\rangle, |1\rangle, |2\rangle, \dots$

We describe the two level atom in a manner similar to the description of

the photon inside the cavity by using the second quantization formalism. We label the ground and excited states of the atom as $|g\rangle$ and $|e\rangle$ respectively. We assume that the ground state has zero energy and ω_a is the atomic transition frequency between the ground and excited states. The Hamiltonian for such a two-level atom is given by

$$H_{atom} = \hbar\omega_a |e\rangle\langle e| \quad (2.45)$$

We now introduce the operators σ^\dagger , σ and σ_z which denote respectively the creation, annihilation and inversion of atomic excitation and these are expressed as

$$\sigma^\dagger = |e\rangle\langle g|, \quad \sigma = |g\rangle\langle e| \quad \text{and} \quad \sigma_z = |e\rangle\langle e| - |g\rangle\langle g| \quad (2.46)$$

The operators σ^\dagger , σ and σ_z are the pseudo-spin (or the pseudo-Pauli matrix) operators fulfilling the algebra

$$[\sigma^\dagger, \sigma] = \sigma_z, \quad [\sigma_z, \sigma^\dagger] = 2\sigma^\dagger, \quad [\sigma_z, \sigma] = -2\sigma, \quad (2.47)$$

with

$$\sigma^\dagger = \begin{pmatrix} 0 & 1 \\ 0 & 0 \end{pmatrix}, \quad \sigma = \begin{pmatrix} 0 & 0 \\ 1 & 0 \end{pmatrix}, \quad \sigma_z = \begin{pmatrix} 1 & 0 \\ 0 & -1 \end{pmatrix} \quad (2.48)$$

Thus the atomic Hamiltonian can be re-written as

$$H_{atom} = \hbar\omega_a \sigma^\dagger \sigma \quad (2.49)$$

The coupling constant between the atom and the cavity mode is given by

$$g(\vec{r}) = g_0 f(\vec{r}) \quad (2.50)$$

where $f(\vec{r})$ is the normalized spatial mode profile of the cavity, g_0 is the maximum coupling constant.

The spatially dependent cavity mode function $f(\vec{r})$ obeying the quantization condition that $\frac{kL}{\pi}$ is an integer is given by

$$f(\vec{r}) = f(x, y, z) = \exp\left(-\frac{x^2 + y^2}{w_0^2}\right) \cos(kz) \quad (2.51)$$

with the cavity mode volume V being given by

$$V = \int_{mode} [f(\vec{r})^2] dV \quad (2.52)$$

The zero point energy of the field mode inside the cavity is given by $\frac{1}{2}\hbar\omega_c$. If we normalize the vacuum field energy $\epsilon_0 E^2 V$ over the cavity mode volume to the zero point energy of the field mode in the cavity by virtue of field quantization [11], we get,

$$E = \sqrt{\frac{\hbar\omega_c}{2\epsilon_0 V}} \quad (2.53)$$

where $V = \frac{\pi}{4} w_0^2 L$ is the effective (or the quantization) mode volume of the cavity and E is the electric field amplitude of the vacuum modes inside the cavity.

We now assume the atom to be positioned at an antinode of the standing wave inside the cavity so that the spatial dependence of the interaction can be omitted. We further assume that the atomic dipole moment d is oriented parallel to the direction of the cavity field polarization at the aforementioned antinode position. The interaction Hamiltonian in the Heisenberg picture is

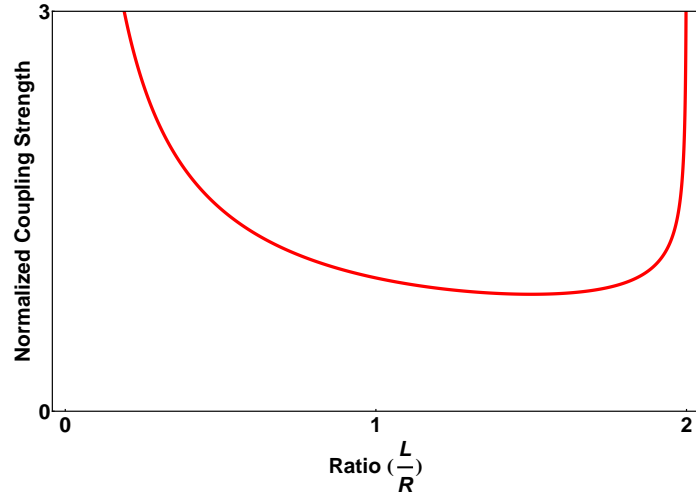


FIGURE 2.13: Variation of the atom-cavity coupling strength g_0 as a function of $\frac{L}{R}$, normalised to the coupling strength in the confocal case.

given by

$$H_{atom-field} = \vec{d} \cdot \vec{E} = d(\sigma^\dagger e^{i\omega_a t} + \sigma e^{-i\omega_a t}) \cdot E(a^\dagger e^{i\omega_c t} + a e^{-i\omega_c t}) \quad (2.54)$$

where d is the dipole moment of the atomic transition.

If we now apply the rotating wave approximation (RWA) to the equation (2.54) such that $(\omega_a - \omega_c) \ll (\omega_a + \omega_c)$, we can drop the energy non-conserving $\sigma^\dagger a^\dagger$ and σa terms (since these operators average out on the timescale of the evolution of the operators σa^\dagger and $\sigma^\dagger a$), and finally reduce the above atom-field Hamiltonian to

$$H_{atom-field} = dE(\sigma^\dagger a + \sigma a^\dagger) = \hbar g_0(\sigma^\dagger a + \sigma a^\dagger) \quad (2.55)$$

where g_0 is given by

$$g_0 = \frac{dE}{\hbar} = \sqrt{\frac{d^2 \omega_c}{2\hbar \epsilon_0 V}} \quad (2.56)$$

The coupling constant g_0 is a function of the dipole moment d of the atomic

transition, the resonance frequency of the cavity ω_c and the cavity mode volume V . For a given atom, the coupling constant can be increased by minimizing the cavity mode volume which in turn translates to minimizing the length of the cavity and the radii of curvature of the mirrors. A plot of the coupling constant g_0 as a function of the ratio $\frac{L}{R}$ is shown in Fig. 2.13. Here R is the radius of curvature of the cavity mirror.

An equivalent expression for g_0 is given by

$$g_0 = \sqrt{\frac{6c^3\Gamma}{\omega_c^2 w_0^2 L}} \quad (2.57)$$

where c is the velocity of light, Γ is the spontaneous emission rate of the excited state, w_0 is the cavity waist and L is the cavity length.

Finally the total Hamiltonian governing the atom-cavity system after ignoring the vacuum-field (or the zero point) energy term is expressed by

$$\begin{aligned} H &= H_{atom} + H_{field} + H_{atom-field} \\ &= \hbar\omega_a \sigma^\dagger \sigma + \hbar\omega_c a^\dagger a + \hbar g_0 (\sigma a^\dagger + \sigma^\dagger a) \end{aligned} \quad (2.58)$$

The above Hamiltonian in equation (2.58) defines the Jaynes-Cummings model that describes a model system consisting of a two level atom interacting with the single mode of a cavity under the rotating wave approximation (RWA), ignoring any dissipative or damping processes like spontaneous emission or loss from cavity mirrors. The zero point energy term can be neglected on the grounds that it does not contribute to the dynamics of the system. The Jaynes-Cummings model is well known in quantum mechanics since it is one of the few models for which an analytical solution can be derived.

2.1.7 Analytical solution of the Jaynes-Cummings model for a system without dissipation

As seen from equation (2.55), the atom-field Hamiltonian term $\hbar g_0(\sigma a^\dagger + \sigma^\dagger a)$ describes processes where a photon in the mode is annihilated while the atom is excited or vice versa. Hence this Hamiltonian couples states of the form $|g, n + 1\rangle$ and $|e, n\rangle$ described in the canonical basis, where $(n+1)$ is the total number of excitations in the system. $|g, n + 1\rangle$ and $|e, n\rangle$ are the bare states depicting the state of the atom and indexing the number of photons in the cavity mode. The ground state of this system $|g, 0\rangle$ is an energy eigenstate. The other energy eigenstates of the coupled system in the dressed state formalism are given by linear combinations of the bare states $|g, n + 1\rangle$, with the atom in the ground state and n intracavity photons, and $|e, n\rangle$, with the atom in the excited state and $(n + 1)$ photons. These new dressed states are given by

$$|n + 1, +\rangle = \cos \theta |e, n\rangle + \sin \theta |g, n + 1\rangle \quad (2.59a)$$

$$|n + 1, -\rangle = -\sin \theta |e, n\rangle + \cos \theta |g, n + 1\rangle \quad (2.59b)$$

where $n = 0, 1, 2, \dots$

The transformation from the basis $\{|g, n + 1\rangle, |e, n\rangle\}$ to the “dressed state” basis $\{|n + 1, +\rangle, |n + 1, -\rangle\}$ is accomplished by a rotation of the system in its Hilbert space by the “mixing angle” θ which is a function of the atom-cavity coupling constant g_0 and the atom-cavity detuning $\Delta = (\omega_c - \omega_a)$. The mixing angle θ is given by

$$\theta = \tan^{-1} \frac{2g_0\sqrt{n+1}}{\Delta + \sqrt{4g_0^2(n+1) + \Delta^2}} \quad (2.60)$$

The Hamiltonian in the dressed state basis is block diagonal in 2×2 blocks which signifies that only pairs of eigenstates shall be coupled to each other.

Thus physically it implies that an excited atom can emit a photon into the cavity and reabsorb it, but only that is the limit of the energy transfer.

The energy eigenvalues obtained by diagonalizing the Hamiltonian expressed in the dressed state basis $\{|n+1, +\rangle, |n+1, -\rangle\}$ are given by

$$E_{(n+1),+} = (n+1)\hbar\omega_c + \hbar\frac{\Delta}{2} + \frac{1}{2}\hbar\sqrt{4g_0^2(n+1) + \Delta^2} \quad (2.61a)$$

$$E_{(n+1),-} = (n+1)\hbar\omega_c + \hbar\frac{\Delta}{2} - \frac{1}{2}\hbar\sqrt{4g_0^2(n+1) + \Delta^2} \quad (2.61b)$$

where $n = 0, 1, 2, \dots$, while the energy splitting between two states is given by

$$\Delta E_{n+1} = E_{(n+1),+} - E_{(n+1),-} = \hbar\sqrt{4g_0^2(n+1) + \Delta^2} \quad (2.62)$$

The eigen-energies of the system form a ladder of doublets, with a central spacing of one photon energy $\hbar\omega_c$ and a splitting which increases with the square root of n as shown in Fig. 2.14. For a degenerate system ($\omega_c = \omega_a$) the spectroscopy of the first doublet of these states (that is, for $n=0$) gives a pair of resonances with the splitting $2g_0$, which is called vacuum-Rabi splitting or the normal mode splitting for an atom-cavity system.

For an atom which is initially in the state $|g, n+1\rangle$, on being coupled to a resonant field within the single mode of a cavity, the populations of the ground and excited states of the atom-cavity system evolve with time t in the following manner:

$$P_{g,n+1} = \cos^2(\sqrt{n+1}g_0t) = \frac{1}{2}[1 + \cos(2\sqrt{n+1}g_0t)] \quad (2.63a)$$

$$P_{e,n} = \sin^2(\sqrt{n+1}g_0t) = \frac{1}{2}[1 - \cos(2\sqrt{n+1}g_0t)] \quad (2.63b)$$

Thus the populations in both the ground and excited states of the composite atom-cavity system exhibit Rabi oscillations at an angular frequency $2\sqrt{n+1}g$

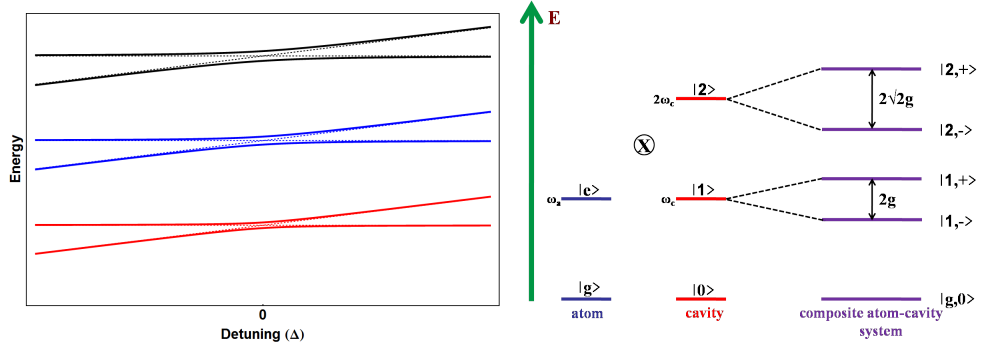


FIGURE 2.14: Left: Avoided level crossings in the Jaynes - Cummings model for different laser detunings. The splitting is maximal on resonance at zero detuning and the eigenstates have rotated from the bare state basis to the dressed state basis as shown by the dashed lines in the figure. The parameters chosen for the plot are $g_0 = 0.5$ and $\omega_c = 30g_0$. Right: The energy levels of the Jaynes-Cummings Hamiltonian form a ladder of doublets as shown.

when $(n+1)$ quanta of energy is exchanged between the atom and the cavity field. For the special case of $n=0$, which signifies the single photon criterion, the Rabi oscillations occur at frequency $2g_0$. Hence g_0 is also referred to as the single-photon Rabi frequency.

The Jaynes-Cummings model can be extended to an N -atom system where N denotes the number of atoms interacting with the field of a single mode of the cavity leading to the Tavis-Cummings model [12]. This model is not considered here. However the collective coupling rate g_{eff} between the atomic ensemble and the cavity field mode is enhanced by a factor \sqrt{N} leading to $g_{eff} = g_0\sqrt{N}$, where N is the number of atoms in the cavity mode.

2.1.8 Analytical solution of the Jaynes-Cummings model for a system with dissipation

The Jaynes-Cummings model considered in the previous section is applicable only to perfectly closed systems which do not suffer from dissipation of any kind, and hence is an example of the ideal regime of operation. However all

real systems are lossy and prone to decoherence due to their coupling with the environment. Thus an atom-cavity system in reality constitutes an open quantum system coupled to the environment. Further any kind of meaningful measurement or spectroscopy on such a real system requires coupling to an external field. The transition from the closed to the open quantum system is made possible by the inclusion of two physical processes: (a) the inclusion of a pump term in order to drive the system and replenish losses and (b) a coupling to modes other than the privileged cavity mode to describe the decay of the excitation of both atom and cavity mode.

Dissipation present in the coupled atom cavity system includes loss mechanisms such as the field decay rate κ of the cavity due to finite reflectivity of mirrors and the dipole decay rate Γ of the excited atomic state due to spontaneously scattered photons out of the cavity mode. Two coherent processes exist: the first one being a coherent pump rate, in the form of a laser field supplies the cavity mode with fresh photons to compensate the losses while the other being the atom-cavity coupling constant g that signifies the extent of coherent exchange of energy/interaction of the atom with the cavity mode field.

Ideally we would like to study or use the coherent interactions present in the atom-cavity system with as little dissipation as possible. In other words we emphasize that the coherent evolution must be fast and more stronger compared to the decoherence processes. Thus we would ideally want the system to enter the regime of strong coupling:

$$g \gg \kappa, \Gamma \quad (2.64)$$

For a complete description of such a system the influence of the environment is usually taken into account in form of a reservoir. We consider the system and the environment as a single entity described by a density matrix ρ , which includes all degrees of freedom. Mathematically, ρ is composed of vectors from the combined Hilbert space H_{Total} given by $H_S \otimes H_R$, where H_S and H_R are the Hilbert spaces of the system and the environment. The environment is hence

the collection of all free-space modes which couple to either the atom or the cavity mode.

We assume that we are operating the system under the Born approximation. Thus the interaction of the system with the reservoir is weak and it can be treated perturbatively. We further apply the Markovian approximation under which we assume that the excitations and correlations in the reservoir die out quickly as compared to the timescale of evolution of the system density matrix ρ characterized by $(g_0, \Gamma, \kappa)^{-1}$ and thus the system is independent of its past evolution and can be regarded as having no memory. The temporal evolution of the open quantum system can then be determined by the quantum master equation [13] (also known as the von-Neumann equation) for its density matrix operator ρ from

$$\dot{\rho} = \frac{i}{\hbar}[\rho, H] + \mathcal{L}_{dissipation} \quad (2.65)$$

where the first term on the right hand side of equation (2.65) describes the coherent evolution of the density matrix operator ρ under the Hamiltonian H while the second term on the right hand side of equation (2.65) describes the operator $\mathcal{L}_{dissipation}$ of the Lindblad form and contains all possible modes of dissipation or damping existing in the atom-cavity system. Here H represents the total Hamiltonian of the system including a pump term that replenishes dissipated photons in the cavity mode.

The total Hamiltonian H is given by

$$H = \hbar\Delta_a\sigma^\dagger\sigma + \hbar\Delta_c a^\dagger a + \hbar g_0(\sigma a^\dagger + \sigma^\dagger a) + \epsilon(a^\dagger + a) \quad (2.66)$$

where the σ^\dagger -s and a -s represent the usual creation/annihilation operators for the atomic excitation and photon number states respectively while ϵ represents the coherent pumping/driving term. The driving field ϵ is proportional to the incident field and to the input mirror transmittivity. Here we invoke the weak field approximation and assume that it is very small so that at most one excitation

in the system is present. Δ_a and Δ_c represent the detunings of the drive field from the actual atomic and cavity transitions and are given by

$$\Delta_a = \omega_a - \omega_L \quad (2.67a)$$

$$\Delta_c = \omega_c - \omega_L \quad (2.67b)$$

where ω_L is the frequency of the drive field while ω_a and ω_c represent respectively the atomic and cavity mode resonance frequencies.

We also introduce the complex detuning parameters $\tilde{\Delta}_a$ and $\tilde{\Delta}_c$ following ref. [14] which are given by

$$\tilde{\Delta}_a = \Delta_a - i\Gamma \quad (2.68a)$$

$$\tilde{\Delta}_c = \Delta_c - i\kappa \quad (2.68b)$$

The Lindblad operator $\mathcal{L}_{dissipation}$ is of non-unitary nature and contains two dissipation channels namely, the spontaneous emission of a photon from the atom out of the cavity mode, which is described by the dissipation operator $\sqrt{\Gamma}\sigma$ and the decay of a photon from the cavity mode through the cavity mirrors, having a dissipation operator $\sqrt{\kappa}\sigma$. The damping/dissipation operator is thus defined as

$$\mathcal{L}_{dissipation} = \frac{\Gamma}{2}(2\sigma\rho\sigma^\dagger - \sigma^\dagger\sigma\rho - \rho\sigma^\dagger\sigma) + \frac{\kappa}{2}(2a\rho a^\dagger - a^\dagger a\rho - \rho a^\dagger a) \quad (2.69)$$

The time evolution of the expectation value of any system operator \hat{o} can be determined from the master equation (2.65) as follows:

$$\langle \dot{\hat{o}} \rangle = \text{Tr}[\hat{o}\dot{\rho}] = \text{Tr}[\hat{o}(\mathcal{L}\rho)] \quad (2.70)$$

where \mathcal{L} is the Liouville super operator defined by

$$\mathcal{L} = \frac{i}{\hbar}[\rho, H] + \mathcal{L}_{dissipation} \quad (2.71)$$

The Heisenberg equations of motion give the time evolution for a set of system operators (a , σ , σ_z) from the master equation (2.65). The equations for time evolution are as follows:

$$\langle \dot{a} \rangle = -i(\tilde{\Delta}_c \langle a \rangle + \epsilon \tilde{\Delta}_c + g_0 \langle \sigma \rangle) \quad (2.72a)$$

$$\langle \dot{\sigma} \rangle = -i(\tilde{\Delta}_a \langle \sigma \rangle - g_0 \langle a \sigma_z \rangle) \quad (2.72b)$$

$$\langle \dot{\sigma}_z \rangle = -2\Gamma(1 + \langle \sigma_z \rangle) + 2ig_0(\langle a^\dagger \sigma \rangle - \langle a \sigma^\dagger \rangle) \quad (2.72c)$$

where σ_z is defined in the usual manner as given by equation (2.47).

Mathematically the weak field approximation is equivalent to setting $\langle a \sigma_z \rangle = \langle a \rangle$ in equation (2.72b) (which implies that the atom is always in the state $|g\rangle$) and dropping equation (2.72c). Thus we obtain a new, closed set of coupled equations given by:

$$\langle \dot{a} \rangle = -i(\tilde{\Delta}_c \langle a \rangle - \epsilon \tilde{\Delta}_c - g_0 \langle \sigma \rangle) \quad (2.73a)$$

$$\langle \dot{\sigma} \rangle = -i(\tilde{\Delta}_a \langle \sigma \rangle + g_0 \langle a \rangle) \quad (2.73b)$$

The steady state of the system is obtained by setting ($\{\langle \dot{a} \rangle, \langle \dot{\sigma} \rangle = 0$). Usually the steady state or stationary solutions of the master equation are calculated numerically utilizing special techniques such as quantum Monte - Carlo methods.

The expectation value of the intracavity photon number and the mean atomic

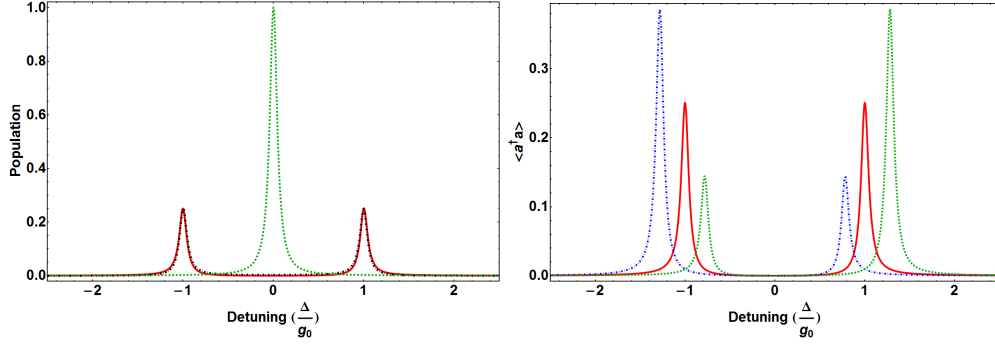


FIGURE 2.15: Left: Vacuum Rabi splitting for the atom cavity system. The red (solid line) and black (dotted) curves show respectively the cavity and atomic population versus laser detuning. The green (dashed) curve at zero detuning corresponds to the cavity transmission with $g_0 = 0$, $\kappa = 4$ and $\Gamma = 4$. Right: The normal mode spectra for different atom cavity detunings are shown. The blue (dotted) curve represents the situation for $\Delta_a = \Delta_c + \frac{g_0}{2}$, the green (dashed) curve represents the situation for $\Delta_a = \Delta_c - \frac{g_0}{2}$ while the red (solid) curve gives the photon population for $\Delta_a = \Delta_c$. The parameters chosen for the plots are $g_0 = 40$, $\kappa = 0.1g_0$ and $\Gamma = 0.1g_0$, which ensures that the system is in the strong coupling regime.

excitation in the steady state are given by

$$\langle \sigma^\dagger \sigma \rangle = \epsilon^2 \frac{g_0^2}{|\Lambda|^2} \quad (2.74a)$$

$$\langle a^\dagger a \rangle = \epsilon^2 \frac{\Delta_a^2 + \frac{\Gamma^2}{4}}{|\Lambda|^2} \quad (2.74b)$$

where Λ is defined in the following manner

$$\Lambda = \frac{\Gamma\kappa}{4} + g_0^2 - \Delta_a\Delta_c - i\left(\frac{\Gamma}{2}\Delta_c + \frac{\kappa}{2}\Delta_a\right) \quad (2.75)$$

Here $\langle \sigma^\dagger \sigma \rangle$ gives the probability of finding a photon in the cavity while $\langle a^\dagger a \rangle$ gives the probability of finding the atom in its excited state. The equations (2.74) are sufficient to calculate a spectrum of the system that gives two resonances known as the normal-mode resonances or the vacuum Rabi doublets of the atom-cavity system. These pair of resonances are characterized by the eigen-frequencies ω_+ and ω_- which can be obtained from the equations (2.73).

The normal mode frequencies are expressed as

$$\omega_+ = \omega_L - \frac{1}{2}(\tilde{\Delta}_a + \tilde{\Delta}_c) + \frac{1}{2}\sqrt{4g_0^2 + |\tilde{\Delta}_a - \tilde{\Delta}_c|^2} \quad (2.76a)$$

$$\omega_- = \omega_L - \frac{1}{2}(\tilde{\Delta}_a + \tilde{\Delta}_c) - \frac{1}{2}\sqrt{4g_0^2 + |\tilde{\Delta}_a - \tilde{\Delta}_c|^2} \quad (2.76b)$$

The eigenfrequencies ω_+ and ω_- have complex values as seen from the equation (2.76). The real part of the eigenfrequencies determine the position of the resonances whereas the imaginary part of the eigenfrequencies describes their widths. The width of the resonances is thus given by $\frac{\kappa+\Gamma}{2}$. The width of the eigenfrequencies physically signifies the presence of dissipation in the system. The vacuum Rabi splitting (VRS) or the normal mode splitting for the atom cavity system shown in Fig. 2.15 is given by the separation between the position of the eigenfrequencies given in equation (2.76). The vacuum Rabi splitting describes the phenomenon by which the originally degenerate resonances of the bare atom and the cavity split into two new resonances in the coupled system (for $\omega_a = \omega_c$). The vacuum Rabi splitting denoted by Δ_{VRS} is given by

$$\Delta_{VRS} = \sqrt{4g_0^2 + |\tilde{\Delta}_a - \tilde{\Delta}_c|^2} \quad (2.77)$$

The vacuum Rabi splitting (VRS) has been experimentally observed with atomic beams passing through a cavity [15, 17, 46], with atoms trapped inside cavities [18–20], and also with Bose-Einstein condensates inside cavities [21, 22]. The normal-mode splitting has also been seen in solid state macroscopic cavity QED systems like quantum dots coupled to micropillars [23, 24] or microdiscs [25] or with quantum dots placed inside photonic crystals [26].

The VRS mentioned above can be explained both from the quantum mechanical framework using the coupled harmonic oscillator analogue. It can also be explained with purely semiclassical arguments using absorption and dispersion phenomena. In the quantum mechanical picture the atom cavity

system behaves as two coupled harmonic oscillators under the weak field approximation. The cavity can be envisioned as a quantized harmonic oscillator with an infinite number of equally spaced energy levels. The atom which is effectively described as a two level system can also be thought of a harmonic oscillator in the weak field driving limit. This correspondence has been shown by H. J. Carmichael [27] for a two-level atom in terms of two bosonic operators using the Schwinger representation where the bosonic operators correspond to the creation and the annihilation operators for atomic/photon number states. However we can draw this correspondence only under the assumption that the excited state has a very low population. The atom cavity coupling constant g , which mediates a dipole coupling between the atomic system and the cavity mode, removes the mode degeneracy that exists between the atoms and the cavity mode. The composite system then has two normal modes with a mode splitting usually equal to twice the coupling constant in the strong coupling regime ($g \gg \kappa, \Gamma$). The normal mode splitting can be probed as long as rate of energy exchange given by the vacuum Rabi frequency (Ω_{VR}) is larger than the dissipation (κ, Γ) present in the system.

From the semi-classical perspective [28, 29] we can think of the atoms to be acting as a medium where a phase shift occurs due to the refractive index of the medium. However the field inside a cavity also experiences a phase shift while traversing back and forth between the mirrors. Now if we can control the input drive field frequency such that the phase shift caused by the atoms gets compensated for by the phase shift in the cavity, we can enhance the transmission of the cavity by virtue of constructive interference due to the zero phase shift condition that has been established by this protocol. In the limit of low drive field intensity and for small atom-cavity detunings the aforementioned zero phase shift condition can be achieved at three different points in the frequency domain. The central frequency point in this frequency band is heavily suppressed due to atomic absorption. The remaining two frequency

points appear as sidebands in transmission on either side of the absent central frequency peak and are known as the vacuum Rabi peaks.

Finally we would like to mention three other important parameters with respect to defining the operating regime of a cavity in the strong coupling limit. These are namely the single atom cooperativity C , the critical photon number n_0 and the critical atom number N_0 [30]. These are expressed as

$$C = \frac{g_0^2}{\kappa\Gamma} \quad (2.78a)$$

$$n_0 = \frac{\Gamma^2}{2g_0^2} \quad (2.78b)$$

$$N_0 = \frac{\kappa\Gamma}{g_0^2} \quad (2.78c)$$

The single atom cooperativity physically signifies the amount of cavity to free space scattering ratio and is essentially determined only by the geometry of the cavity mode. It also determines the effect of a single atom on the cavity spectrum. The critical photon number signifies the amount of photon quanta one would need to saturate the transition along the cavity mode. The critical atom number is the inverse of the quantity C and hence it gives the smallest amount of atoms that are necessary to perturb the system effectively to go into the strong coupling regime. In the strong coupling regime we should always have $\{n_0 \ll 1, C \gg 1\}$ so that a single quanta dominates the dynamics of the atom-cavity system.

2.2 Laser cooling: Basics and theoretical background

In this section, the atomic properties of Rubidium which are relevant to the optical switching experiment (using the ^{87}Rb isotope) and cavity based experiments using laser cooled ^{85}Rb atoms are discussed briefly. We introduce the basic concepts of atom-light interactions needed to explain the principles of laser cooling. We also describe briefly the principles of Doppler cooling processes.

2.2.1 Atomic properties of Rubidium

The primary alkali metal atom of choice for the experiments reported in this thesis is Rubidium (Rb). In general Rubidium is a preferred alkali metal of the atomic physics community for laser cooling and trapping due to the following reasons: it can be easily produced using alkali metal dispensers [31–33] to generate enough vapor with small amount of heating necessary for laser cooling applications, it is paramagnetic in nature thus making it suitable for magnetic trapping, relatively cheap lasers for cooling can be built using readily available commercial laser diodes and finally the relatively large hyperfine splitting in the $5P_{3/2}$ state allows the cooling cycle to operate on a closed transition far enough away from other transitions (thus lowering the probability of optical pumping via absorption of off-resonant photons) so as to allow large laser detunings necessary for effective laser cooling.

There are two naturally occurring isotopes of Rubidium - one stable isotope with mass number 85 with a relative abundance of 72.2% and other with mass number 87 with abundance 27.8% having an extremely weak decay (having a half life of 48.8×10^9 years) thus making it effectively stable. As mentioned earlier, for the experiments reported in this thesis, both isotopes have been used

and hence the atomic properties of both ^{85}Rb and ^{87}Rb are presented here. The vapour pressure p_V , for the solid and the liquid phase of Rb, according to the vapor-pressure model presented in [34] is given by the following equations:

$$\log_{10} p_V = 2.881 + 4.857 - \frac{4215}{T} \quad (\text{solid phase}) \quad (2.79a)$$

$$\log_{10} p_V = 2.881 + 4.312 - \frac{4040}{T} \quad (\text{liquid phase}) \quad (2.79b)$$

where p_V is the the vapor pressure in torr and T is the temperature in Kelvin.

The electronic structure of Rubidium is $1s^2 2s^2 2p^6 3s^2 3p^6 3d^{10} 4s^2 4p^6 5s^1$ or in shorthand notation $[\text{Kr}]5s^1$, where Kr is the noble gas element Krypton. Thus the ground-state electronic configuration of Rubidium consists of closed shell configuration plus a single 5s valence electron that gives a spectrum which is similar to that Hydrogen (H). The total angular momentum (J) of the ground state 5s is 1/2. The ground state is represented by the term state $5S_{1/2}$. In the first excited state the single electron becomes a $5p^1$ electron. The total angular momentum can be 1/2 or 3/2 since the possible values of the total angular momentum quantum number J are $|l-s|, |l-s|+1, \dots, |l+s|-1, |l+s|$, with $s=1/2$ and $l=0$ or 1 depending on the electron being in the s and p orbital respectively. Thus the two excited states in the 5p manifold are represented by the term states $5P_{1/2}$ and $5P_{3/2}$ respectively. The transition from the $5S_{1/2}$ state to the $5P_{1/2}$ state is known as the D_1 transition while the transition from the $5S_{1/2}$ to $5P_{3/2}$ is referred to as the D_2 transition. The energy level diagram for Rb is shown in Fig. 2.16.

The dominant term in the interaction between the nuclear spin and the electron gives rise to the magnetic hyperfine splitting. The nonrelativistic Hamiltonian for an atom having a single electron form assuming an infinitely massive

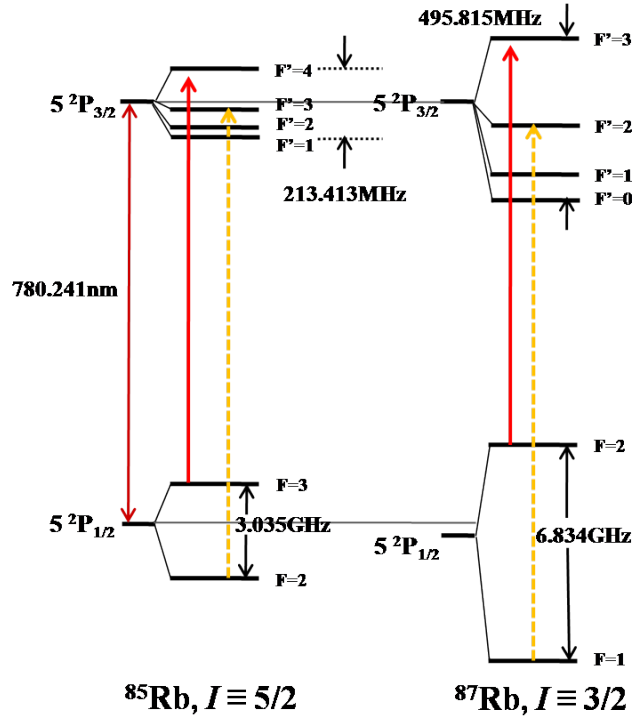


FIGURE 2.16: The Rubidium (Rb) energy level diagram for the D_2 transitions of ^{85}Rb and ^{87}Rb . The red (solid) and the orange (dashed) arrows represent respectively the relevant cooling and repumping transitions for a magneto-optical trap.

nucleus, is given by

$$H = K.E + P.E + H_{S.O.} + H_{hyperfine1} + H_{hyperfine2} \quad (2.80a)$$

$$= \frac{p^2}{2m} + \frac{Z_{eff}e^2}{4\pi\epsilon_0 r} + \zeta(r)\vec{L}\cdot\vec{S} + \alpha\vec{J}\cdot\vec{I} \\ + \frac{\beta}{2I(2I-1)J(2J-1)} [3(\vec{I}\cdot\vec{J})^2 + \frac{3}{2}(\vec{I}\cdot\vec{J}) - I(I+1)J(J+1)] \quad (2.80b)$$

where the five terms K.E, P.E, $H_{S.O.}$, $H_{hyperfine1}$ and $H_{hyperfine2}$ are labelled in order respectively. K.E. is the kinetic energy of the single electron where $\vec{p} = -i\hbar\vec{\nabla}$ and hence p denotes classically the mechanical momentum of the electron of mass m. P.E. is the potential energy term and is given by the Coulomb interaction of the single electron with the nucleus and the core electrons under the assumption that the nucleus and core electrons form a spherical symmetric

potential with charge Z_{eff} where Z_{eff} is an effective atomic number. $H_{S.O.}$ is the spin orbit interaction, where \vec{L} and \vec{S} are the orbital and spin angular momenta of the single electron while $\zeta(r)$ is the spin-orbit coupling coefficient. $H_{hyperfine1}$ is the magnetic hyperfine interaction, where α is called the magnetic hyperfine structure constant, while \vec{J} and \vec{I} are the total electron and nuclear angular momenta, respectively. $H_{hyperfine2}$ is the electric quadrupole hyperfine interaction, where β is the electric quadrupole interaction constant, and I and J are angular momenta quantum numbers. Although the major electric pole of the rubidium nucleus is the spherically symmetric electric monopole giving rise to the Coulomb interaction, it also has an electric quadrupole moment. However it does not have an electric dipole moment. The above Hamiltonian in equation (2.80b) leads us to the energy level diagram for the D_2 transitions of ^{85}Rb and ^{87}Rb as given below in the figure.

The finite lifetime (τ) of the excited state results in a width in the absorption profile of the atom which has a Lorentzian lineshape with full width half maximum (FWHM) given by $\Gamma = \frac{1}{\tau}$, where Γ denotes the natural line width of the atom. However, in general, for an ensemble of atoms at a given temperature T the atoms have the possibility of moving in any direction consistent with the Maxwellian distribution of velocities at the temperature T. In any particular direction, the velocity distribution can be well described by a Gaussian function. For an atom moving at velocity \vec{v} , the frequency ω of an incoming photon is doppler shifted by an amount ω' , where ω' is given by

$$\omega' = \omega - \vec{k} \cdot \vec{v} \quad (2.81)$$

where \vec{k} is the wave-vector of the photon and $|\vec{k}| = \frac{2\pi}{\lambda}$. Here λ is the wavelength of the photon and is given by $\lambda = \frac{c}{\omega}$ with c denoting the speed of light. Hence the absorption profile of an atomic ensemble at a finite temperature T shows

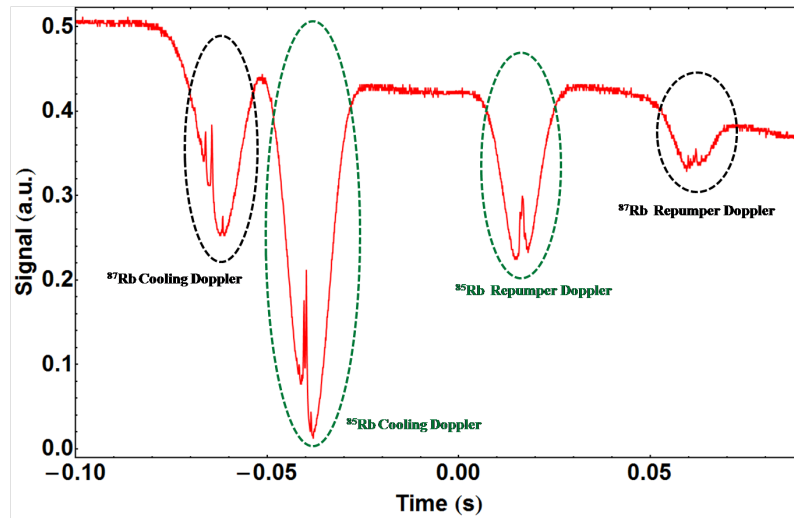


FIGURE 2.17: The Rubidium (Rb) spectral features as resolved by a saturated absorption spectroscopy set-up using a home built ECDL scanning across the relevant Doppler broadened dips spanning by $\approx 6.8\text{GHz}$ in frequency domain.

a Doppler broadened profile that depends on temperature of the atomic ensemble. At room temperature ($\approx 23^\circ\text{C}$), the Doppler width of 5S-5P transition in Rubidium is two orders of magnitude more than the natural linewidth of the $F'=4$ state of the $5^2P_{3/2}$ state of the ^{85}Rb D_2 transition which has an FWHM of $\simeq 6\text{MHz}$.

The narrow spectral features of the naturally occurring Rb are hence accessed by a technique known as saturated absorption spectroscopy whose primary feature is its avoidance of or insensitivity to the Doppler effect. This technique relies on two beams: a stronger pump beam that saturates the atomic transition and a weak probe beam which counter-propagates with the pump beam. The pump beam is usually more intense than the probe beam and is nominally 10 times more stronger than the probe beam. Narrow linewidth ($\approx 1\text{MHz}$) linewidth (FWHM) of diode lasers have made it possible to resolve spectral features whose natural linewidth are $\approx 6\text{MHz}$ within a thermal background of $\approx 500\text{MHz}$ that exists at room temperature vapor. A saturated absorption spectroscopy signal of the D_2 transitions of Rb recorded by a home built diode laser in the ECDL (external cavity diode laser) configuration is shown in

Fig. 2.17. The spectroscopy is obtained from a Rb vapor cell acquired from Triad Technologies Inc., USA.

The selection rules for electric dipole transitions are given by

$$\Delta F = 0 \pm 1 \quad (\text{but not } 0 \rightarrow 0) \quad (2.82a)$$

$$\Delta J = 0 \pm 1 \quad (2.82b)$$

$$\Delta s = 0 \quad (2.82c)$$

where F , J and s are the nuclear, total angular momentum and spin quantum numbers respectively. Here $\vec{F} = \vec{J} + \vec{I}$ and F can take values from $|J-I|$, $|J-I|+1, \dots, |J+I|-1, |J+I|$.

Given the geometrical arrangement of pump and probe beams that counter-propagate in the saturated absorption spectroscopy set-up, there arises crossover resonances in addition to the normal resonance lines, which occur at frequencies $\frac{\nu_1 + \nu_2}{2}$ for each pair of true or normal transitions at frequency ν_1 and ν_2 . The crossover transitions are often in general more intense than the normal transitions.

2.2.2 Interaction of static magnetic fields with atoms:

Zeeman effect

For an atom with a total nuclear angular momentum quantum number F , there exists $2F+1$ Zeeman sublevels (where $m_F = -F, \dots, F$) that governs the angular distribution of the electronic wavefunction. The Zeeman sublevels are degenerate in the absence of a magnetic field. In the presence of a magnetic field (B), the degeneracy of the energy levels is lifted. If the strength of the magnetic field is weak, such that the magnetic interaction is very small compared to the

hyperfine splittings ground and excited states of the atom, then F is a good quantum number. The interaction Hamiltonian in this case is given by

$$H_B = \mu_B g_F \frac{F_z}{\hbar} B_z \quad (2.83)$$

where μ_B is the Bohr magneton, g_F is the hyperfine Lande g-factor while F_z and B_z are the nuclear angular momentum quantum number and the magnitude of the magnetic field respectively. The above Hamiltonian for the atom is expressed assuming that a magnetic field exists along the z-direction (i.e., along the atomic quantization axis). In the afore-mentioned weak field limit the interaction Hamiltonian H_B perturbs only the zero-field eigenstates of $H_{\text{hyperfine1}}$ and $H_{\text{hyperfine2}}$ causing a linear splitting of the energy levels in the $|F, m_F\rangle$ basis. Thus the state $|F, m_F\rangle$ is shifted in energy by

$$\Delta E = -\mu_B g_F m_F B_z \quad (2.84)$$

where the hyperfine Lande g-factor g_F is expressed as

$$g_F \simeq g_J \frac{F(F+1) + J(J+1) - I(I+1)}{2F(F+1)} \quad (2.85)$$

and g_J is Lande g-factor given by

$$g_J \simeq 1 + \frac{J(J+1) + S(S+1) - L(L+1)}{2J(J+1)} \quad (2.86)$$

where S denotes the spin quantum number.

However in the case of intermediate magnetic field strengths of magnitude (~ 0.5 KG), the magnetic interaction is comparable to the hyperfine splitting and hence the approximations used earlier in the case of linear Zeeman effect are not applicable anymore. In this regime of magnetic field strengths

the quadratic Zeeman effect becomes significant and in general, one must resort to numerical techniques to diagonalize the Hamiltonian $H_B + H_{\text{hyperfine}1} + H_{\text{hyperfine}2}$. However for ground state manifolds with $J = 1/2$ and an arbitrary value of I , the quadratic Zeeman effect can be expressed analytically through the Breit-Rabi formula [35, 36] as

$$\Delta E_{|J=1/2, m_J, I, m_I\rangle} = -\frac{\Delta E_{\text{hfs}}}{2(2I+1)} + \mu_B g_I m B \pm \frac{\Delta E_{\text{hfs}}}{2} \left(1 + \frac{4mx}{2I+1} + x^2\right)^{1/2} \quad (2.87)$$

where $\Delta E_{\text{hfs}} = A_{\text{hfs}}(I + 1/2)$ is the hyperfine splitting with A_{hfs} being the magnetic dipole constant, $m = m_I \pm m_J = m_I \pm 1/2$ (where the \pm sign is taken to be the same as in (2.87)), g_I is the nuclear g-factor and x is given by

$$x = \frac{(g_J - g_I)\mu_B B}{\Delta E_{\text{hfs}}} \quad (2.88)$$

A simpler expression which may be used for the two states $m = \pm(I + 1/2)$, to avoid any sign confusion that might arise while using equation (2.87), is given by

$$\Delta E_{|J=1/2, m_J, I, m_I\rangle} = \Delta E_{\text{hfs}} \frac{I}{(2I+1)} \pm \frac{1}{2}(g_J + 2I g_I)\mu_B B \quad (2.89)$$

A very important application of the Breit-Rabi formula is to calculate the small-field shift between the $m_F = 0$ sublevels of the two hyperfine ground states in the context of the ‘‘clock transition’’, for which there does not arise any first-order Zeeman shift. The energy shifts of the hyperfine states of ^{85}Rb $5^2\text{S}_{1/2}$ ground state with magnetic field is shown in Fig. 2.18.

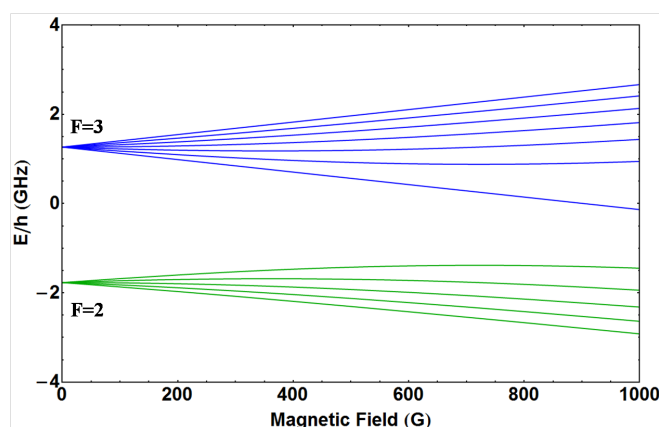


FIGURE 2.18: Zeeman effect for $^{85}\text{Rb } 5^2\text{S}_{1/2}$ ground state. x-axis denotes the magnetic field in Gauss and y-axis denotes the corresponding energy shifts calculated in GHz using equation (2.87). The energy shift at zero magnetic field is due to hyperfine coupling. The levels are grouped according to the value of F in the low-field (Zeeman) regime.

2.2.3 Interaction of light with atoms: Coherent and incoherent processes

When an atom interacts with an external monochromatic laser field, two fundamentally different physical phenomena occur:

1. A coherent process by which an atom absorbs (scatters) photons from the laser field and subsequently emits them via stimulated emission into the laser field. In such stimulated emission processes, the emitted photon travels in the same direction as the inducing photon from the external laser field. The transition probability of stimulated emission is same as the transition probability for absorption and is proportional to the intensity (I) of incident radiation.

2. An incoherent process by which the absorbed photons are spontaneously emitted in a random direction due to finite life time of the excited state.

The selection rule for allowed transitions in the magnetic hyperfine levels (m_F) is given by $m_{F'} - m_F = 0$ or ± 1 .

Both the coherent and the incoherent processes lead to a different kinds of forces acting on the atom, namely the dipole force and the spontaneous force

respectively. The origin of these two forces can be explained by means of the Lorentz's model of the electron [37]. In the simplest configuration possible, the electron can be regarded as an oscillator elastically bound to the core of the atom via a spring with force constant k_{spring} . Thus the binding force $F_{binding}$ is given by

$$F_{binding} = -k_{spring}x = -m_e \omega_0^2 x \quad (2.90)$$

where m_e is the mass of the electron, x is the displacement of the electron from its equilibrium position and ω_0 is the natural frequency of oscillation given by $\sqrt{k_{spring}/m_e}$. This oscillation frequency ω_0 corresponds to the optical transition frequency of the atom. The electric field due to the laser can be expressed in the form

$$\vec{E}(\vec{r}, t) = \hat{e} E(\vec{r}) \exp(-i\omega t) + c.c. \quad (2.91)$$

where E is the magnitude of the electric field, ω is the frequency of the electric field of laser, \hat{e} is the electric charge of the electron and c.c. refers to complex conjugate. The electric field due to the laser induces an oscillating dipole moment $\vec{p}(\vec{r}, t)$ on the electron that oscillates at the same frequency as the driven electron and is expressed by

$$\vec{p}(\vec{r}, t) = \hat{e} p(\vec{r}) \exp(-i\omega t) + c.c. \quad (2.92)$$

where the magnitude of the dipole moment p is related to the electric field via the complex polarisability $\alpha(\omega)$ and is expressed as

$$p = \alpha(\omega)E \quad (2.93)$$

The Lorentz model is useful in arriving at the relevant expressions for the two resulting forces that arise from the coherent and incoherent processes mentioned earlier. While being accelerated by the external laser field, the oscillating

electron loses energy due to dipole radiation at a classical rate

$$\gamma_\omega = \frac{e^2\omega^2}{6\pi\epsilon_0 m_e c^3} \quad (2.94)$$

where m_e is the mass of the electron, ϵ_0 is the permittivity of free space and c is the velocity of light. This loss of energy through radiation by an accelerating charge introduces a velocity dependent damping term in the equation of motion which is given by

$$\ddot{x} + \gamma_\omega \dot{x} + \omega_0^2 x = -\frac{eE(t)}{m_e} \quad (2.95)$$

In the steady state the system oscillates at the driving frequency ω of the external laser field. The time dependent displacement of the electron from its mean position x_0 is given by

$$\vec{x}(t) = \vec{x}_0 \exp(-i\omega t) \quad (2.96)$$

Solving the above equation (2.95) by using equation (2.96) yields the amplitude and the phase of the oscillating dipole with respect to the driving field which can be expressed in terms of the complex polarisability $\alpha(\omega)$ as

$$\alpha(\omega) = \frac{e^2}{m_e} \frac{1}{\omega_0^2 - \omega^2 - i\omega\gamma_\omega} \quad (2.97)$$

The real and imaginary part of the complex polarisability $\alpha(\omega)$ denoted by $Re(\alpha)$ and $Im(\alpha)$ respectively. $Re(\alpha)$ and $Im(\alpha)$ are in turn related to the coherent and the incoherent processes respectively as explained below.

1. **Coherent process:** The electric field drives the atomic transition coherently resulting in an interaction potential between the induced dipole moment

\vec{p} and the electric field \vec{E} given by

$$U_{dipole} = -\frac{1}{2} \langle \vec{p} \cdot \vec{E} \rangle = -\frac{1}{2\epsilon_0 c} \text{Re}(\alpha) I \quad (2.98)$$

where I denotes the intensity of the external laser field. Here $\text{Re}(\alpha)$ describes the strength of the in-phase oscillations of the dipole moment \vec{p} with the oscillations of the electric field \vec{E} . The related force, referred to as dipole force, is found by taking the derivative of the dipole potential:

$$\vec{F}_{dipole} = -\vec{\nabla} U_{dipole}(\vec{r}) = \frac{1}{2\epsilon_0 c} \text{Re}(\alpha) \vec{\nabla} I(\vec{r}) \quad (2.99)$$

An important consequence of the dependence of the dipole force on the gradient of the laser intensity is its use in the optical trapping of neutral atoms [38, 39].

2. Incoherent process: As mentioned earlier, according to the classical picture, the oscillator loses energy by dipole radiation leading to the damping term in equation (2.95). The power emitted by the oscillator and absorbed by the external laser field is given by

$$P_{abs} = \langle \vec{p} \cdot \vec{E} \rangle = 2\omega \text{Im}(pE^*) = \frac{\omega}{\epsilon_0 c} \text{Im}(\alpha) I(\vec{r}) \quad (2.100)$$

The resulting scattering rate denoted by $\gamma_{scatt}(\vec{r})$ can be interpreted in terms of the rate of photons being spontaneously emitted into the laser field and is expressed as

$$\gamma_{scatt}(\vec{r}) = \frac{P_{abs}}{\hbar\omega} = \frac{1}{\hbar\epsilon_0 c} \text{Im}(\alpha) I(\vec{r}) \quad (2.101)$$

An important feature of the spontaneous emission process is its isotropy, that is, it happens with equal probability in any arbitrary direction, and hence can be used to decelerate moving atoms. This is referred to as the

spontaneous force on the atom and will be discussed in detail in the following sub-sections 2.2.4 and 2.2.6.

2.2.4 Optical Bloch equations for a two level atom

The interaction of an atomic system with near-resonant monochromatic radiation can be well described by the optical Bloch equations [40, 41]. The evolution of both the coherences and the populations of a simple two level atomic system can be derived from the Liouville equation (2.65).

The Hamiltonian for a two-level atom interacting with near-monochromatic radiation is given by

$$\mathcal{H} = \mathcal{H}_A + \mathcal{H}_{atom-field} \quad (2.102)$$

where \mathcal{H}_A is the pure atomic Hamiltonian and $\mathcal{H}_{atom-field}$ is the interaction Hamiltonian for the two level atom with the external field. The interaction Hamiltonian $\mathcal{H}_{atom-field}$ is expressed as

$$\mathcal{H}_{atom-field} = -\vec{d} \cdot \vec{E}_l \cos(\omega_l t) \quad (2.103)$$

where $\vec{E}_l \cos(\omega_l t)$ is the external laser field and \vec{d} is the atomic dipole. For the two level atom, the atomic dipole \vec{d} is given by,

$$\vec{d} = \vec{d}_{ba}(|a\rangle\langle b| + |b\rangle\langle a|) \quad (2.104)$$

where $|a\rangle$ and $|b\rangle$ are the excited and the ground states of the two level atom. The excited state $|a\rangle$ can decay to the ground state $|b\rangle$ at a rate $\Gamma_a = \frac{1}{\tau}$, where τ defines the lifetime of the excited state of the atom. We can further define an effective transverse decay rate $\gamma_{ab} = \frac{\Gamma_a + \Gamma_b}{2} + \gamma_c$, where γ_c is the collisional decay rate. Assuming that there is no decay from the ground state $|b\rangle$, the

transverse decay rate γ_{ab} reduces to $(\frac{\Gamma_a}{2} + \gamma_c)$.

Using the density matrix formalism for a two level atom by defining the density matrix operator ρ for a pure state given by

$$\rho = |\psi\rangle\langle\psi| \quad (2.105)$$

where $|\psi\rangle$ is the state under consideration. For the ideal two-level atomic system considered here, $|\psi\rangle$ is given by

$$|\psi\rangle = c_a|a\rangle + c_b|b\rangle \quad (2.106)$$

where c_a and c_b are complex coefficients with the constraint that $|c_a|^2 + |c_b|^2 = 1$. Thus the density matrix ρ for the two level atom can be now written down as

$$\begin{pmatrix} \rho_{aa} & \rho_{ab} \\ \rho_{ba} & \rho_{bb} \end{pmatrix} = \begin{pmatrix} c_a c_a^* & c_a c_b^* \\ c_b c_a^* & c_b c_b^* \end{pmatrix} \quad (2.107)$$

where ρ_{aa} and ρ_{bb} are the populations of the excited and ground states respectively.

Defining the slowly varying coherence terms $\rho_{ab} = \tilde{\rho}_{ab} e^{-i\omega_l t}$ and the detuning Δ_l of the laser field from the atomic resonance as $\Delta_l = \omega_a - \omega_b + \omega_l$, we get the following reduced set of equations by making use of the rotating wave approximation (RWA)

$$\dot{\tilde{\rho}}_{ab} = -(\gamma_{ab} - i\Delta_l)\tilde{\rho}_{ab} + \frac{i\Omega_{ba}}{2}(\rho_{aa} - \rho_{bb}) \quad (2.108a)$$

$$\dot{\rho}_{aa} = \frac{i\Omega_{ba}}{2}(\tilde{\rho}_{ab} - \tilde{\rho}_{ba}) - \Gamma_a \rho_{aa} \quad (2.108b)$$

$$\dot{\rho}_{bb} = \frac{i\Omega_{ba}}{2}(\tilde{\rho}_{ba} - \tilde{\rho}_{ab}) + \Gamma_a \rho_{aa} \quad (2.108c)$$

where $\tilde{\rho}_{ab} = \tilde{\rho}_{ba}^*$. The above set of equations (2.108) are known as the *optical Bloch equations* for the density matrix operator ρ for the two level atomic system. We have further assumed that any effects due to the motion of the atom and decays or couplings to other auxiliary states are negligible in the context of arriving at the set of *optical Bloch equations*. Here Ω_{ba} is the Rabi frequency of the dipole interaction and is defined as

$$\Omega_{ba} = -\frac{\vec{d}_{ba} \cdot \vec{E}_l}{\hbar} = \Gamma_a \sqrt{\frac{I}{2I_s}} \quad (2.109)$$

where I is the intensity of the external laser field while I_s is the saturation intensity of the transition from the ground state $|b\rangle$ to the excited state $|a\rangle$.

Solving the above set of equations for the steady state case (which signifies that $\dot{\rho}_{ab} = \dot{\rho}_{aa} = \dot{\rho}_{bb} = 0$) under the assumption that there are no collisional effects, with the additional constraint that $\rho_{aa} + \rho_{bb} = 1$, we get the following solution for the excited state population

$$\rho_{aa}(t \rightarrow \infty) = \frac{(\Omega_{ba}/\Gamma_a)^2}{1 + 4(\Delta_l/\Gamma_a)^2 + 2(\Omega_{ba}/\Gamma_a)^2} \quad (2.110a)$$

$$= \frac{(s_0/2)}{1 + 4(\Delta_l/\Gamma_a)^2 + s_0} \quad (2.110b)$$

where s_0 is the saturation parameter [42] defined by

$$s_0 = \frac{2|\Omega_{ba}|^2}{\Gamma_a^2} = \frac{I}{I_s} \quad (2.111)$$

With the above value of the excited state population as obtained in equation (2.110) under the steady state approximation, the total photon scattering rate (after integrating over all directions and frequencies) is then given by R_{sc} , which

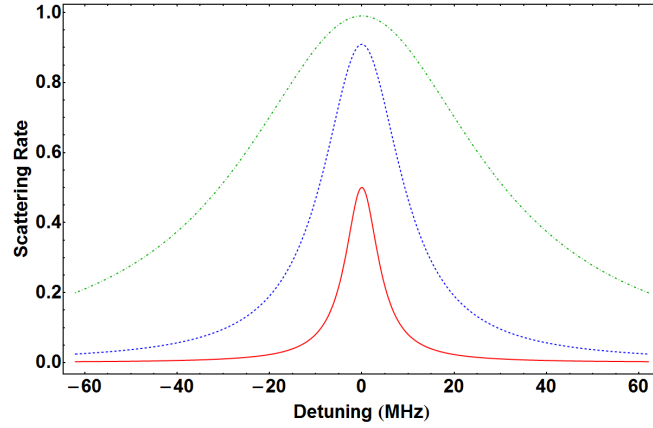


FIGURE 2.19: The scattering rate for a Rubidium (Rb) atom as a function of laser detuning is shown for three different saturation intensity (s_0) ratios with the red (solid) curve for $s_0=1$, the blue (dashed) curve for $s_0 = 10$ and the green (dot-dashed) curve for $s_0 = 100$. All three curves are normalized to the maximal scattering rate of $\Gamma/2$, where Γ is the excited state linewidth for the Rb D_2 transition.

can be expressed as

$$R_{sc} = \Gamma_a \rho_{aa}(t \rightarrow \infty) = \Gamma_a \frac{(\Omega_{ba}/\Gamma_a)^2}{1 + 4(\Delta_l/\Gamma_a)^2 + 2(\Omega_{ba}/\Gamma_a)^2} \quad (2.112)$$

and using equation (2.109), R_{sc} can be re-expressed as

$$R_{sc} = \left(\frac{\Gamma_a}{2}\right) \frac{(I/I_s)}{1 + 4(\Delta_l/\Gamma_a)^2 + (I/I_s)} \quad (2.113)$$

The transition probability for spontaneous emission is also given by the quantity R_{sc} which means that it has a Lorentzian profile of width $\Gamma' = \Gamma_a \sqrt{1 + I/I_s}$, where Γ' is known as the power broadened linewidth of the transition. Thus the observed linewidth of any given transition may be broader compared to its natural linewidth due to saturation effects. A plot of the scattering rate R_{sc} is shown in Fig. 2.19.

Using $I = (1/2)c\epsilon_0 E_l^2$, where E_l represents the magnitude of the electric field

of the external laser field, I_s is given by

$$I_s = \frac{c\epsilon_0\Gamma_a^2\hbar^2}{4|\hat{\epsilon}\cdot\vec{d}|^2} \quad (2.114)$$

where $\hat{\epsilon}$ defines the unit polarization vector of the light field along the direction of propagation, and \vec{d} is the atomic dipole moment. The saturation intensity I_s can be thought of as the photon energy ($\hbar c/\lambda$) per unit time (Γ_a) per unit area (absorption cross-section $\approx \lambda^2$), and can also be represented by the expression

$$I_s = \frac{2\pi^2\hbar\Gamma_a c}{3\lambda^3} = \frac{\pi\hbar c}{3\lambda^3\tau} \quad (2.115)$$

where h is the Planck constant. Putting the appropriate values of the spectroscopic constants for the Rb D_2 transition, we get $I_s = 1.67 \text{ mW/cm}^2$.

2.2.5 AC Stark shifts from external laser field

In the presence of an external field the energy levels of the atom are shifted in energy due to Stark effect caused by the electric field of the external laser field. The light shifts are most readily obtained by first eliminating the time dependence of $\mathcal{H}_{atom-field}$ in (2.103) and then diagonalizing the total Hamiltonian of the atoms in the presence of electromagnetic field (including the interaction of the atom with the electromagnetic field) using the rotating frame transformation approach [42]. The total Hamiltonian \mathcal{H} using this approach thus reduces to

$$\mathcal{H} = \frac{\hbar}{2} \begin{pmatrix} -2\Delta_l & \Omega_{ab} \\ \Omega_{ba} & 0 \end{pmatrix} \quad (2.116)$$

The new values of shifted energies obtained by diagonalizing the above

Hamiltonian in equation (2.116) are given by

$$E_{a,b} = \frac{\hbar}{2}(-\Delta_l \mp \Omega') \quad (2.117)$$

where Ω' is given by $\sqrt{\Omega_{ba}^2 + \Delta_l^2}$. In the limit $\Omega_{ba} \ll \Delta_l$ the resulting light shifts of the ground and excited states are respectively given by

$$\Delta E_b = \frac{\hbar\Omega_{ba}^2}{4\Delta_l} \quad (2.118a)$$

$$\Delta E_a = -\frac{\hbar\Omega_{ba}^2}{4\Delta_l} \quad (2.118b)$$

The nomenclature of above energies as light shifts arise from the fact that the Rabi frequency Ω_{ba} is dependent on the intensity of the external laser field interacting with the two level atom. As seen from the above set of equations (2.118), the light shift of the energy levels is directly proportional to the intensity of the external laser light field and inversely proportional to the detuning of the light field from the atomic transition frequency. In the case of a multilevel atom interacting with an external light field, the light shifts of the various Zeeman sublevels of the ground and excited states depend on the state of polarization of the external light field by different amounts and are given by

$$\Delta E_{m_F} = \pm CG^2 \frac{\hbar\Omega_R^2}{4|\Delta|} \quad (2.119)$$

where CG is Clebsch-Gordan coefficient corresponding to either σ^+ (for which $m_F \rightarrow m_F + 1$) or σ^- (for which $m_F \rightarrow m_F - 1$) transitions, Ω_R is the Rabi frequency of the external light field connecting the two Zeeman sublevels of the two level atom and $|\Delta|$ is the magnitude of the detuning of the external light field from the atomic transition.

2.2.6 Spontaneous force on an atom

The amount of momentum transfer for an atom by the absorption of a photon from an external laser field is given by

$$\Delta \vec{p}_{atom} = \vec{p}_{photon} = \hbar \vec{k} \quad (2.120)$$

where $|\vec{k}| = \frac{2\pi}{\lambda}$, λ denoting the wavelength of the photon. The subsequent spontaneous emission being isotropic in the probability of emission, the time averaged momentum transfer of many cycles cancel each other out and the resulting momentum transfer is zero. Thus the spontaneous force acting on an atom can be expressed as

$$\langle \vec{F}_{sp} \rangle = \hbar \vec{k} R_{sc} \quad (2.121)$$

where R_{sc} is the photon scattering rate defined in the manner as in equation (2.113). It is clear from equation (2.121) that the magnitude of the spontaneous force F_{sp} is proportional both to the natural linewidth and the population of the excited state of the atom. Thus the higher the occupation probability of the excited state, the more number of photons can be exchanged with the ground state in an equilibrium and vice versa. The maximum force achievable is given by

$$F_{max} = \frac{\hbar k \Gamma_a}{2} \quad (2.122)$$

where Γ_a is the linewidth of the excited state, given the maximum value of $\rho_{aa}(t \rightarrow \infty)$ from equation (2.110b) is $\frac{\Gamma_a}{2}$ under the conditions $I \gg I_s$ & $\Delta_l = 0$.

2.2.7 Laser cooling and optical molasses

The physical principles in favor of slowing atoms down with the help of radiation pressure utilizing laser beams were first put forward by Hansch and Schawlow

in 1975 [43] and subsequently developed and enriched by many other physicists [44–47]. For an atom moving with velocity $\pm\vec{v}$ in a laser field with wave vector $+\vec{k}$ detuned by $\delta_0 = \omega - \omega_0$, the atoms effective detuning is changed via the Doppler shift to

$$\delta_{v\pm} = \delta_0 \mp kv \quad (2.123)$$

where ω is the frequency of the laser field, ω_0 is the atomic transition frequency, $k = |\vec{k}| = \frac{2\pi}{\lambda} = \frac{\omega}{c}$ and $v = |\vec{v}|$ is the magnitude of the velocity of the atom.

For a counterpropagating laser beam, the Doppler shift is positive and is given by

$$\delta_{v-} = \delta_0 + \frac{v}{c}\omega \quad (2.124)$$

From the earlier discussions on the spontaneous force on an atom in section 2.2.6, we know that when an atom absorbs a photon, it receives a momentum kick $\hbar\vec{k}$, where k is the wave vector. However given the isotropic nature of spontaneous emission the net change in momentum averaged over many cycles of spontaneous emission is zero. Thus the resulting force from the absorption followed by spontaneous emission is given by [42]

$$F_{spont} = \frac{\hbar k \left(\frac{I}{I_s}\right) (\Gamma/2)}{1 + \frac{I}{I_s} + \left(\frac{2\delta_0}{\Gamma}\right)^2} = \frac{\hbar k s_0 (\Gamma/2)}{1 + s_0 + \left(\frac{2\delta_0}{\Gamma}\right)^2} \quad (2.125)$$

where $s_0 = \frac{I}{I_s}$.

For the case of two counter-propagating laser beams with k -vectors $\pm\vec{k}$, the spontaneous force of both beams adds up to

$$\langle \vec{F} \rangle = \frac{\hbar k \Gamma s_0}{2} \left(\frac{1}{1 + s_0 + \left(\frac{2\delta_{v+}}{\Gamma}\right)^2} - \frac{1}{1 + s_0 + \left(\frac{2\delta_{v-}}{\Gamma}\right)^2} \right) \quad (2.126)$$

which under the assumptions that the detunings are small and that the laser

field intensity is low can be linearized to [48]

$$\langle \vec{F} \rangle \cong \frac{8\hbar k^2 \delta_0 s_0}{\Gamma(1 + s_0 + (\frac{2\delta_0}{\Gamma})^2)} \vec{v} \equiv -\beta v \quad (2.127)$$

where β is the damping coefficient.

For $\delta_0 < 0$, (i.e. for a red detuned laser beam) the force is directed in a direction opposite to the the atomic motion and since $\vec{F} \propto \vec{v}$, the motion of the atom is damped. For large detunings $\delta_0 \gg \Gamma$, the force has two maxima at

$$v = \pm \frac{\delta_0}{k} \quad (2.128)$$

that define a maximum capture velocity for a given atom in motion interacting with a laser field.

With every absorption of a photon, the atom is heated by an amount equal to the recoil energy E_{rec} , where E_{rec} is given by

$$E_{rec} = \frac{\hbar^2 k^2}{2m} = \hbar \omega_r \quad (2.129)$$

where m is the mass of the atom and ω_r defines the angular recoil frequency of the photon. During a single absorption-spontaneous emission cycle, the net change in momentum is only due to the absorption process and hence an energy equal to E_r is transferred to the atom. Within every cycle with two laser beams, the heating rate amounts to $2 \times 2\hbar\omega_r R_{sc}$.

The temperature of the system can be estimated by equating the cooling rate $F(\delta_0).v$ [having units of energy/s] with the heating rate $4\hbar\omega_r R_{sc}$ [which also has units of energy/s]. The resulting temperature for the optical molasses given by

$$k_B T = \frac{\hbar \Gamma}{4} \frac{1 + (\frac{2\delta_0}{\Gamma})^2}{\frac{|\delta_0|}{\Gamma}} \quad (2.130)$$

where k_B is the Boltzmann constant. The temperature has a minimum for $\delta_0 = -\frac{\Gamma}{2}$ which sets a lower limit in temperature for this cooling method. This minimum attainable temperature is known as the Doppler temperature T_{Dopp} and is given by

$$T_{Dopp} = \frac{\hbar\Gamma}{2k_B} \quad (2.131)$$

The Doppler cooling temperature for Rubidium is about $145\mu\text{K}$. For very large detunings, the factor β in equation (2.127) becomes smaller, so the cooling rate $F \cdot v$ decreases. This leads to an increase of the minimum temperature in the molasses. There exist methods for cooling below the Doppler temperature, e.g polarisation gradient cooling which we shall not discuss here.

2.2.8 Magneto-optical trap

The magneto-optical trap (MOT) [8, 49] has been the workhorse of cold atom experimental physicists for the last couple of decades. The magneto-optical trap combines the radiation pressure force obtained from laser beams (which generates optical molasses as discussed in the previous section) with an inhomogenous magnetic field gradient (that can be realized by a pair of current carrying coils in the anti-Helmholtz configuration) to generate a confining as well as a cooling force field to slow down fast moving atoms and confine them spatially at the zero-crossing of the magnetic field lines. Thus it acts as a damped harmonic oscillator potential for the atom and gives rise to a viscous force that is both dependent on space and velocity. A linearly rising magnetic field creates a spatial dependence of the scattering rate and therefore a spatial dependence of the spontaneous force. To address only atoms moving away from the trap centre, counterpropagating circular polarised laser beams are used.

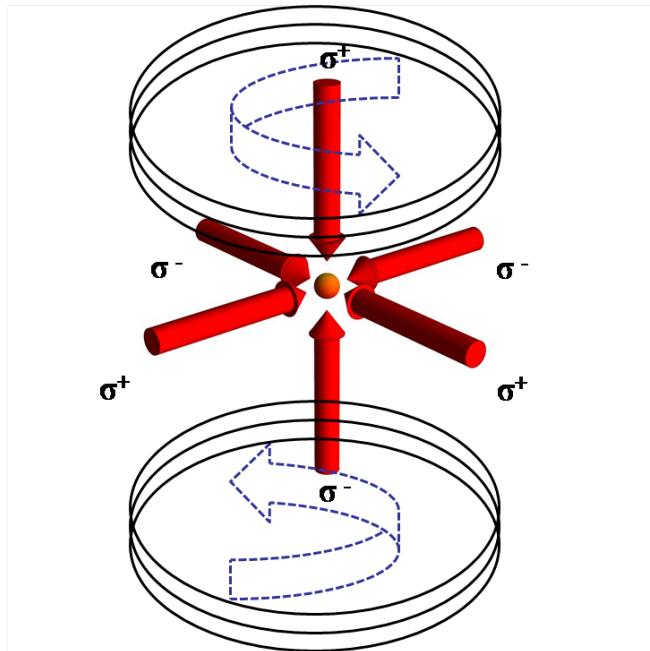


FIGURE 2.20: A schematic of the MOT in three dimensions. Shown in the figure are three pairs of counter-propagating beams with the appropriate sense of polarization. The blue (dashed) lines give the sense of direction of current in the pair of coils depicted as black rings. The small orange dot at the center represents a cloud of cold atoms trapped.

A 3-dimensional potential is required to trap atoms in the MOT. A pair of current carrying coils in the anti-Helmholtz configuration (for creating a quadrupolar field) and three pairs of counter-propagating laser beams with polarizations in the $\sigma^+ - \sigma^-$ configuration are used along three orthogonal directions to realize a magneto-optical trap as shown in Fig. 2.20.

The mathematical treatment of the magneto-optical trap in three dimensions is beyond the scope of the current work reported in this thesis. However, for simplicity, we may refer to the one dimensional case of an atom with ground state $F = 0$ and excited state $F = 1$. In the presence of a linearly inhomogeneous magnetic field (i.e the gradient of the magnetic field scales linearly with distance from the zero crossing of the magnetic field) having the form $B \equiv A \cdot x$, with A being a constant factor giving the gradient of the magnetic field and x the distance, the energy shift of the Zeeman sub-levels of the excited state

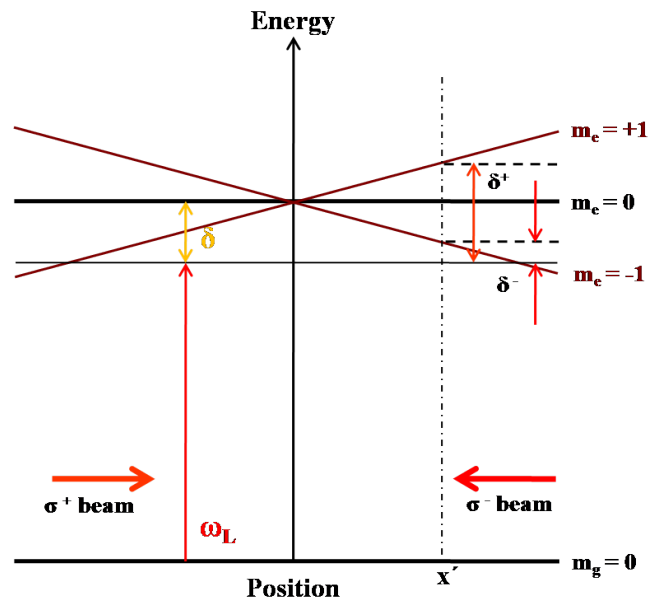


FIGURE 2.21: A schematic of the working principle of the MOT in one dimension. Shown in the figure are three pairs of counter-propagating beams with the appropriate sense of polarization. The blue (dashed) lines give the sense of direction of current in the pair of coils depicted as black rings. The small orange dot at the center represents a cloud of cold atoms trapped.

becomes position dependent as shown in Fig. 2.21.

Referring to the figure Fig. 2.21, at position x' the excited state $m_e = +1$ is shifted up for $B > 0$, whereas $m_e = -1$ is shifted down. So at this position the $\Delta_m = -1$ transition is closer to resonance. As depicted in the figure, the polarization of the laser beam incident from right is σ^- and while the polarization of the beam incident from left is σ^+ . Thus more light is scattered from the σ^- beam than the σ^+ beam which leads to atoms being pushed and confined towards the center. For the region lying to the left of the zero crossing of the magnetic field, more light is scattered from the σ^+ beam than the σ^- beam which again drives the atoms towards the center. Exactly at the zero crossing of the magnetic fields, the force is zero since detuning for both the transitions, resulting from the pair of counter-propagating beams, is the same. This leads to trapping of the atoms. In actual operation of the MOT, the laser light is detuned below the atomic resonance in both the cases leading to simultaneous trapping and

cooling of atoms.

The effective detuning of the atom in the magnetic field is given by

$$\delta_{eff\pm} = \delta_0 \pm kv \mp \frac{\mu' B}{\hbar} \quad (2.132)$$

where $\mu' = \mu_B(g_j^{ex} m_j^{ex} - g_j^{gnd} m_j^{gnd})$. Here the g-s denote the Lande g-factors for the various ground and excited states, while m-s denote the magnetic sublevel values for the ground and excited states. The suffixes gnd and ex stand for the ground and excited states respectively. With the above expression for δ_{eff} , the spontaneous force acting on an atom for small Doppler and Zeeman shifts is proportional both to the velocity and the position of the atom and is expressed as

$$\langle \vec{F} \rangle \cong -\beta \vec{v} - \kappa \vec{x} \quad (2.133)$$

where β is the velocity damping coefficient term expressed as

$$\beta = \frac{8\hbar k^2 \delta_0 s_0}{\Gamma(1 + s_0 + (\frac{2\delta_0}{\Gamma})^2)^2} \quad (2.134)$$

and κ denotes the spring constant of the trap given by

$$\kappa = \frac{\mu' A}{\hbar k} \beta \quad (2.135)$$

Here A denotes the magnitude of the gradient of the magnetic field and is given by $|\frac{\partial B}{\partial x}|$. The trajectories caused by the force given in equation (2.133) are damped harmonic motions of the atoms towards the centre of the trap at an oscillation frequency $\omega_{MOTFreq}$ given by

$$\omega_{MOTFreq} = \sqrt{\kappa/m} \quad (2.136)$$

where m is the mass of the atom.

References

- [1] A. E. Siegman. *Lasers*. University Science Books, Mill Valley, CA, 2003.
- [2] B. E. A. Saleh and M. C. Teich. *Fundamentals Of Photonics*. John Wiley & Sons, Inc., Hoboken, New Jersey, 2007.
- [3] Joseph F. Mulligan. "Who were Fabry and Perot?". *Am. J. Phys.* 66 (9), September 1998.
- [4] Paul R. Berman. (edited) *Cavity quantum electrodynamics - Advances in atomic, molecular, and optical physics*. New York: Academic Press. (1994).
- [5] M. Brune, F. Schmidt-Kaler, A. Maali, J. Dreyer, E. Hagley, J. M. Raimond, and S. Haroche. Quantum Rabi Oscillation: A Direct Test of Field Quantization in a Cavity. *Phys. Rev. Lett.* 76, 18001803 (1996).
- [6] K. Baumann, R. Mottl, F. Brennecke, and T. Esslinger. Exploring Symmetry Breaking at the Dicke Quantum Phase Transition. *Phys. Rev. Lett.* 107, 140402 (2011).
- [7] J. Bernu, S. Deleglise, C. Sayrin, S. Kuhr, I. Dotsenko, M. Brune, J. M. Raimond, and S. Haroche. Freezing Coherent Field Growth in a Cavity by the Quantum Zeno Effect. *Phys. Rev. Lett.* 101, 180402 (2008).

-
- [8] Haruka Tanji-Suzuki, Wenlan Chen, Renate Landig, Jonathan Simon, and Vladan Vuletic. Vacuum-Induced Transparency. *Science*. 333, 1266 (2011).
- [9] H. Kogelnik and T. Li. Laser Beams and Resonators. *Proc. of IEEE*. 54, 1312-1329 (1966).
- [10] E. Jaynes and F. Cummings. Comparison of quantum and semiclassical radiation theories with application to the beam maser. *Proc. IEEE*. 51 (1): 89109. (1963).
- [11] M. O. Scully and M. S. Zubairy. *Quantum optics*, Cambridge University Press. 1997.
- [12] M. Tavis and F. W. Cummings. Exact Solution for an N-Molecule Radiation-Field Hamiltonian. *Phys. Rev.* 170, 379384 (1968).
- [13] H. Carmichael. *An open systems approach to quantum optics*. Springer 1993.
- [14] K. Murr. On the suppression of the diffusion and the quantum nature of a cavity mode. Optical bistability: forces and friction in driven cavities. *J. Phys. B*. 36, 2515 (2003).
- [15] R. J. Thompson, G. Rempe, and H. J. Kimble. Observation of normal-mode splitting for an atom in an optical cavity. *Phys. Rev. Lett.* 68, 1132 (1992).
- [16] J. J. Childs, K. An, M. S. Otteson, R. R. Dasari, and M. S. Feld. Normal-mode line shapes for atoms in standing-wave optical resonators. *Phys. Rev. Lett.* 77, 2901-2904 (1996).
- [17] J. Gripp, S. L. Mielke, and L. A. Orozco. Evolution of the vacuum Rabi peaks in a detuned atom-cavity system. *Phys. Rev. A*. 56, 3262-3273 (1997).

-
- [18] P. Maunz, T. Puppe, I. Schuster, N. Syassen, P. W. H. Pinkse, and G. Rempe. Normal-mode spectroscopy of a single-bound-atom-cavity system. *Phys. Rev. Lett.* 94, 033002 (2005).
- [19] A. Boca, R. Miller, K. M. Birnbaum, A. D. Boozer, J. McKeever, and H. J. Kimble. Observation of the Vacuum Rabi Spectrum for One Trapped Atom. *Phys. Rev. Lett.* 93, 233603 (2004).
- [20] T. Puppe, I. Schuster, A. Grothe, A. Kubanek, K. Murr, P. W. H. Pinkse, and G. Rempe. Trapping and observing single atoms in a blue-detuned intracavity dipole trap. *Phys. Rev. Lett.* 99, 013002 (2007).
- [21] Yves Colombe, Tilo Steinmetz, Guilhem Dubois, Felix Linke, David Hunger, and Jakob Reichel. Strong atom-field coupling for Bose-Einstein condensates in an optical cavity on a chip. *Nature.* 450, 272-276 (2007).
- [22] Ferdinand Brennecke, Tobias Donner, Stephan Ritter, Thomas Bourdel, Michael Kohl, and Tilman Esslinger. Cavity QED with a Bose-Einstein condensate. *Nature.* 450, 268-271 (2007).
- [23] J. P. Reithmaier, G. Sek, A. Löffler, C. Hofmann, S. Kuhn, S. Reitzenstein, L. V. Keldysh, V. D. Kulakovskii, T. L. Reinecke, and A. Forchel. Strong coupling in a single quantum dot-semiconductor microcavity system. *Nature.* 432, 197-200 (2004).
- [24] David Press, Stephan Gotzinger, Stephan Reitzenstein, Carolin Hofmann, Andreas Löffler, Martin Kamp, Alfred Forchel, and Yoshihisa Yamamoto. Photon antibunching from a single quantum-dot-microcavity system in the strong coupling regime. *Phys. Rev. Lett.* 98, 117402 (2007).
- [25] E. Peter, P. Senellart, D. Martrou, A. Lemaitre, J. Hours, J. M. Gerard, and J. Bloch. Exciton-photon strong-coupling regime for a single quantum dot embedded in a microcavity. *Phys. Rev. Lett.* 95, 067401 (2005).

-
- [26] T. Yoshie, A. Scherer, J. Hendrickson, G. Khitrova, H. M. Gibbs, G. Rupper, C. Ell, O. B. Shchekin, and D. G. Deppe. Vacuum Rabi splitting with a single quantum dot in a photonic crystal nanocavity. *Nature*. 432, 200-203 (2004).
- [27] H. J. Carmichael. Quantum fluctuations in absorptive bistability without adiabatic elimination. *Phys. Rev. A*. 33, 3262 (1986).
- [28] Yifu Zhu, Daniel J. Gauthier, S. E. Morin, Qilin Wu, H. J. Carmichael, and T. W. Mossberg. Vacuum Rabi splitting as a feature of linear-dispersion theory: Analysis and experimental observations. *Phys. Rev. Lett.* 64, 2499 (1990).
- [29] J. Gripp and L. A. Orozco. Evolution of the vacuum Rabi peaks in a many-atom system. *Quantum Semiclassic. Opt.* 8, 823 (1996).
- [30] H. J. Kimble. Strong interactions of single atoms and photons in cavity QED. *Physica Scripta*. Vol. T76, 127-137, 1998.
- [31] J. Fortagh, A. Grossmann, T. W. Hansch and C. Zimmermann. Fast loading of a magneto-optical trap from a pulsed thermal source. *J. App. Phys.* 84 6499 (1998).
- [32] U. D. Rapol, A. Wasan and V. Natarajan. Loading of a Rb magneto-optical trap from a getter source. *Phys. Rev. A*. 64 023402 (2001).
- [33] K. L. Moore, T. P. Purdy, K. W. Murch, S. Leslie, S. Gupta and D M Stamper-Kurn. Collimated, single-pass atom source from a pulsed alkali metal dispenser for laser cooling experiments. *Rev. Sci. Instrum.* 76, 023106 (2005).
- [34] C. B. Alcock, V. P. Itkin, and M. K. Horrigan. Vapor Pressure Equations for the Metallic Elements: 2982500 K. *Canadian Metallurgical Quarterly*. 23, 309 (1984).

-
- [35] A. Corney. *Atomic and Laser Spectroscopy*. Oxford: Clarendon Press (1997).
- [36] G. Breit and I.I. Rabi. Measurement of Nuclear Spin. *Phys. Rev.* 38, 2082 (1931).
- [37] Rudolf Grimm, Matthias Weidemuller and Yurii B. Ovchinnikov. Optical dipole traps for neutral atoms. *Adv. At. Mol. Opt. Phys.*, Vol. 42, 95-170, 2000.
- [38] Arthur Ashkin. Optical trapping and manipulation of neutral particles using lasers. *PNAS*. Vol. 94 No. 10 4853-4860, May 13, 1997.
- [39] Arthur Ashkin. *Optical Trapping and Manipulation of Neutral Particles Using Lasers: A Reprint Volume With Commentaries*. World Scientific Publishing Company. (December 29, 2006).
- [40] R. Loudon. *The Quantum Theory of Light*. Oxford University Press. (2nd ed., 1983).
- [41] L. Allen and J. H. Eberly. *Optical Resonance and Two-Level Atoms*. Dover Publications. (December 1, 1987).
- [42] H. J. Metcalf and P. van der Straten. *Laser Cooling and Trapping*. Berlin: Springer (1999).
- [43] T.W. Hansch and A.L. Schawlow. Cooling of Gases by Laser Radiation. *Opt. Comm.* 13, 68 (1975).
- [44] V.S. Letokhov, V.G. Minogin and B.D. Pavlik. Cooling and capture of atoms and molecules by a resonant light field. *Sov. Phys. JETP* 45, 698 (1977).
- [45] D. J. Wineland and W. Itano. Laser cooling of atoms. *Phys. Rev. A*. 20, 15211540 (1979).

- [46] J. P. Gordon and A. Ashkin. Motion of atoms in a radiation trap. *Phys. Rev. A.* 21, 16061617 (1980).
- [47] Richard J. Cook. Theory of resonance-radiation pressure. *Phys. Rev. A.* 22, 10781098 (1980).
- [48] P. D. Lett, W. D. Phillips, S. L. Rolston, C. E. Tanner, R. N. Watts, and C. I. Westbrook. Optical molasses. *JOSA B.* Vol. 6, Issue 11, pp. 2084-2107 (1989).
- [49] E. L. Raab, M. Prentiss, Alex Cable, Steven Chu, and D. E. Pritchard. Trapping of Neutral Sodium Atoms with Radiation Pressure. *Phys. Rev. Lett.* 59, 2631-2634 (1987).
- [50] C. Monroe, W. Swann, H. Robinson, and C. Wieman. Very cold trapped atoms in a vapor cell. *Phys. Rev. Lett.* 65, 1571-1574 (1990).

3

Cavity based all optical switching in room temperature atomic vapor

3.1 Experiments using a vapor cell cavity at room temperature

The presence of an optically interacting medium within a Fabry-Perot (FP) cavity alters the conditions under which the discrete modes of light are supported [1]. Specifically absorption [2], dispersion [3], scattering [4], non-linear [5, 6] effects can occur due to the interaction of the EM field supported by the cavity mode, with the intra-cavity medium. The signature of the light-matter interaction in the cavity can be detected in the light coupled out of the cavity.

Atoms in cavities with resonant light fields have given rise to rich physics over the past several decades. An important class of experiments has dealt

with a low finesse cavity built around atomic vapor, representative of the weak coupling limit ($g \ll \kappa, \Gamma$). The atomic vapor can be contained either in vapor cells, a well defined beam or be a trapped gas of cold atoms or ions. The cavity itself can either be a ring (traveling wave) cavity [7–9] or a standing wave cavity [10]. Further differentiation is possible based on the number of transitions and the detunings of the light fields involved in the cavity mediated atom-light interaction. All these aspects demonstrate both the variety of experimental approaches possible and the different ways that this complex, interacting system can be studied.

A lot of experiments with atomic vapor in cavities have used spectroscopic cells of various descriptions. Due to the presence of the two glass faces of the cell, an input beam encounters four surfaces while making a single pass along the cavity axis for a cavity built around the cell. This fact as well as the varying glass surface quality of the vapor cells makes for a relatively poor cavity due to multiple etaloning by the presence of each surface. However the system is still capable of supporting cavity modes and the relatively modest experimental requirements for manufacturing such an atom cavity system makes this an attractive experimental system for a variety of physical phenomena such as bistability [11–21], switching [22] and non-linear processes [23].

This chapter focuses on the changes in cavity transmission when a four level atomic system defined by the geometry of the experimental set-up (explained subsequently in section 3.4), having two ground states is acted upon by two frequencies of resonant light, one of which is coupled into the cavity mode. The D_2 transitions of ^{87}Rb , which connect the ground states $5^2S_{1/2}$ ($F=1$ and $F=2$) to the excited states $5^2P_{3/2}$ ($F'=2$ and $F'=3$ respectively), define an effective four level level system, if we ignore the two other states in the excited state manifold. Coupling one of these frequencies into the standing wave cavity such that the cavity transmits sets up the experiment. Two cases have been investigated using a very weak control beam (which the beam transverse to the cavity axis)

either on the same or on a different transition as the probe beam (which is light the beam along the cavity axis). Intersecting the light-atom system in the cavity mode via the control beam can manipulate the intensity of the light transmitted by the cavity very effectively.

If the probe and control beams are operated on different transitions, then we refer to the switching mechanism as “negative”logic switching. However, if the probe and control are on the same transition then we refer to it as “positive”logic. In section 3.2 we shall briefly describe what constitutes an all optical switch. In section 3.3 we shall briefly review previous research on all optical switches. In section 3.4 we shall introduce the experimental apparatus, describe the cavity characterization and optical system set-up relevant for negative logic switching, follow it up with the experiments performed in relation to the negative logic switching and conclude with results and discussions. Both steady state and transient changes in the transmitted intensity are recorded for both cases of operation. Then in section 3.5 we shall present the experimental set-up and results for positive logic switching and compare the results with the negative logic switching experiments discussed in the previous section. In section 3.6 we shall discuss the physical process behind the operation of the switching mechanism by invoking a simple model. Finally in section 3.7, we shall conclude by discussing the results of both switching experiments in the context of all optical switching utilizing a vapor cell encompassed within an optical cavity.

3.2 All optical switching

A device that provides the possibility of altering or manipulating the state of one light beam by using another beam can be defined as an all optical switch. For the device to act as an optical switch four very basic criterion need to be satisfied: (a) the device must exhibit at least two distinguishable states and

(b) it should have input-output isolation, (c) it should allow cascadability so that the issue of scalability can be addressed, and finally (d) the device should ensure signal level restoration which essentially signifies that the output level of the device should be independent of the variations at the input level. There exists a variety of possible configurations where the optical switch can alter the output power, direction, or state of polarization of a beam of light that is either propagating through a nonlinear medium or generated within the medium.

One of the simplest all-optical switches conceived and demonstrated in a wide variety of materials makes use of the nonlinear phase shift that arises due to a intensity-dependent refractive index of the nonlinear optical medium and this nonlinear change in phase is experienced by any wave propagating through such a transparent media. This phenomena provides the basis for control of light by light if such a medium is inserted in one arm of an interferometer [24]. The output state of the interferometer could then be altered by changing the phase shift experienced by one beam which physically signifies changing the optical path length of one arm of the interferometer. The nonlinear phase shift is completely dependent on the total optical intensity incident on the nonlinear material assuming a constant length of the nonlinear optical medium. Thus if a strong control field of intensity I_c is applied, and assuming the signal field I_{signal} is weak ($I_{signal} \ll I_c$), the nonlinear phase shift ϕ_{nl} is given by

$$\phi_{nl} = 2 \frac{\omega_c}{c} n_2 I_c L \quad (3.1)$$

where ω_c is the angular frequency of the control beam, c is the speed of light in vacuum, L is the length of the medium and n_2 is the nonlinear index of refraction. To demonstrate high-contrast switching, the control beam must be of sufficient strength to cause a significant change in the nonlinear phase ϕ_{nl} of the signal beam, $\phi_{nl} \sim \pi$.

A second type of all-optical switch can be realized utilizing the absorption properties of a saturable absorber. The absorption experienced by a wave

propagating through a homogeneously broadened medium exhibiting saturable absorption depends only on the intensity I , and decreases for increasing intensity [24]. This behavior can be expressed by the following equation

$$\alpha = \frac{\alpha_0}{1 + \frac{I}{I_{sat}}} \quad (3.2)$$

where α_0 is the absorption coefficient experienced by a weak field and I_{sat} is the saturation intensity. The realization of an optical switch based on saturable absorption is possible when a strong control beam (of sufficient intensity capable of saturating the atomic response of the medium) and a weak signal beam copropagate through a saturable absorber. Physically saturation of a two-level system implies transferring a significant amount of the atomic population from the ground state to the excited state. In order to maintain an effective population in the excited state, one photon must be incident on each atom per excited state lifetime. We can express the afore-mentioned condition [25] as

$$I = I_{sat} = \frac{\hbar\omega}{\sigma\tau_{sp}} \quad (3.3)$$

where τ_{sp} is the excited state lifetime, $\hbar\omega$ is the photon energy for a photon with frequency ω , and σ is the atomic cross section. However equation (3.3) must be modified suitably to account for optical pumping in a material where the population is redistributed in time according to the ground-state lifetime τ_g . There are also other types of all optical switches that have been demonstrated in the community which have been discussed in section 3.3.

3.3 Brief overview of past research on all optical switching

In general, although the simplest realization of an all optical switch is possible as per the discussion in the previous section, we shall briefly review some of the important state of the art experiments in the field of all optical switches that have been demonstrated in the community. The current discussion gives a perspective of the experimental goals and technical issues that are of primary importance and interest in the context of all optical switches. There are two basic pathways to low light level optical switching and both of them try to amplify the the coupling between light and matter governed by non-linear interactions between the two afore-mentioned entities. The first approach relies on the strong coupling of an atom with the field when placed inside a high finesse cavity. One can also utilize the optical bistability phenomenon even in relatively poor cavities to design an optical switch between the two steady states of the bistable curve by adding relevant fields to the cavity intensity. The other approach makes use of traveling waves which have the potential to articulate quantum interferences within the optical medium and thus increase significantly the effects of light on matter.

In the strong coupling regime of cavity quantum-electrodynamics (QED) systems an extremely small number of photons are required to saturate the response of an atom coupled to the mode of the cavity. Thus a cavity QED system operating in the strong coupling regime offers very high sensitivity by saturating the nonlinear optical response of the atom coupled to the cavity mode and can ensure complete transmission through the cavity with just 10 intra-cavity photons [26] in the presence of the atom. Working in a similar regime one can also observe an effect known as photon blockade which physically implies that the two-photon absorption process is suppressed due to the resonance of a single-photon process with the lowest excited dressed-state of

the atom-cavity system [27]. Cavity QED systems thus offer unprecedented sensitivity at the single atom single photon level but are limited by the number of available input/output channels which are usually restricted to one per polarization since these systems are designed to operate with the field of a single mode inside the cavity. These systems are also not easily cascadable (which ensures that the output of one device must be able to drive two or more subsequent inputs for other devices) and hence do not meet the all important aspect of scalability with regards to optical switches.

A different mechanism for all optical switching is through the creation and control of cavity solitons using vertical cavity surface emitting lasers (VCSELs) as the nonlinear cavity [28]. A combination of beams (one wide “holding” beam and one narrow “write” beam) traversing along the cavity axis induces a cavity soliton. Since the solitons usually persist until the holding beam is turned off this system has the natural ability to serve as an optical memory. Cavity soliton systems have been primarily limited by lower sensitivity. Typical powers for the hold and write beams for such systems are in the range of a few mW and order of 200 μ W respectively. However these systems are not easily cascadable due to low power output of each cavity soliton that would be required to seed solitons in two or more subsequent devices. Added technical complexities may then arise while imaging the output soliton into a second cavity. The solution to this issue has so far eluded the optics community at large.

The other approach in the context of optical cavities relies on a combination of the field enhancement offered by optical cavities and the strong coupling of coherently prepared atoms. Bistability switching in the output of a cavity filled with a large-Kerr, EIT medium [23] is demonstrated with high fidelity, but requires higher input power of about a mW and exhibits microsecond time responses. Bistable switching has also been demonstrated in photonic crystal nanocavities [29] with about 75 fJ pulses and switching speeds of <100 ps.

The fourth method of utilizing traveling waves using the techniques of electromagnetically induced transparency (EIT) [28, 30–33, 35] also allows one to operate the optical switch with multi-mode optical fields and achieve few-photon sensitivity. For example, Harris and Yamamoto [36] suggested a switching scheme based on narrow atomic resonances (whose experimental realization is the primary hurdle) using the strong non-linearities that exist in specific states of four-level atoms. In such four level atomic systems it is possible for a single photon at one frequency to cause the absorption of light at another frequency in the ideal limit. The above scheme has been implemented by Braje et al. [35] who first observed all-optical switching in an EIT medium with an input energy density of about $1\mu\text{W}$ per square mm. Zhang et al. [30] recently observed switching with just 20 photons using a modified version of the Harris-Yamamoto scheme by using an extra EIT coupling field that causes additional quantum interference. In spite of the sensitivity achieved in these systems at a few photon level these systems suffer from limited cascability given the fact that the input and output fields are required to have the same power.

A final approach to all optical switching from transverse optical patterns was demonstrated by Dawes et al. [37]. Here they exploited the formation of transverse optical patterns that arise from the collective instabilities which occur when a pair of laser beams counterpropagate through a non-linear medium like an atomic vapor. Such instabilities are in general very sensitive to perturbations and thus by combining instabilities with resonantly-enhanced, sub-Doppler nonlinearities, they have created an optical switch with very high sensitivity. Though operationally the switch operates with $<1\text{mW}$ of pump power, the issue of scalability and sensitivity can be addressed in a larger context here.

Our experiment with the vapor cell cavity utilizes the saturation effects in Rubidium (Rb) vapor to manipulate the transmission of an optical cavity with the aid of an external control beam. We have made a conscious choice of the

^{87}Rb D_2 transitions to demonstrate all optical switching phenomena so that we can relate it to switching experiments that can be realized with a cloud of cold atoms trapped in a magneto-optical trap (MOT).

3.4 Experimental arrangement and setup for negative logic switching

3.4.1 Cavity Assembly

The experimental arrangement is as follows. A cylindrical spectroscopy cell (Triad Technologies Inc.) containing an enriched sample of ^{87}Rb , 75 mm in length and 25 mm diameter is inserted within a non-confocal Fabry-Perot (FP) cavity. The cavity mirrors have a manufacturer specified reflectivity $R = 99.97\%$ at 780 nm and an experimentally measured reflectivity of $R_{exp} = 99.98 \pm 0.01$. The radius of curvature of both the concave mirrors is 250 mm. The distance between the mirror surfaces of the cavity is ≈ 80 mm. One FP mirror is directly glued onto one of the parallel end faces of the cell, while the other mirror is glued onto an annular piezoelectric transducer, which is in turn glued onto the opposite face of the Rb cell. Care is required in cavity construction to ensure the two FP mirrors share a common cylindrical axis.

3.4.2 Optical System Setup

At room temperature, due to doppler broadening, the excited $5^2P_{3/2}(F')$ manifold of ^{87}Rb is unresolved. However given the counter propagating nature of the beams present in the cell cavity system that arise due to back and forth reflection of the beams along the cavity axis from the cavity mirrors, the first order Doppler effect is eliminated. The system can be treated as an effective

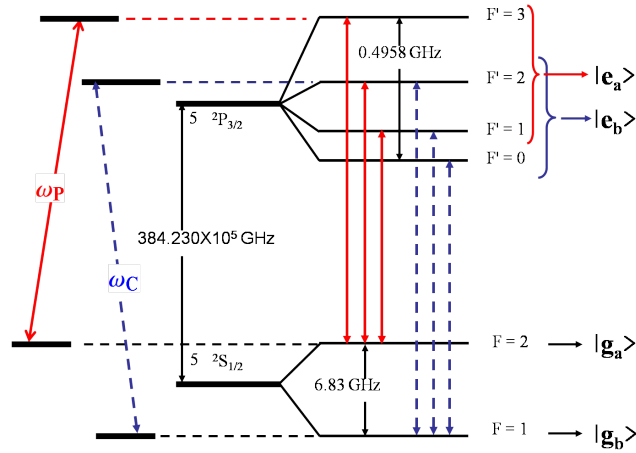


FIGURE 3.1: Left: The schematic depicts a simplified four level system of the ^{87}Rb $5S_{1/2}$ and the $5P_{3/2}$ and energy levels. Right: The full hyperfine level splittings with the dipole allowed transitions are shown for the ^{87}Rb D_2 transition.

four level system comprising the resolved $5^2S_{1/2}$, F=1 and F=2 ground states and the excited states F'=2 and F'=3 of the $5^2P_{3/2}$ manifold, as illustrated in Fig. 3.1, given the fact that the system is being driven experimentally using two independent extended cavity diode laser (ECDL) systems.

To drive the four level system as shown in Fig. 3.1 between the two hyperfine ground states and the $5^2P_{3/2}$ excited state manifold, two independent extended cavity diode lasers (ECDL) are set up. The lasers can be tuned individually to the appropriate transitions of the ^{87}Rb (Rubidium) D_2 manifold relevant to the experiment as shown in Fig. 3.1. The laser coupled into the cavity mode is identified as the probe(coupling) laser, with frequency ω_p and intensity I_p . The probe laser is passed through an acousto-optic modulator (AOM), followed by transmission through a single-mode polarization maintaining fiber to produce a linearly polarized TEM_{00} beam and finally mode-matched into the cavity. The intensity of the probe beam I_p is controlled and adjusted by the AOM and its polarization can be adjusted using a half-wave ($\frac{\lambda}{2}$) plate placed before the mode matching lens of the cavity. The second laser which intersects the probe beam in a small region of the cavity mode is referred to as the control(switching) laser. The control laser alters the transmission of the probe light through the

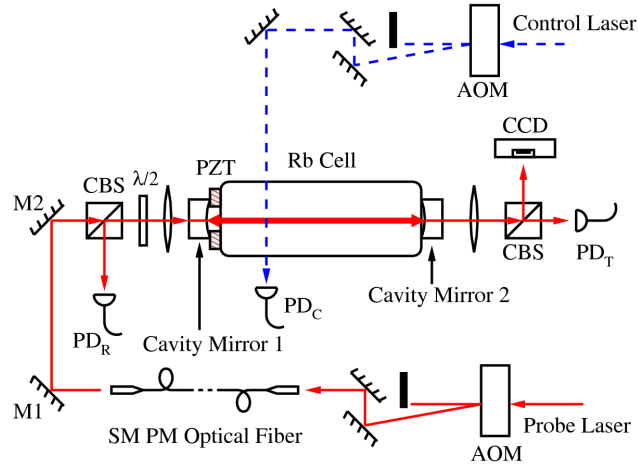


FIGURE 3.2: Schematic of the experimental setup. The FP cavity with the ^{87}Rb cell is shown. Two beams on the complimentary D2 transitions are shown. One beam (solid line) is coupled into the cavity and the transmission and reflection ports are monitored using the photodiodes PD_T and PD_R respectively. The spatial profile of the transmitted mode is captured using a CCD camera. The other beam (dashed line) intersects the cavity mode in transverse geometry over a small volume of the cavity mode and is monitored using PD_C . Switching of the two beams is done using AOM's as shown.

cavity. The control laser has frequency ω_c and an intensity I_c and is operated in a manner similar to the probe beam, as shown in Fig. 3.2.

The resonant light transmission through the cavity is set-up as follows. Laser light that is scanning across the Rb D₂ transition is coupled into the cavity. Initial poor alignment results in small transmission peaks in the off resonant part of the Rb spectrum, while at resonance only the doppler broadened absorption is seen in the transmitted light. The poor alignment also raises the baseline of the light level detected by the photo-diode in transmission (PD_T). Where the periodic cavity transmission peaks should coincide with the doppler broadened absorption, no increased transmission results. As the light coupled into the cavity increases, either due to better alignment or increase in input intensity or both, the amplitude of the cavity transmission peaks goes up steadily in the non resonant region of the spectrum. Within the absorption dip the phenomenon is quite different. For poor alignment a regular doppler broadened absorption

profile is obtained in transmission over the elevated background. As the coupling into the cavity mode improves, distortions manifests in the doppler profile at the transmission periodicity of the cavity.

Optimizing cavity coupling is an iterative process combining alignment and probe intensity changes. With only slight changes in alignment a large change in cavity transmission occurs on the cavity resonance within the absorption profile, when the Rb atoms in the mode are saturated. This has two consequences on the transmission of the probe laser light through the cavity. First, the cavity transmission peaks that coincide with the absorption grow relative to the peaks in the non-absorbing part of the Rb spectrum. Second, the absorption dip in the transmission signal vanishes as the alignment improves, which also results in a very low baseline light levels measured in PD_T and a larger intra-cavity light intensity on the cavity resonance. The lower baseline occurs over the entire scan range of the D_2 resonance in ^{87}Rb . Once this condition is achieved, the laser coupled into the cavity mode is set to be resonant with the maximum of the doppler broadened D_2 absorption, i.e. the $5^2S_{1/2}(F=2)$ hyperfine state to the excited $5^2P_{3/2}(F')$ manifold of ^{87}Rb . The frequency of this laser can be set with an accuracy of a few MHz. The cavity piezo is then scanned with a saw-tooth wave of 50% duty cycle to change the length of the cavity, while the probe frequency is nearly constant with time. The transmission property of the cavity is now a function of the cavity length and periodic transmission peaks are seen with the expansion and contraction of the piezo controlled cavity. This is illustrated in Fig. 3.3.

The probe(coupling) beam is identified with labels ω_p and I_p whereas the control(switching) beam labels are ω_c and I_c , as shown in Fig. 3.1. The control beam of $\approx 2\text{mm}$ diameter intersects the probe beam within the cavity mode with small overlap volume, as illustrated in Fig. 3.2. The rest of the experiments concern the consequence of the overlap of these two resonant beams within the cavity mode.

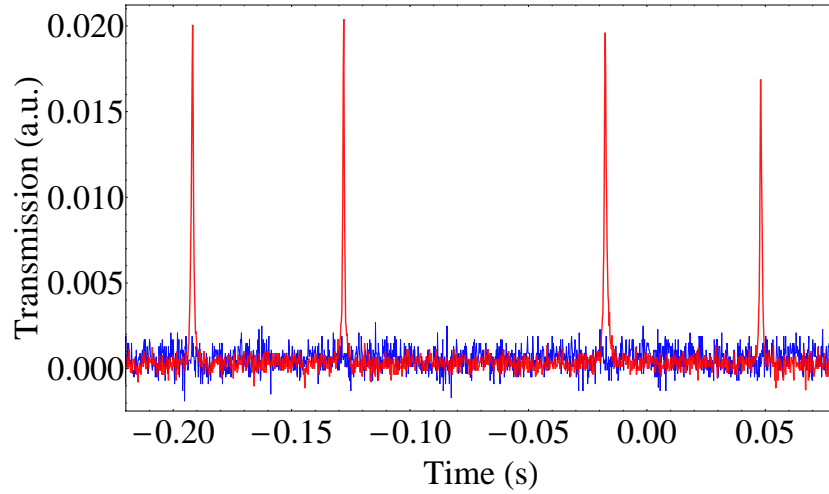


FIGURE 3.3: The cavity transmission of probe light as a function of the cavity length is illustrated by the thin (red) trace. Both the expansion and contraction cycle are shown. When the control light is incident on the cavity mode from the orthogonal direction, we see the complete suppression of the cavity transmission peaks shown as the thick (blue) trace. The transmission has been extinguished and not been shifted in frequency.

For the probe laser frequency ω_p tuned to the $5^2S_{1/2}(F=2) \rightarrow 5^2P_{3/2}(F'=3)$ transition, the frequency of the control laser ω_c is tuned to the $5^2S_{1/2}(F=1) \rightarrow 5^2P_{3/2}(F'=2)$ transition. The choice of transitions for the probe and control laser can be reversed, with no qualitative change in the experimental results. Both lasers are temperature stabilized with relatively narrow linewidth. Neither laser is locked to a specific ^{87}Rb transition. The long term drift of the lasers is of the order of 20 MHz/hr. The control lasers is arranged to intersect the cavity mode in an approximately transverse geometry. The diameter of the control laser beam is $\approx 1.5\text{mm}$, and so it intersects the cavity mode, which is 75 mm long, over a small fraction of its length as is illustrated in Fig. 3.2. A very weak beam of the control laser, is all that is required to destroy the transmission property of the cavity completely. The cavity is now setup for the intensity control of the cavity transmission of the probe light.

3.4.3 Cavity Characterization

The transmitted intensity of the probe laser through the cavity needs characterization before its control is studied. How good the cavity is as an optical filter, in transmission, is given by its finesse F , which is the ratio of the cavity free spectral range $\Delta\nu_{FSR}$ to the linewidth of the resonance $\Delta\nu_{FWHM}$ supported by the cavity. Experimentally $\Delta\nu_{FSR}$ is the distance after which the cavity mode repeats itself as the cavity length is scanned. For the Rb loaded cavity the ratio of the measured finesse F_r on resonance to the measured value of finesse off resonance F_{nr} is $\frac{F_r}{F_{nr}} \approx 2$. The value of F_r , which ranges from $50 < F_r < 110$, depends mainly on the construction of the cavity and to a small extent on the alignment of the probe beam. $F_r > F_{nr}$ indicates that the round trip loss of intensity in the cavity mode is partially compensated by the round trip gain, due to the presence of the ^{87}Rb in the cavity mode. It should be noted that, on resonance, additional round trip loss is incurred due to the fluorescence of the atoms in the cavity mode and despite this F_r increases. The cavity arrangement is illustrated in Fig. 3.2.

The rate of growth and decay of the probe light in the cavity mode is shown in Fig. 3.4. The cavity length is adjusted by the piezo so as to zoom on a cavity peak such that maximum, constant cavity transmission is achieved with time. The probe light coupled into the fiber is the first order of the AOM diffracted beam. Turning OFF and ON the drive radiofrequency (RF) power into the AOM offers complete control on the light intensity in the first order beam, so that $\text{RF}_{ON} \Rightarrow$ probe coupled into cavity. The AOM switching time off $\approx 150\text{ns}$ and the gain bandwidth product of the photodiodes limit the accurate measurement of the fast time constants. However the ON resonance, slow rise time measurement is unaffected and is therefore accurate. When RF is switched OFF, the first order of the AOM beam decays, and likewise the transmitted probe intensity. The measured decay time is sub-microsecond for both the OFF resonance Fig. 3.4(a) and the ON resonance Fig. 3.4(b) case. When the RF power to the

3.4 EXPERIMENTAL ARRANGEMENT AND SETUP FOR NEGATIVE LOGIC SWITCHING

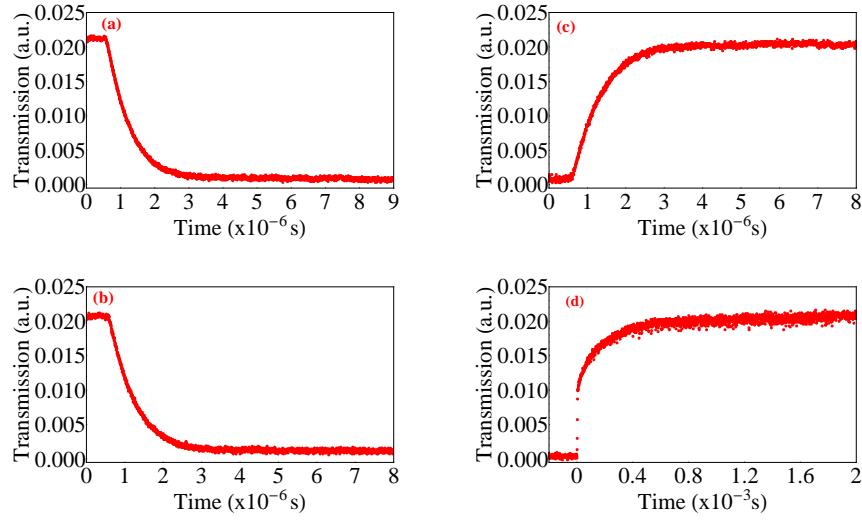


FIGURE 3.4: The measured decay and rise of the cavity transmission for the probe, ON and OFF resonance, is shown. The decay of the steady state intensity, measured in transmission for the OFF resonance case is (a), and the ON resonance case (b). In both cases the fall time has sub microsecond time constants. The rise in the transmitted intensity OFF and ON resonance are shown in (c) and (d) respectively. Here the rise time constant for the OFF resonant case is sub microsecond, whereas for the the ON resonance case it is greater than 100 μ s.

AOM is switched ON from the OFF state, the OFF resonance transmission rise time is once again sub-microsecond, as shown in Fig. 3.4(c). However, in the ON resonance situation, the transmitted light intensity rise time is orders of magnitude slower with a time constant $\tau_{rt} \approx 180\mu$ s, as in Fig. 3.4(d).

A large rise time for cavity transmission, when the light is ON resonance with the atoms in the cavity, implies a corresponding build up time for intra-cavity intensity. The long time scale associated with the build up of intra-cavity intensity can be directly related to the strength of the resonance between the atoms and the incident beam along the cavity axis. The stronger this resonance, the greater is the rate of resonant scattering by the atoms from the cavity mode and hence the longer build up time for the intracavity intensity. Thus it is expected that the build up time of the intra-cavity intensity for the repumping transition $\{5^2S_{\frac{1}{2}}(F=1) \rightarrow 5^2P_{\frac{3}{2}}(F'=2)\}$ of ^{87}Rb is smaller than the intra-cavity build up time

Table 3.1: Rise and fall time constants without control beam. The data are fit to single exponential decay form and time constants mentioned with standard deviation as the error bar.

Probe Frequency	Rise Time (μs)	Fall Time (μs)
$^{85}\text{Rb } 5^2\text{S}_{\frac{1}{2}}(F=3) \rightarrow$ $^{85}\text{Rb } 5^2\text{P}_{\frac{3}{2}}(F'=4)$	0.9 ± 0.3	0.7 ± 0.02
$^{85}\text{Rb } 5^2\text{S}_{\frac{1}{2}}(F=2) \rightarrow$ $^{85}\text{Rb } 5^2\text{P}_{\frac{3}{2}}(F'=3)$	0.8 ± 0.03	0.7 ± 0.1
$^{87}\text{Rb } 5^2\text{S}_{\frac{1}{2}}(F=2) \rightarrow$ $^{87}\text{Rb } 5^2\text{P}_{\frac{3}{2}}(F'=3)$	180.2 ± 86.6	0.6 ± 0.02
$^{87}\text{Rb } 5^2\text{S}_{\frac{1}{2}}(F=1) \rightarrow$ $^{87}\text{Rb } 5^2\text{P}_{\frac{3}{2}}(F'=2)$	62.5 ± 4.1	0.6 ± 0.01

when the probe beam along the cavity axis is tuned to the cooling transition $\{5^2\text{S}_{\frac{1}{2}}(F=2) \rightarrow 5^2\text{P}_{\frac{3}{2}}(F'=3)\}$ of ^{87}Rb , which is also evident from the experimental data presented in Table 3.1. The large build up time for intra-cavity intensity is also a commonly observed phenomenon in lasers, where in the presence of the active medium and resonant light, the build up time for a steady state circulating intensity inside the cavity can be orders of magnitude longer than the decay time from the cavity. The transient behaviour in Fig. 3.4 can be understood within laser theory [25].

3.4.4 Optical bistability and hysteresis in negative logic switching

The cell cavity system is inherently a bistable system due to the presence of Rb atoms which show strong absorption in the presence of resonant light being coupled into the cavity mode. The bistability is a function of the cavity-laser detuning and the atomic frequency-laser detuning. On atomic resonance, the probe light transmitted through the cavity exhibits bistable behaviour [22]. This is observed when the cavity length is kept constant such that it supports

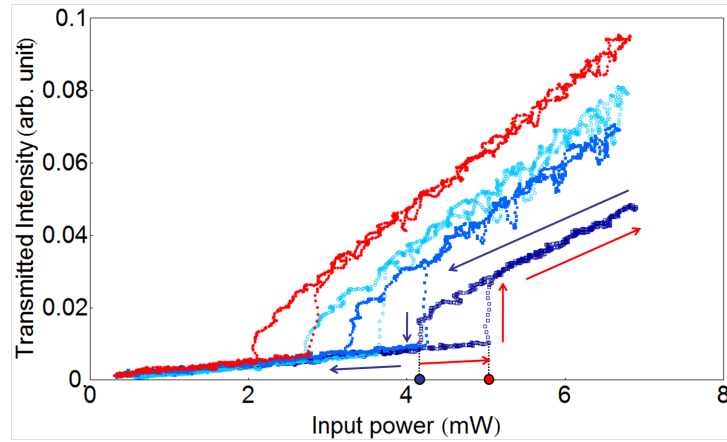


FIGURE 3.5: Typical hysteresis curves with and without the switching(control) beam at three different control beam powers of $600\mu\text{W}$, 10mW and 22mW . The red trace (filled circles) represents the hysteresis cycle without the switching beam. The light blue (open circles), dark blue (filled squares) and indigo traces (open squares) represent the hysteresis cycle with the control beam powers at $600\mu\text{W}$, 10mW and 22mW respectively. The red and blue dots on the input power (to cavity) axis represent the $I_{ThreshUp}$ and $I_{ThreshDown}$ intensity points. The red and blue arrows depict respectively the upward and downward cycle of the hysteresis curve. Notice the increasing shift in the hysteresis cycle towards increasing input intensity with increasing switching beam power.

transmission at atomic resonance frequency. The input probe intensity into the cavity is then ramped from low to high (up cycle) and back again from high to low (down cycle) using an AOM as shown in Fig. 3.2. The evolution of the cavity transmission intensity as a function of the incident probe intensity then exhibits bistable behaviour, as shown in Fig. 3.5. It can be seen that the threshold for transmission, on the ramp up starts at a higher input intensity, and falls to zero from a finite value on the ramp down, at a lower value of input intensity. The ramp rate in input intensity in the up and down cycle is the same.

To experimentally demonstrate this phenomenon, we kept the coupling laser frequency is tuned to the maximum of the absorption of the $5^2\text{S}_{1/2}(F=2) \rightarrow 5^2\text{P}_{3/2}(F')$ doppler broadened peak, while the switching laser beam tuned to the maximum of the absorption of the $5^2\text{S}_{1/2}(F=1) \rightarrow 5^2\text{P}_{3/2}(F')$ doppler broadened peak and its intensity I_c maintained constant. We verified the existence of hysteresis in the system both with and without the switching beam. In the

first case, we blocked the switching laser beam and tuned the cavity into resonance. Then we zoomed onto the peak of the transmission fringes of the cell cavity and maintained the voltage level manually at the peak without locking the cavity. When this condition was achieved, we vary the input intensity I_p to the cavity over a period of few seconds by varying the radio-frequency power of an acousto-optic modulator placed along the path of the coupling laser beam. We record the variation in the peak height of the transmission fringe for the entire cycle for which the coupling laser intensity I_p was varied on an oscilloscope. We repeat the same procedure in the presence of the switching laser beam, keeping the cavity maintained at the same voltage level as in the previous case and record the variation again on an oscilloscope. This is illustrated in Fig. 3.5.

On the upward cycle the cavity transmission is zero for input light intensity $I < I_{ThreshUp}$ where $I_{ThreshUp}$ is the minimal value of input intensity to the cavity for which we see measurable transmission. At $I_{ThreshUp}$ a small change in input intensity results in a sharp increase of intra-cavity light build-up and the cavity consequently transmits exhibiting the characteristics of threshold behavior. Increasing the cavity input intensity beyond this value causes a proportional change in cavity transmission. While ramping down the input intensity to the cavity from the value I_{max} which results in highest point of cavity transmission it is observed that the afore-mentioned proportional regime behavior extends well below $I_{ThreshUp}$ till a value $I_{ThreshDown}$ for which the transmitted intensity to the cavity sinks rapidly to zero. Thus the intra-cavity intensity build up exhibits hysteresis behavior in the range $I_{ThreshDown} < I < I_{ThreshUp}$.

In the presence of the control beam, as the intensity of the control beam increases, the entire hysteresis curve shifts to higher values of input intensities, see Fig. 3.5, with no qualitative change observed in the nature of the hysteresis curve. Thus the presence of control beam inhibits transmission of the probe beam through the cavity. It has been observed experimentally that the relative polarizations of the probe and control beam have no measurable effect on the

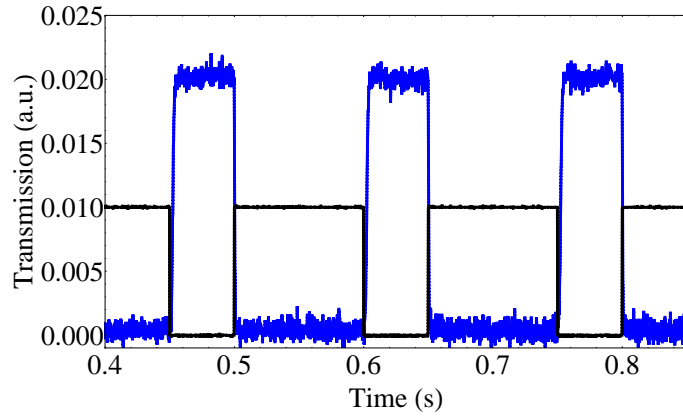


FIGURE 3.6: A time trace recording three cycles of switching. The transmission is high I_0 when $I_c = 0$ and low when $I_c > I_{cSwitch}$. Thus the switch operates in negative logic.

attenuation of intensity in the cavity mode. The cavity transmission has the same polarization state as the input light into the cavity. The consequences of this control beam induced attenuation of cavity transmission are explored below.

3.4.5 Characterization of all optical switching in negative logic

The most dramatic consequence of attenuation of the transmission is when the transmitted light is completely extinguished as shown in Fig. 3.6. Experimentally it is seen that for an appropriately chosen value of probe intensity I_p incident into the cavity mode for which the transmitted light intensity I_{pTrans} is measured, there can exist a control beam intensity $I_c > I_{cSwitch}$, for which $I_{pTrans}=0$, that is the transmitted light goes to zero. Here $I_{cSwitch}$ is the minimum value of control beam intensity I_c for which we start seeing visible change in I_{pTrans} . This is experimentally demonstrated by setting the probe laser on the $F=2 \leftrightarrow F'$ transition doppler broadened absorption maxima, and setting the cavity length to a constant value which supports the transmission of the probe

laser. With this setting the probe transmission intensity $I_{pTrans}(t) \approx I_0$ which is a constant intensity value with time. Neither the cavity nor the probe laser is locked, so there exist small drifts in the transmission as the laser frequency or the cavity length fluctuate. The control is then switched ON and OFF with the AOM (Fig. 3.2) with control beam intensity $I_c > I_{cSwitch}$. This results in the switching behaviour of the probe transmitted through the cavity, in negative logic with respect to the control beam. This intensity manipulation over three cycles is shown in Fig. 3.6.

In order to quantify the functioning of the switch further we define the efficiency e of the switch as $e = 1 - \frac{h_{on}}{h_{off}}$. Here h_{off} is the height of the cavity transmission peak when the switching beam is OFF and h_{on} is the transmission peak height when the switching beam is ON. The height are measured with respect to the non resonant baseline light level, which remains the same irrespective of the state of the switching laser. In absolute terms the baseline light level is ≈ 50 times lower than the peak heights. Thus the efficiency of the switch can assume values between 0 and 1. This is experimentally verified and is illustrated in Fig. 3.7. The efficiency measurement was done in the continuous mode of operation of the control beam. However the intensity for attenuation of the cavity transmission is the same.

For the present experiment, the polarizations vectors of the two intersecting beams within the cavity are perpendicular to each other. Fixing the intensity I_p of the probe laser, we can vary the intensity of the control laser I_c with the following effect. At $I_c \ll I_{cSwitch}$ there is no effect on the cavity transmission of the probe and so the efficiency of the switching is ≈ 0 . Beyond a certain threshold value of I_c denoted by $I_{cThresh}$, the transmitted peak height decreases. This decrease is not only a decrease in height but also a corresponding decrease in the integrated area under the peak, as the peak width remains unchanged with decreasing peak height. The efficiency of the switch increases in a highly non-linear fashion until it reaches $e \approx 0.8$ after which a saturation of the efficiency

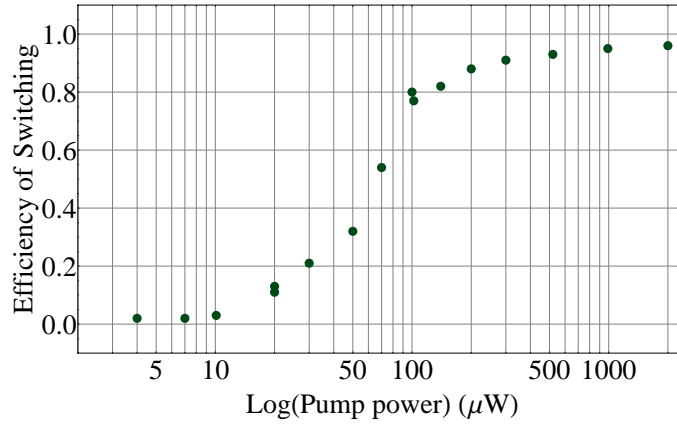


FIGURE 3.7: The gradual increase in the efficiency of the switching, as a function of I_c is illustrated here. The x-axis represents the power of the control laser and the y-axis the switching efficiency.

is reached gradually. This is illustrated in Fig. 3.7.

The experiments above have both probe and control laser frequencies set at their respective ^{87}Rb absorption maxima. It is of interest to know how cavity attenuation is affected as a function of frequency shifts from the resonance maxima. To investigate this I_p and I_c are adjusted so that when both are on their respective absorption peaks at ω_p and ω_c and I_c attenuates I_{pTrans} partially, that is the efficiency $e \approx 0.5$. At the probe frequency ω_p the cavity length is scanned, while the control laser beam frequency ω_c is scanned across the full doppler broadened resonance of the $F=1 \leftrightarrow F'$ manifold absorption peak for constant I_c . The resulting attenuation of I_{pTrans} as a function of the detuning of the control laser $\delta\omega_c = \omega_c - \omega_{c0}$ is shown in Fig. 3.8. It is clear the the efficiency of attenuation is highest when $\omega_c = \omega_{c0}$, i.e at the absorption maximum of the control beam, and falls to $e \approx 0$ at $\delta\omega_c \approx \Gamma$, where Γ is the FWHM of the control laser absorption profile. This clearly demonstrates the atomic resonance mediated attenuation of the cavity mode transmission.

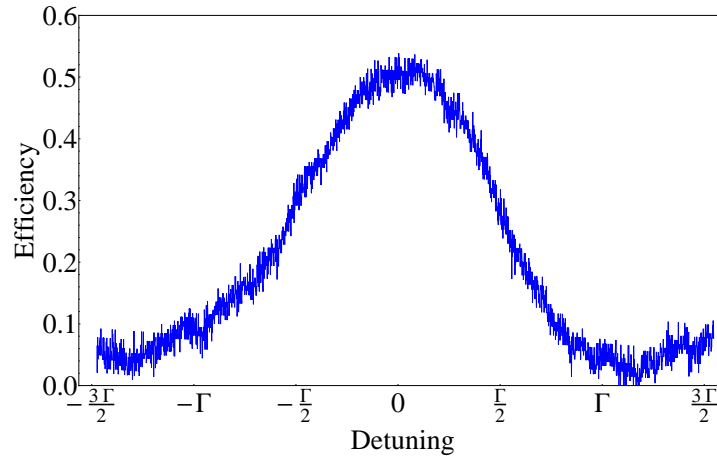


FIGURE 3.8: The change in the efficiency of attenuation as a function of the control laser frequency detuning across the absorption profile of the control laser. At zero detuning with respect to the absorption maximum for the control beam, the switching efficiency is highest and there is a steady decline as a function of detuning from the absorption maximum.

3.4.6 Partial switching regime in negative logic

The attenuation of the transmitted light has the peculiar feature that the addition of more light into the cavity mode results in the complete suppression of the mode. The redistribution of the light intensity must show up in other parts of the experiment as shown in Fig. 3.9. To diagnose this redistribution qualitatively, the light intensity is monitored in two additional directions PD_C and PD_R as seen in Fig. 3.2, which measure the control beam intensity in transmission and the reflection of the probe beam from the cavity. The probe and control beam frequencies are set to their respective absorption maxima at ω_p and ω_c respectively. Now I_c is adjusted such that $e \approx 0.5$, i.e. the experiment is in the partial attenuation regime. In this configuration, with $I_c = 0$, as the cavity length is scanned, cavity transmission peaks are measured in PD_T and in the reflected light collection diode PD_R , a corresponding absence of light is measured, when the cavity resonance conditions are met by the probe beam. When I_c is adjusted for partial transmission of probe light on cavity resonance,

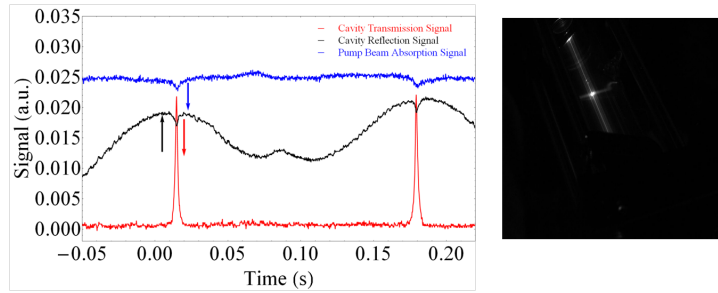


FIGURE 3.9: Left: A sweep across the cavity resonance recording the change in the transmitted and reflected probe light and the transmitted control light, when partial attenuation of probe transmission is arranged. The red and black traces are cavity transmission (PD_T) and reflection (PD_R) signals respectively. The blue trace is the transmitted intensity (PD_C) of the control beam, which intersects the cavity mode. As the cavity transmission resonance is scanned across, the signal in PD_T goes down, PD_R goes up and in PD_C goes down. The sense of light level change is indicated by the arrows alongside the respective peaks. Right: A CCD image of the overlap zone of the two beams along the cell cavity axis.

the intensity in transmission (PD_T) decreases, the reflected probe light on resonance (PD_R) increases and the control beam intensity in transmission (PD_C) decreases. The measured intensities and the direction of their change in the three photodiodes is shown in Fig. 3.9. It is clearly seen that the presence of the control beam expels the probe light from the cavity, making the cavity optically non-resonant with the frequency of input probe light. The light energy budget is that probe decreases in transmission but increases in reflection. The control decreases in intensity in transmission. There is significantly enhanced fluorescence from the volume of intersection of the probe light in the cavity mode and the control light beam.

The complete extinction of the cavity transmission, that is the limit $e \rightarrow 1$, is the requirement for total switching of I_{pTrans} as illustrated in Fig. 3.6, for probe and control frequencies set at ω_{p0} and ω_{c0} respectively. Determination of the rise and fall time of the switching in Fig. 3.6, particularly in light of the asymmetric on resonant switching with only the cavity beam in Fig. 3.4(b) and (d) is essential. For the intensities of the probe and control beam described earlier, the result of zooming in on the rise and fall of $I_p(t)$ is shown in Fig. 3.10.

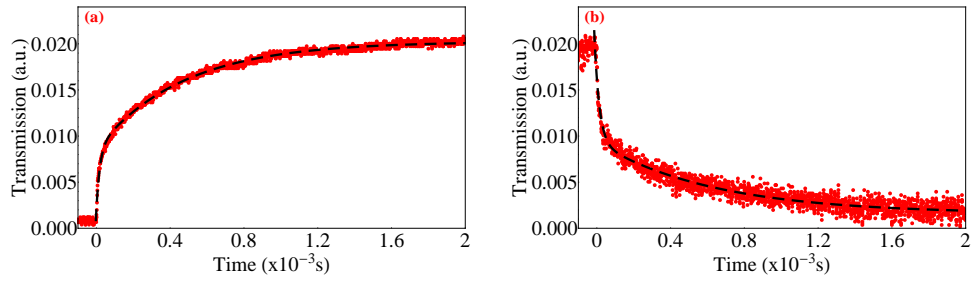


FIGURE 3.10: Time traces recording rise and fall times of switching in negative logic mode of operation. Figure 10(a) represents the rising edge while Figure 10(b) represents the falling edge. The dashed line is a double exponential fit to the data in each of the cases. The rise time is 1ms and the fall time is 1ms for 10% to 90% switching.

Here $I_p(t)$ denotes the time dependent cavity transmission corresponding to the time varying control beam intensity $I_c(t)$. We find that the rise and fall times are best fit by a double exponential which results in fast and slow time constants. The fast time constants are $\approx 50\mu s$ and the slow time constants are $\approx 500\mu s$. This is generally true of both the rising and falling edges of I_{pTrans} . By contrast the switching time of the AOM controlled I_c is less than 100ns. It is interesting to note that the large difference in transmission build up and decay times with the probe on resonance and the control OFF is not reproduced in the case of all optical switching in Fig. 3.10.

Table 3.2: Rise and fall time constants with control beam in negative logic

Case	Fast (μs)	Slow (μs)
Rise Time Constant	45.8 ± 24.5	497.4 ± 138.9
Fall Time Constant	23.1 ± 10.3	569.7 ± 221.4

Hard switching is implemented in the following manner. Both ω_p and ω_c are adjusted to be at their respective absorption maximum. With I_c blocked, the cavity length is tuned so that the transmission through the cavity is always high. In this situation I_c is then periodically pulsed using an acousto-optic modulator(AOM), which has switching times of 100ns to activate the switching of

the cavity transmission. The transmitted intensity is reproduced in Fig. 3.6. The switching action demonstrates high fidelity and exhibits a rise time of 1ms and a fall time of 1ms as shown in Fig. 3.10.

The rise and fall of cavity transmission recorded by pulsing the control beam, applied transverse to the cavity axis, using the acousto-optic modulator(AOM) have been documented in Table 3.2. The transient dynamics of the rising and falling edge have been fitted to double exponential profiles. It is seen that there are two independent time scales associated with the transient dynamics in negative logic switching. One of them is a fast time constant while the other is a long time constant.

The fast response in our experiments is attributed to the small signal gain of the cavity mode field in reaction to the switching ON or OFF of the control light. Small signal gain coefficient (γ_ω) plays a crucial role in the physics of optical amplifiers and represents the gain per unit length in the photon flux. In our experiment, the fraction of the cavity mode that is illuminated by the control laser, z_δ , is much smaller than the mode length, enabling us to associate the change in cavity transmission with the small signal gain in this region, which depends on the difference in the populations in the excited and ground states i.e. $\gamma_\omega \propto N_{e_a} - N_{g_a}$. As no population inversion is possible in our system, $N_{e_a} < N_{g_a}$, implying that γ_ω is always negative and propagation along the cavity mode is attenuated. The AOM switches the control light intensity linearly with time, which in turn increases or decreases the value of $N_{g_a}(t) \propto I_c(t)$, implying $\gamma_\omega(t) \propto t$ in the time immediately following the switching of the state of I_c . As the gain per unit length within the cavity mode is proportional to an $I_p(0)\exp(\gamma_\omega(t)z_\delta)$, the fast response behavior of the transmitted probe light through the cavity is exponential. The transmitted intensity is anti-correlated with the switching light rate of change since $N_{e_a} < N_{g_a}$ at all times. Therefore, when the control light is switched off, the light in the cavity mode increases and vice versa.

The slow time scales associated with the rise time and fall time may be explained in terms of the rate of transfer of atomic population from one ground state to another as discussed in section 3.6.

3.5 Experimental arrangement and setup for positive logic switching

For the positive logic switching, we employ the same transition for probe and control pulses. For the experiments on the ^{87}Rb cell cavity, we choose the cooling transition ($F = 2 \rightarrow F' = 3$, ^{87}Rb D_2 line). The relevant energy level diagram along with the experimental schematic is shown below in Fig. 3.11.

We set the input probe intensity to a value close to the threshold of transmission of light into the cavity. At this values of input probe intensity, the medium inside the cavity is not saturated to allow the transmission through the cavity. Viewing the path of the light build up along the cavity axis shows weak fluorescence build up due to absorption of resonant light by the ^{87}Rb atoms inside the vapor cell. However, no significant transmission through the cavity occurs at this point. Once this condition is satisfied, we allow a control beam resonant on the same cooling transition ($F = 2 \rightarrow F' = 3$, ^{87}Rb D_2 line) to intersect the cavity mode by orienting it transverse to the cell cavity axis as shown in Fig. 3.11. As soon as the control beam is put on, we see transmission of light through the cell cavity. This choice of the cooling atomic transition of ^{87}Rb for positive logic switching mode is purely arbitrary. One can also choose the repumper transition for the positive logic mode of operation. However this does not change the qualitative characteristics of the optical switch when operated following the positive logic protocol. This transmission can be understood by invoking a simple model which tries to argue the switching mechanism from the point of redistribution of the relative populations of the two ground states of

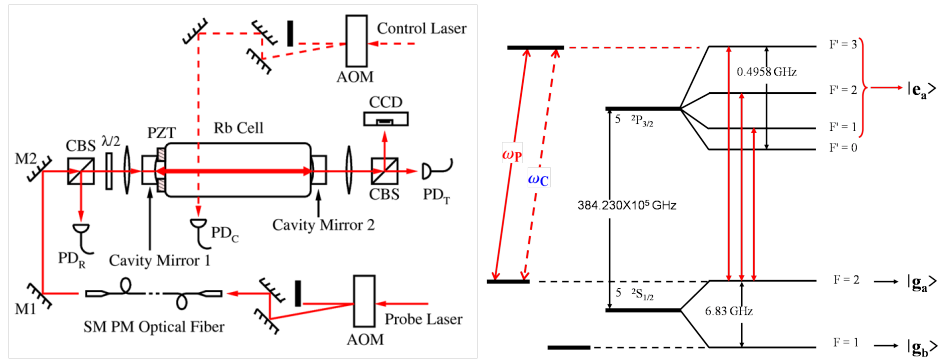


FIGURE 3.11: The experimental schematic and the relevant energy level diagram for positive logic switching.

the ^{87}Rb D_2 atomic transition.

3.5.1 Optical bistability and hysteresis in positive logic switching

As reported earlier in the negative logic scenario, we investigate the change in the hysteresis curves in the positive logic case and try to compare and contrast it against the behavior seen in negative logic switching case. We demonstrate this phenomenon by keeping both the coupling/probe and the switching/control laser frequencies tuned to the maximum of the absorption of the $5^2S_{1/2}(F = 2) \rightarrow 5^2P_{3/2}(F')$ doppler broadened peak. The coupling laser intensity I_c is varied above and below the saturation threshold of the ^{87}Rb atomic medium inside the cell cavity by varying the radio-frequency power of an acousto-optic modulator placed along the path of the coupling laser beam.

Initially we adjust the power of the coupling beam so that we see very little transmission through the cell cavity. We then sit on the resonance of the cavity transmission by manually adjusting the cavity piezo offset voltage. We then modulate the coupling beam intensity I_c along the cavity axis over a period of few seconds by varying the radio-frequency power of an acousto-optic

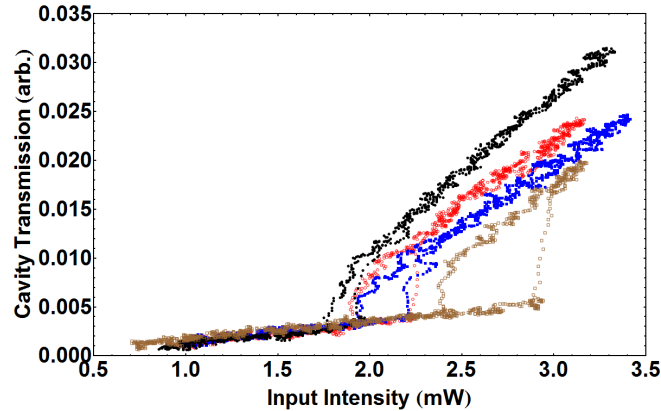


FIGURE 3.12: Typical hysteresis curves with and without the switching(control) beam at three different pump powers of 5.5mW, 10.5mW and 23mW. The brown trace (open squares) represents the hysteresis cycle without the pump beam. The blue (filled squares), red (open circles) and black (filled circles) represent the hysteresis cycle with the switching(control) beam powers at 5.5mW, 10.5mW and 23mW respectively. Notice the increasing shift in the hysteresis cycle towards decreasing input intensity to cavity with increasing switching beam power. Another interesting feature of the hysteresis curves is the decrease in area under the cycle with increasing switching beam power.

modulator placed along the path of the coupling laser beam. We record on an oscilloscope the variation in the peak height of the transmission fringe for the entire cycle for which the coupling laser intensity I_c was varied both in the presence and in the absence of the switching laser beam which is on the same transition as the coupling laser beam. This is illustrated in Fig. 3.12.

3.5.2 Transient dynamics in positive logic switching

We experimentally investigated the dynamics of positive logic switching in the transient regime and found that there exists two timescales associated with the switching phenomenon as shown in Fig. 3.13. In order to measure the timescales associated with the transient dynamics we followed a protocol similar to the one as reported earlier in negative logic switching. We initially tuned the cavity into resonance with the input probe beam and adjusted the offset

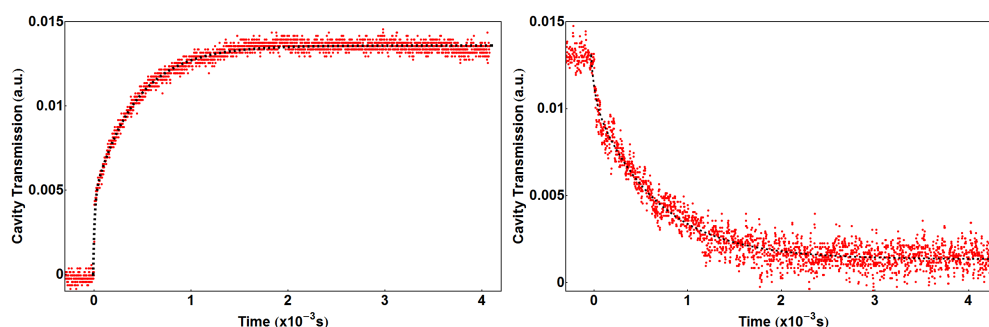


FIGURE 3.13: Left: A time trace depicting the rising edge of the cavity transmission when the optical switch is operated in positive logic mode. Right: A time trace depicting the falling edge of the cavity transmission when the optical switch is operated in the same mode as mentioned earlier. The dashed line is a double exponential fit to the data. The rise time and the fall time is again 1ms for 10% to 90% switching and consistent with the time scales for the same amount of switching as reported in the case of negative logic switching phenomenon described earlier in the chapter.

voltage on the cavity piezo so that we could be at the peak of cavity transmission. The cavity resonance could be maintained on its maximum for a couple of seconds before it would drift away. However this would provide us with enough time to record the switching phenomenon seen. In this interim period with the cavity transmission at its maximum, we would enable high speed switching of the control beam via an acousto-optic modulator (AOM) applied transverse to the cell cavity axis. We observed that the rise and fall time of the cavity transmission obtained by periodic modulation of the control beam intensity shows an effective time constant of about a millisecond for 10% - 90% switching. However closer monitoring revealed that this effective single time constant is in fact a convolution of a small (fast) and a long (slow) time constant. The mean fast time constant of the order of 24 microseconds while the mean longer time constant is of the order of 600 microseconds as documented in Table 3.3. Thus the observed time scales in positive logic switching are the same order of magnitude as recorded for negative logic switching.

Table 3.3: Rise and fall time constants with control beam in positive logic

Case	Fast (μs)	Slow (μs)
Rise Time Constant	26.8 ± 11.9	504.8 ± 123.3
Fall Time Constant	24.0 ± 11	676.7 ± 128

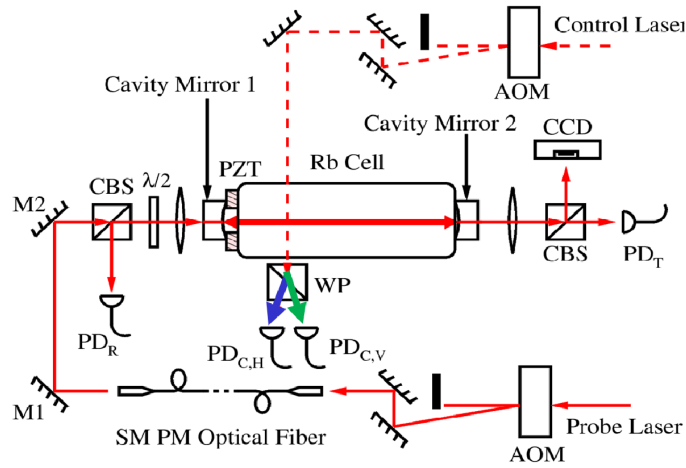


FIGURE 3.14: The experimental schematic for positive logic switching in the partial switching regime to investigate small signal gain in the system. The blue arrow and green arrows after the Wollaston prism (WP) indicate the linearly polarized horizontal and vertical components of the scattered light from the switching beam.

3.5.3 Investigation of small signal gain in positive logic switching

We also investigated the possibility of small signal gain or the existence of stimulated emission in the context of positive logic switching as shown in illustrated in Fig. 3.14. We adjust the input probe and control beam powers on the cell cavity experiment so that we see a relatively small transmission through the cell. Care is taken to adjust the input probe beam intensity along the cell cavity axis such that the atomic medium along the axis is very close to saturation, while at the same time ensuring that a very small but net transmission occurs through the end of the cavity. In this condition we have adjusted the polarization of the switching beam by using a half-wave ($\frac{\lambda}{2}$) plate and a polarization

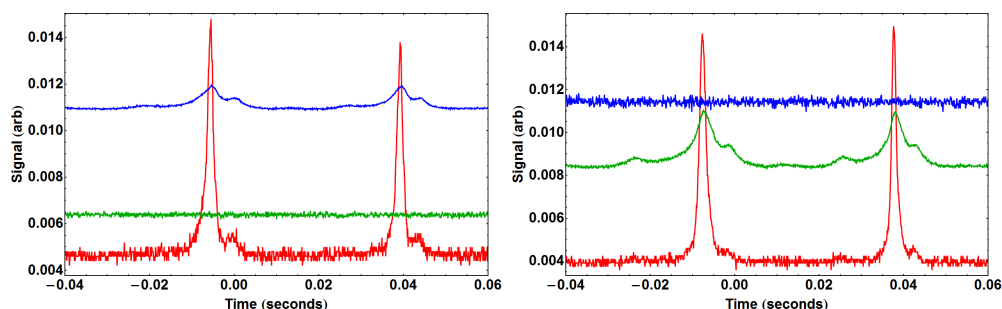


FIGURE 3.15: Record of polarization effects on the switching beam after passing through the Wollaston prism (WP). Left: The signal picked up on the photo-diode placed after the WP with the control beam having purely horizontal polarization. Right: Same case with the control beam polarization set to vertical. In both figures the green and the blue trace depict signals with linearly vertical and horizontal components of light. The red trace denotes cavity transmission in both cases.

beam splitting cube (PBSC) combination. In one set of experiments we have maximized the transmitted beam through the PBSC ensuring linear horizontal polarization while in a second set we have maximized the output beam on the reflected port of the PBSC ensuring vertical linear polarization. In a third set of measurements we have set it at an intermediate linear polarization where both horizontal and vertical components of the linear polarization prevail.

We now place a Wollaston prism (WP) on the path of the switching beam which exits the cell to select the polarization of the beam scattered along that direction. The WP acts as polarization filter to an extinction ratio of 1000:1. It also spatially separates the horizontal and vertical linear polarization components of the scattered which are then detected on the two photo-diodes placed at appropriate positions. For the three sets of linear polarization settings described above we record very high contrast polarization dependent signals on the photo-diodes. As can be seen from the figure Fig. 3.15, there is absolutely no pick up on the complimentary photo-diode when the polarization setting is either purely linearly horizontal or linearly vertical. The striking feature of both the signals recorded for the two settings of linear polarization shows a remarkable increase in signal which coincides exactly at the points where the cavity

transmits. Thus there is enhanced scattering of light by the atoms in the cavity mode in the direction of the switching beam. This phenomenon of increase of signal along the direction of the switching beam maintaining the state of polarization of the scattered to a high degree even by atoms at room temperature leads us to believe that the cell cavity system is capable of sustaining gain in the small signal operating regime.

3.6 Qualitative model for estimating time

constants of switching in negative and positive logic

The negative logic switch is operated with the probe beam tuned to the ^{87}Rb cooling transition ($F=2 \rightarrow F'=3$, D_2 line) and the switching beam tuned to the ^{87}Rb repump transition ($F=1 \rightarrow F'=2$, D_2 line). In contrast the positive logic switching is realized when both the probe and switching beams are tuned to the ^{87}Rb cooling transition ($F=2 \rightarrow F'=3$, D_2 line). Qualitatively the switching effect appears to be polarization independent, which might indicate lack of role of Zeeman coherences in the switching effect. Here we propose a simplified four level model based only on hyperfine levels involved. We take the density matrix approach and solve for the time dependent equations for the population terms. We model the experimentally observed switching mechanism based on the rate of transfer of population from one ground state to the other ground state by addition of the switching field from the transverse direction. The entire model is based on the primary assumption that only atoms in the overlap zone of the probe and switching beams are participating in the optical switching phenomena observed.

The total Hamiltonian for the system consisting of the atom and the probe

3.6 QUALITATIVE MODEL FOR ESTIMATING TIME CONSTANTS OF SWITCHING IN NEGATIVE AND POSITIVE LOGIC

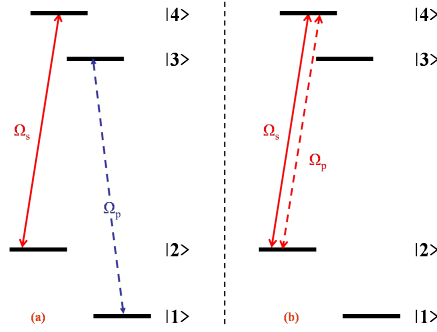


FIGURE 3.16: A simplified schematic of a four level atomic system to model the switching phenomena. Left: Relevant energy level diagram for negative logic switching. The cavity coupling (probe) field is labeled as Ω_s connecting states $|2\rangle$ and $|4\rangle$ while the switching field is labeled as Ω_p connecting states $|1\rangle$ and $|3\rangle$. Right: Relevant energy level diagram for positive logic switching. Both the cavity coupling (probe) field (labeled as Ω_s) and the switching field (labeled as Ω_p) connect the states $|2\rangle$ and $|4\rangle$.

and switching light fields in the interaction picture is expressed as

$$H = H_0 + H_I \quad (3.4)$$

where H_0 is the Hamiltonian for the bare atom and H_I the light-atom interaction Hamiltonian. These are given by

$$H_0 = \hbar\omega_1|1\rangle\langle 1| + \hbar\omega_2|2\rangle\langle 2| + \hbar\omega_3|3\rangle\langle 3| + \hbar\omega_4|4\rangle\langle 4| \quad (3.5)$$

and

$$H_I = -\frac{\hbar}{2}[\Omega_{24}|2\rangle\langle 4|exp(-i\omega_{24}t) + \Omega_{23}|2\rangle\langle 3|exp(-i\omega_{24}t) + \Omega_{13}|1\rangle\langle 3|exp(-i\omega_{13}t) + H.C.] \quad (3.6)$$

Here the $\hbar\omega_i$ represent the energies of the levels as represented in Fig. 3.16, with ω_s and ω_p the frequencies of the probe and switching laser beams and Ω_{ij} denoting the Rabi frequency connecting the ground level $|i\rangle$ to the excited level $|j\rangle$. The term ‘‘H.C.’’ refers to hermitian conjugate.

The dynamics of the system described by the above Hamiltonian can be studied using the density matrix $\rho = \sum \rho_{ij} |i\rangle \langle j|$. The time evolution of the density matrix ρ is given by the Liouville equation

$$\dot{\rho} = \frac{i}{\hbar} [\rho, H] + \mathcal{L}_{dissipation} \quad (3.7)$$

where the first term on the right hand side of equation (3.7) describes the coherent evolution of the density matrix operator ρ under the Hamiltonian H while the second term on the right hand side of equation (3.7) describes the operator $\mathcal{L}_{dissipation}$ of the Lindblad form and contains all possible modes of dissipation or relaxation existing in the system. The damping/dissipation operator is defined as

$$\mathcal{L}_{dissipation} = \sum \left[\frac{\Gamma_{ij}}{2} (2\sigma_{ij}\rho\sigma_{ij}^\dagger - \sigma_{ij}^\dagger\sigma_{ij}\rho - \rho\sigma_{ij}^\dagger\sigma_{ij}) \right] \quad (3.8)$$

Here ρ is the density matrix defined in the usual notation above while the σ_{ij} defines the creation operator for atomic excitation while σ_{ij}^\dagger denotes the annihilation operator for atomic excitation. Γ_{ij} is the decay rate connecting states $|i\rangle$ and $|j\rangle$.

σ_{ij} is defined by $g_j \cdot e_i^\dagger$ where g_j and e_i are according to the definitions given in equations (3.9) and (3.10).

The two ground states $|2\rangle$ and $|1\rangle$ are defined as

$$|2\rangle = \begin{pmatrix} 0 \\ 1 \\ 0 \\ 0 \end{pmatrix}, \quad |1\rangle = \begin{pmatrix} 1 \\ 0 \\ 0 \\ 0 \end{pmatrix} \quad (3.9)$$

while the two excited states $|3\rangle$ and $|4\rangle$ are given by

$$|3\rangle = \begin{pmatrix} 0 \\ 0 \\ 1 \\ 0 \end{pmatrix}, \quad |4\rangle = \begin{pmatrix} 0 \\ 0 \\ 0 \\ 1 \end{pmatrix} \quad (3.10)$$

The other assumptions which go into developing and solving the density matrix based rate equation model are outlined as following:

a. The F=2 ground state, including its five Zeeman sublevels, is modeled as a single state, $|g_a\rangle$, and the F=1 ground state is modeled as another state, $|g_b\rangle$. For simplicity of nomenclature in the density matrix approach we label these as $|2\rangle$ and $|1\rangle$ respectively as shown in Fig. 3.16.

b. The two excited state manifolds are modeled each as a single state, $|e_a\rangle$ and $|e_b\rangle$, respectively. This justification is valid since none of the pump or probe beams involved in the experiment are frequency locked to any given hyperfine transitions of the Rb D₂ spectrum. Keeping with the density matrix nomenclature norm above we label these two states as $|4\rangle$ and $|3\rangle$ respectively.

c. We are assuming that any polarization-dependent effects are not significant in the switching mechanism.

d. We are accounting only for spontaneous emission processes in this model and do not take into account the role of stimulated absorption.

e. We neglect the role of stimulated emission processes which will be valid under two conditions: (1) the light intensities remain low enough for spontaneous emission rate to be much faster than stimulated emission rate; (2) the excited state populations remain low enough so that stimulated emission cannot add significantly to the intensities of probe and switching beams.

f. Although we do see a slight change in the transmitted intensity of the switching beam, in the thin medium approximation (valid at room temperature, over cell diameter of 2.54 cm), we hold it constant at the incident intensity of

the switching beam.

g. We also assume that the atoms outside the beams are largely unpolarized (valid for uncoated vacuum cell, where atoms exiting the beam will hit the wall and depolarize before returning to the beam), so they are thermally distributed equally over all eight Zeeman sublevels.

h. We further ignore any possibility of collisional decay of excited state atoms in the model.

i. For simplicity, we have ignored transit time broadening for the atoms when they are in the overlap region of the probe and switching fields.

Under the above assumptions, we can write down the following rate equations for atomic densities which account for relaxations and repopulations due to optical transitions (absorption and emissions) of the atoms through the beam. The final set of equations for the populations after applying the rotating wave approximation (RWA) is given below:

$$\dot{\rho}_{11} = \Gamma_{21}\rho_{22} + \Gamma_{31}\rho_{33} + \Gamma_{41}\rho_{44} + \frac{i}{2}(\rho_{31}\Omega_p^* - \rho_{13}\Omega_p) \quad (3.11a)$$

$$\dot{\rho}_{22} = \Gamma_{42}\rho_{44} + \Gamma_{32}\rho_{33} - \Gamma_{21}\rho_{22} + \frac{i}{2}(\rho_{32}\Omega_{offres}^* - \rho_{23}\Omega_{offres} + \rho_{42}\Omega_s^* - \rho_{24}\Omega_s) \quad (3.11b)$$

$$\dot{\rho}_{33} = \Gamma_{43}\rho_{44} - \Gamma_{32}\rho_{33} - \Gamma_{31}\rho_{33} + \frac{i}{2}(\rho_{23}\Omega_{offres} - \rho_{32}\Omega_{offres}^* + \rho_{13}\Omega_p - \rho_{31}\Omega_p^*) \quad (3.11c)$$

$$\dot{\rho}_{44} = -(\Gamma_{43} + \Gamma_{42} + \Gamma_{41})\rho_{44} + \frac{i}{2}(\rho_{24}\Omega_s - \rho_{42}\Omega_s^*) \quad (3.11d)$$

while the equations for coherences after applying the RWA are given by

3.6 QUALITATIVE MODEL FOR ESTIMATING TIME CONSTANTS OF SWITCHING IN NEGATIVE AND POSITIVE LOGIC

$$\dot{\rho}_{21} = -\tilde{\gamma}_{21}\rho_{21} - \frac{i}{2}\rho_{23}\Omega_p + \frac{i}{2}\rho_{31}\Omega_{offres}^* + \frac{i}{2}\rho_{41}\Omega_s^* \quad (3.12a)$$

$$\dot{\rho}_{31} = -\tilde{\gamma}_{31}\rho_{31} + \frac{i}{2}\rho_{21}\Omega_{offres} + \frac{i}{2}(\rho_{11} - \rho_{33})\Omega_p \quad (3.12b)$$

$$\dot{\rho}_{41} = -\tilde{\gamma}_{41}\rho_{41} - \frac{i}{2}\rho_{43}\Omega_p + \frac{i}{2}\rho_{21}\Omega_s \quad (3.12c)$$

$$\dot{\rho}_{32} = -\tilde{\gamma}_{32}\rho_{32} + \frac{i}{2}(\rho_{22} - \rho_{33})\Omega_{offres} + \frac{i}{2}\rho_{12}\Omega_p - \frac{i}{2}\rho_{34}\Omega_s \quad (3.12d)$$

$$\dot{\rho}_{42} = -\tilde{\gamma}_{42}\rho_{42} - \frac{i}{2}\rho_{43}\Omega_{offres} + \frac{i}{2}(\rho_{22} - \rho_{44})\Omega_s \quad (3.12e)$$

$$\dot{\rho}_{43} = -\tilde{\gamma}_{43}\rho_{43} + \frac{i}{2}\rho_{23}\Omega_s - \frac{i}{2}\rho_{42}\Omega_{offres}^* - \frac{i}{2}\rho_{41}\Omega_p^* \quad (3.12f)$$

where according to the above configuration of states Ω_s , Ω_{offres} and Ω_p are the Rabi frequencies of the coupling(probe), off-resonant pumping and the switching(control) fields respectively. The probe laser (field) Ω_s is the one coupled to the cavity mode while the switching laser (field) Ω_p is applied on the direction transverse to the axis of the cell cavity system. In the present situation Ω_{offres} is the field to account for the off resonant pumping of the atoms by the probe field Ω_s along the cavity axis. However in principle one can take it to be an externally applied additional field without any loss of generality. The Rabi frequencies for the model above are given by

$$\Omega_s = \mu_{24} \frac{E_s}{\hbar} = \Gamma_4 \sqrt{\frac{I_s}{2I_{sat}}} \quad (3.13a)$$

$$\Omega_{offres} = 10^{-4}\Omega_s \quad (3.13b)$$

$$\Omega_p = \mu_{13} \frac{E_p}{\hbar} = \Gamma_3 \sqrt{\frac{I_p}{2I_{sat}}} \quad (3.13c)$$

where the prefactor of 10^{-4} is the probability that an atom will absorb a photon from the probe (coupling) field and get optically pumped to state $|3\rangle$. The above factor of 10^{-4} has been estimated from the fact that in the case of laser cooling using a closed cycle transition, one out of every 10,000 atoms absorbs

a photon from the cooling laser field due to off resonant pumping and ends up in an excited state which is not closed. Here I_s and I_p are the intensities of the coupling(probe) and switching(control) laser fields respectively. I_{sat} is the saturation intensity for the ^{87}Rb D_2 transition. Further Γ_4 and Γ_3 denote the lifetimes of the excited states $|4\rangle$ and $|3\rangle$ respectively. The decay from $|4\rangle$ to $|1\rangle$ is possible via an electric quadrupole transition which is estimated to be a factor (a_0/λ) lower than the dipole transition from $|4\rangle$ to $|2\rangle$ [38]. Here a_0 is the Bohr radius in angstroms and λ is the wavelength of the light coupling states $|4\rangle$ and $|2\rangle$. We further define the following detunings:

$$\tilde{\gamma}_{21} = \gamma_{21} - i(\Delta_p - \Delta_{offres}) \quad (3.14a)$$

$$\tilde{\gamma}_{31} = \gamma_{31} - i\Delta_p \quad (3.14b)$$

$$\tilde{\gamma}_{41} = \gamma_{41} - i(\Delta_p - \Delta_{offres} + \Delta_s) \quad (3.14c)$$

$$\tilde{\gamma}_{32} = \gamma_{32} - i\Delta_{offres} \quad (3.14d)$$

$$\tilde{\gamma}_{42} = \gamma_{42} - i\Delta_s \quad (3.14e)$$

$$\tilde{\gamma}_{43} = \gamma_{43} - i(\Delta_s - \Delta_{offres}) \quad (3.14f)$$

where $\Delta_p = \omega_p - \omega_{13} - \mathbf{k}_p \cdot \mathbf{v}$, $\Delta_{offres} = \omega_{offres} - \omega_{23}$ and $\Delta_s = \omega_s - \omega_{24} - \mathbf{k}_s \cdot \mathbf{v}$ are the detunings of the switching, the off resonant and the probe (cavity input) fields respectively with respect to the appropriate atomic transitions connected through these fields. Here \mathbf{k}_p and \mathbf{k}_s are the wave-vectors of the switching and coupling fields respectively while \mathbf{v} is the velocity of the atom in the vapor cell consistent with the Maxwell-Boltzmann distribution of speeds at room temperature.

We define Γ_{nm} as the natural decay rate between any two levels $|n\rangle$ and $|m\rangle$. Also we define γ_{nm} as

$$\gamma_{nm} = \frac{1}{2}(\Gamma_n + \Gamma_m) \quad (3.15)$$

3.6 QUALITATIVE MODEL FOR ESTIMATING TIME CONSTANTS OF SWITCHING IN NEGATIVE AND POSITIVE LOGIC

where Γ_n and Γ_m are the individual decay rates of the states $|n\rangle$ and $|m\rangle$ respectively.

We solve the dynamical equations of motion for four different cases. The initial conditions at time $t=0$ for solving the equations (3.12) for all the cases are as follows:

$$\rho_{11} = 0.5 \quad (3.16a)$$

$$\rho_{22} = 0.5 - \frac{\left(\frac{I_s}{2I_{sat}}\right)}{1 + 4\left(\frac{\Delta_s}{\Gamma_4}\right)^2 + \left(\frac{I_s}{I_{sat}}\right)} \quad (3.16b)$$

$$\rho_{33} = 0.0 \quad (3.16c)$$

$$\rho_{44} = \frac{\left(\frac{I_s}{2I_{sat}}\right)}{1 + 4\left(\frac{\Delta_s}{\Gamma_4}\right)^2 + \left(\frac{I_s}{I_{sat}}\right)} \quad (3.16d)$$

The four different cases are as follows:

a. When the coupling and the switching fields are on complimentary transitions (in our case the ^{87}Rb cooling and repumper transitions respectively), we estimate the time taken to transfer the population from the cooling ground state to the repumper ground state when the repumper field is switched OFF at time $t=0$. This situation is akin to negative logic switching with no switching field. Here we get transfer times for the population of the order of a milli-second after solving the set of equations (3.12) for the initial conditions as given by (3.16).

b. When the coupling and the switching fields are on complimentary transitions (in our case the ^{87}Rb cooling and repumper transitions respectively), we estimate the time taken to transfer the population from the cooling ground state to the repumper ground state when the repumper field is switched ON at time $t=0$. This situation is similar to negative logic switching in the presence of the switching field. Here we get population transfer times of the order of ten microseconds after solving the set of equations (3.12) for the initial conditions as given by (3.16).

c. When the coupling and the switching fields are on the same transitions (in

our case the ^{87}Rb cooling transition), we estimate the time taken to transfer the population from the cooling ground state to the repumper ground state when the switching field is turned ON at time $t=0$. This situation is similar to positive logic switching in the presence of the switching field.

d. When the coupling and the switching fields are on the same transitions (in our case the ^{87}Rb cooling transition), we estimate the time taken to transfer the population from the cooling ground state to the repumper ground state when the switching field is turned OFF at time $t=0$. This situation is similar to positive logic switching in the absence of the switching field.

In both cases (c) and (d) above for the positive logic switching regime we get transfer times for the population of the order of a milli-second after solving the set of equations (3.12) for the initial conditions as given by (3.16).

Solving the dynamical equations of motion for the population terms using a numerical algorithm such as the NDSolve function in MATHEMATICA[®], we find that the rate of evolution of the population terms can be well described by a single exponential decay. This is in contrast to the experimentally measured time constants of negative and positive logic switching where we find that the cavity transmission decays with two time constants, one fast and one slow.

We find that the transfer rates for the above three cases (a), (c) and (d) are well described by a single time constant. We note that for the given conditions of the experimental situation for the negative and positive logic switching scenarios, we get long time constants of about a millisecond as the time taken to transfer the population from one ground state to another in cases (a), (c) and (d) respectively. The model however fails to account for the long time constant in situation (b) giving a single time constant of the order of 10 micro-seconds.

3.7 Conclusion

In the present study a deliberate choice of the Rb D_2 transition frequencies has been made, in order to extend the present work to studies with cold atoms. In our experiment the frequency of the light coupled into the cavity mode is set to $5^2S_{1/2} F=2 \rightarrow 5^2P_{3/2} F'=3$ of the D_2 transition of ^{87}Rb while the frequency of the control light to $5^2S_{1/2} F=2 \rightarrow 5^2P_{3/2} F'=2$ for the same D_2 transition as mentioned earlier, which are in fact the cooling transition and the repumping transition for a standard magneto-optical trap (MOT) of ^{87}Rb atoms. If a cavity is built around such a MOT, the possibility for many investigations open up along and beyond the lines probed above. While several differences exist between the vapor cell experiment discussed here and a cold atom experiment, there are many similarities which make the present work important in the context of future experiments with cold atoms.

To summarize, we have demonstrated an all optical switching phenomena in transmission utilizing a Rubidium vapor cell enclosed within a Fabry-Perot cavity. The cavity probe light can be completely extinguished by the control intensity, a fact which is used to demonstrate high fidelity switching of transmitted light through this system. The control light exhibits a threshold power, above which it alters the transmission properties of the cavity. Both steady state and transient processes are experimentally characterized for this system for two different approaches of realizing the optical switch. The physics of this system is discussed within the context of a driven four level system and both qualitative explanations and quantitative estimates for the observed steady state and transient phenomena are provided. The key features of this switch are as follows:

- a. The switch operates at close to half the telecom wavelength (1550nm).
- b. The switching mechanism is robust and alignment insensitive.
- c. The power of control light required to affect the transmitted intensity of the resonant seed light through the cavity is shown to be very small.

d. The all optical switch has no qualitative dependence on the polarization of the probe and switching beams.

e. The switching mechanism does not require elaborate frequency stabilization of either the cavity resonances or the probe and control fields to relevant atomic transitions to realize the switch.

The cavity based all optical switch described above exhibits two distinctive high and low states depending on the cavity transmission output. The high and low states can be distinguished with high fidelity. The input and output sources (in the context of all optical switches) in this case are purely isolated since these are derived from two independent driving lasers. The all optical switch demonstrated above is cascadable. The transmitted output of the cell cavity system from one set-up can be used to drive a second set-up constructed in a similar fashion. The switching phenomena is robust and is independent of the small variations in phase, frequency and intensity of the probe beam. Given the fact that the switch operates with powers in the few mW regime, it does not however, satisfy the low power switching regimes that have been achieved with very low number of photons [27, 30].

References

- [1] B. E. A. Saleh and M. C. Teich, *Fundamentals Of Photonics* (John Wiley & Sons, Inc., Hoboken, New Jersey, 2007).
- [2] H. Wang, D. Goorskey, and M. Xiao. Controlling light by light with three-level atoms inside an optical cavity. *Opt. Lett.* 27, 1354 (2002).
- [3] H. Wu and M. Xiao. Cavity linewidth narrowing and broadening due to competing linear and nonlinear dispersions. *Opt. Lett.* 32, 3122 (2007).
- [4] M. Motsch, M. Zeppenfeld, P. W. H. Pinkse and G. Rempe. Cavity-Enhanced Rayleigh Scattering. *New Journal of Physics.* 12 (2010) 063022.
- [5] H. Wang, D. Goorskey, and M. Xiao. Enhanced Kerr Nonlinearity via Atomic Coherence in a Three-Level Atomic System. *Phys. Rev. Lett.* 87, 073601 (2001).
- [6] W. Yang, A. Joshi, and M. Xiao. Controlling dynamic instability of three-level atoms inside an optical ring cavity. *Phys. Rev. A.* 70, 033807 (2004).
- [7] H. Wu, M. Xiao, and J. Gea-Banacloche. Evidence of lasing without inversion in a hot rubidium vapor under electromagnetically-induced-transparency conditions. *Phys. Rev. A.* 78, 041802(R) (2008).

-
- [8] H. Wu, J. Gea-Banacloche, and M. Xiao. Splitting of atom-cavity polariton peaks for three-level atoms in an optical cavity. *Phys. Rev. A.* 80, 033806 (2009).
- [9] J. Gea-Banacloche, H. Wu, and M. Xiao. Transmission spectrum of Doppler-broadened two-level atoms in a cavity in the strong-coupling regime. *Phys. Rev. A.* 78, 023828 (2008).
- [10] X. Yu, D. Xiong, H. Chen, P. Wang, M. Xiao, and J. Zhang. Multi-normal-mode splitting of a cavity in the presence of atoms: A step towards the superstrong-coupling regime. *Phys. Rev. A.* 79, 061803(R) (2009).
- [11] L. A. Lugiato. Theory of optical bistability. *Progress in Optics.* XXI, 70-204, 1984.
- [12] H. M. Gibbs. *Optical Bistability: Controlling Light with Light.* (Academic, New York, 1985).
- [13] L. A. Orozco, H. J. Kimble, A. T. Rosenberger, L. A. Lugiato, M. L. Asquini, M. Brambilla, and L. M. Narducci. Single-mode instability in optical bistability. *Phys. Rev. A* 39, 1235 (1989).
- [14] J. Gripp, S. L. Mielke, and L. A. Orozco. Evolution of the vacuum Rabi peaks in a detuned atom-cavity system. *Phys. Rev. A.* 56, 3262 (1997).
- [15] J. P. Lowenau, S. Schmitt-Rink, and H. Haug. Many-Body Theory of Optical Bistability in Semiconductors. *Phys. Rev. Lett.* 49, 1511 (1982).
- [16] A. Tredicucci, Y. Chen, V. Pellegrini, M. Borger, and F. Bassam. Optical bistability of semiconductor microcavities in the strong-coupling regime. *Phys. Rev. A.* 54, 3493 (1996).
- [17] J. Xue and S. R. Forrest. Organic optical bistable switch. *Appl. Phys. Lett.* 82, 136 (2003).

-
- [18] J. Mlynek, F. Mitschke, R. Deserno, and W. Lange. Optical bistability from three-level atoms with the use of a coherent nonlinear mechanism. *Phys. Rev. A* 29, 1297 (1984).
- [19] A. Lambrecht, E. Giacobino, and J. M. Courty. Optical nonlinear dynamics with cold atoms in a cavity. *Opt. Commun.* 115, 199 (1995).
- [20] A. Joshi, A. Brown, H. Wang, and M. Xiao. Controlling optical bistability in a three-level atomic system. *Phys. Rev. A.* 67, 041801(R) (2003).
- [21] H. Wang, D. J. Goorskey, and M. Xiao. Bistability and instability of three-level atoms inside an optical cavity. *Phys. Rev. A.* 65, 011801(R) (2001).
- [22] A. Brown, A. Joshi, and M. Xiao. Controlled steady-state switching in optical bistability. *Appl. Phys. Lett.* 83, 1301 (2003).
- [23] H. Wang, D. Goorskey, and M. Xiao. Controlling the cavity field with enhanced Kerr nonlinearity in three-level atoms. *Phys. Rev. A.* 65, 051802(R) (2002).
- [24] R.W. Boyd. *Nonlinear Optics*. 2nd edition (Academic Press, 2002).
- [25] A. E. Siegman. *Lasers*. University Science Books, Mill Valley, CA, 2003.
- [26] C. J. Hood, M. S. Chapman, T. W. Lynn, and H. J. Kimble. Real-Time Cavity QED with Single Atoms. *Phys. Rev. Lett.* 80, 4157 (1998).
- [27] K. Birnbaum, A. Boca, R. Miller, A. Boozer, T. Northup, and H. Kimble. Photon blockade in an optical cavity with one trapped atom. *Nature* 436, 87 (2005).
- [28] X. Hachair, L. Furfaro, J. Javaloyes, M. Giudici, S. Balle, J. Tredicce, G. Tissoni, L. A. Lugiato, M. Brambilla, and T. Maggipinto. Cavity-solitons switching in semiconductor microcavities. *Phys. Rev. A.* 72, 013815 (2005).

-
- [29] T. Tanabe, M. Notomi, S. Mitsugi, A. Shinya, and E. Kuramochi. Fast bistable all-optical switch and memory on a silicon photonic crystal on-chip. *Opt. Lett.* 30, 2575 (2005).
- [30] J. Zhang, G. Hernandez, and Y. Zhu. All-optical switching at ultralow light levels. *Opt. Lett.* 32, 1317 (2007).
- [31] S. E. Harris. Electromagnetically Induced Transparency. *Phys. Today* 50, 36 (1997).
- [32] H. Schmidt and A. Imamoglu. Giant Kerr nonlinearities obtained by electromagnetically induced transparency. *Opt. Lett.* 21, 1936 (1996).
- [33] A. S. Zibrov, M. D. Lukin, and M. O. Scully. Nondegenerate Parametric Self-Oscillation via Multiwave Mixing in Coherent Atomic Media. *Phys. Rev. Lett.* 83, 4049 (1999).
- [34] Y.-F. Chen, Z.-H. Tsai, Y.-C. Liu, and I. A. Yu, *Opt. Lett.* 30, 3207 (2005).
- [35] D. A. Braje, V. Balic, G. Y. Yin, and S. E. Harris. Low-light-level nonlinear optics with slow light. *Phys. Rev. A.* 68, 041801(R) (2003).
- [36] S. E. Harris and Y. Yamamoto. Photon Switching by Quantum Interference. *Phys. Rev. Lett.* 81, 3611 (1998).
- [37] A.M.C. Dawes, L. Illing, S.M. Clark, and D.J. Gauthier. All-optical switching in rubidium vapor. *Science.* 308, 672 (2005).
- [38] Claude Cohen-Tannoudji, Bernard Diu und Franck Laloe. *Quantum Mechanics*. Wiley-Interscience. 2006.

4

Experiments with cold atoms in a cavity

4.1 Introduction

Cold atoms in cavities [1, 2] have spawned an enormous amount of scientific activities in the last ten years. With the advent of laser cooling [3–6] leading to the magneto-optical trapping of neutral atoms [7–11] and the subsequent experimental realization of quantum degenerate systems [12–17], one could explore a plethora of physical phenomena in the context of light matter interactions using optical cavities of reasonably high finesse. Till date, to the best of our knowledge, detection of cold and ultracold molecules [18–31] is largely destructive utilizing either trap loss mechanisms or mass spectrometry methods relying on the creation of molecular ionic species from the parent molecules, which are then subsequently detected on a channel electron multiplier (CEM)

or from techniques that allow reconversion of the molecules to its constituent atoms using Feshbach resonances. The technological breakthroughs in thin film technology made it possible to realize cavities with ultra-high finesse in the optical domain [32, 33], hitherto inaccessible to physicists who wanted to explore dynamics of atom-cavity interactions using tailor made Hamiltonians [34–38]. One could now use optical cavities for precision measurements relating to spectroscopy of cold and ultracold molecules created either from cold atoms or degenerate quantum gases.

A cavity could enable frequency sensitive non-destructive detection of molecular states by coupling the weak molecular fluorescence over and above the atomic fluorescence, if any, to the mode of the cavity. The first step towards realizing this objective would be to understand and characterize reliably the interaction of cold trapped atoms with the mode of an optical cavity. Cavity assisted atom detection and atomic state readout has already been established in the community with high fidelity and efficiency of detection [39–44]. The physics goals of our lab at the Raman Research Institute, Bangalore are geared towards exploring atom-cavity interactions, atom-ion interactions towards understanding cold chemical reactions, synthesis and detection of cold polar molecules. In this context, the design and construction of a hybrid trap apparatus which combines the relevant technologies necessary for trapping neutral atoms and ions with an optical cavity was envisioned and efforts were made towards the experimental realization of such a system. The present chapter focuses in detail the design, construction and characterization of some of the key features of the afore-mentioned hybrid trapping instrument and follows it up with some of the initial experiments that were performed in the hybrid trap to explore the dynamics of atom-cavity interactions in the transient and steady state regime.

The chapter is organized in the following manner. Section 4.2 of the current

chapter outlines the physics goals that are of primary interest and the technological issues that need to be addressed in order to realize the stated physics objectives. In section 4.3 we shall describe the design and construction of the UHV chamber housing the experiment. We shall point out the key components that have been incorporated to address the physics goals that we want to address. Following this is subsection 4.3.1 where we shall elaborate on the design, mounting, alignment and characterization of the optical Fabry-Perot cavity which is the key tool for the experimental observations reported in this chapter. In section 4.5 we shall move into characterizing the magneto-optical trap (MOT) realized in experimentally in the UHV system constructed by us. We shall then describe the experimental realization of coupling light from cold atoms trapped in the MOT into cavity modes in section 4.7. Following this in section 4.8 we shall focus on the dynamics of atomic population by a periodic modulation on the MOT repumper beam as measured by the photomultiplier tubes (PMTs) placed along the cavity axis in transmission and the spatial filter assembly to pick up fluorescence from trapped atoms in the MOT. In section 4.9 we shall try to explain qualitatively the dynamics of the atomic population measured by the PMT along the MOT spatial filter axis by an effective simplified four level system using a density matrix approach. Following this in section 4.10 we shall try to give a qualitative understanding of the dynamics of the composite atom cavity system using a simplified system of a two level atom in a cavity for the experimental observations as reported in section 4.9. Next in section 4.11 we shall demonstrate the realization of collective strong coupling achieved in the composite atom cavity system through the experimental observation of normal mode splitting [45–47] for cold atoms trapped in the MOT and located at the mode of the optical cavity. Finally in section 4.12 we conclude by summarising the experiments and observations reported in this chapter.

4.2 Experimental requirements

The experiment was designed keeping the following physics goals in perspective:

1. The experiment should be capable of magneto-optical trapping (MOT) relevant isotopes of multi-species alkali metals of our interest like Rubidium (Rb), Potassium (K) and Cesium (Cs). This would enable us to investigate formation of homonuclear and heteronuclear cold molecules from the participating atomic species.

2. The necessity of an optical cavity as a detector for low light level signatures of atomic and molecular fluorescence from the species of our interest. The cavity would act as a frequency sensitive detector at low light levels empowering us with the ability of non-destructive detection of molecular species of our interest.

3. A polar molecule trap along the lines of [48] was fabricated using a combination of wire electrodes wound around a scaffolding. This wireframe should possess the ability to impose large gradient fields such that the hetero-nuclear dipolar molecules created from the cold atoms can be trapped in the same spatial volume at the trap center.

4. The network of electrodes that are constructed to form the above Stark field trap are designed to enable ion trapping of alkali or alkaline earth elements like Rb^+ , Cs^+ , K^+ and Ca^+ . Obviously the field requirements for ion trapping and dipolar molecular trapping are quite different and only one of the two kinds of trap is possible within the structure at any given time.

The technical issues that we needed to address in order to experimentally explore the physics goals are:

1. A very important and crucial aspect of the vacuum system was to ensure spatial overlap of the cavity mode with the centers of the magneto-optical trap and the two wireframe traps. Ensuring the spatial overlap amongst the inter-species traps with the cavity mode would enable us to investigate signatures of

atom-cavity interactions, atom-ion and ion-molecule interactions in the cavity mode.

2. We wanted to operate the linear RF Paul trap with thin wires [48] so that we have the freedom to generate high electric fields at the center of the atom trap and investigate the influence of high electric fields on the atom-cavity interactions and also examine experimentally the trapping of polar molecules that may be formed from the atomic species involved. This would mean that the ion trap constructed from the thin wires should be of small geometrical dimensions so that high electric field gradients are possible around the central region of the MOT.

3. A technical issue that arises when one wants simultaneous operation of a magneto-optical trap with a thin-wire ion trap is shadow and diffraction effects that arise due to the wires itself. The thin wire ion trap should also allow the relatively big MOT cooling beams of 10mm diameter to pass unhindered causing minimal diffraction at the center of the MOT.

4. Further, one needs to ensure that wires of least thickness, high tensile strength, good thermal and electrical conductivity as well as possessing the least possibility of getting magnetized (either temporarily or permanently) when the anti-Helmholtz coils of the MOT are in operation.

5. The requirement of a channel electron multiplier (CEM) for detecting and recording ions that are non-fluorescing should be incorporated in the design of the vacuum assembly.

6. The mounts for the ion trap should be made of ceramic which has very good ultra-high vacuum (UHV) and electrically insulating properties.

4.3 Design and construction of UHV system

Keeping the above physics and technical aspects in mind, we came up with the following layout of the internal components of the UHV assembly as given in

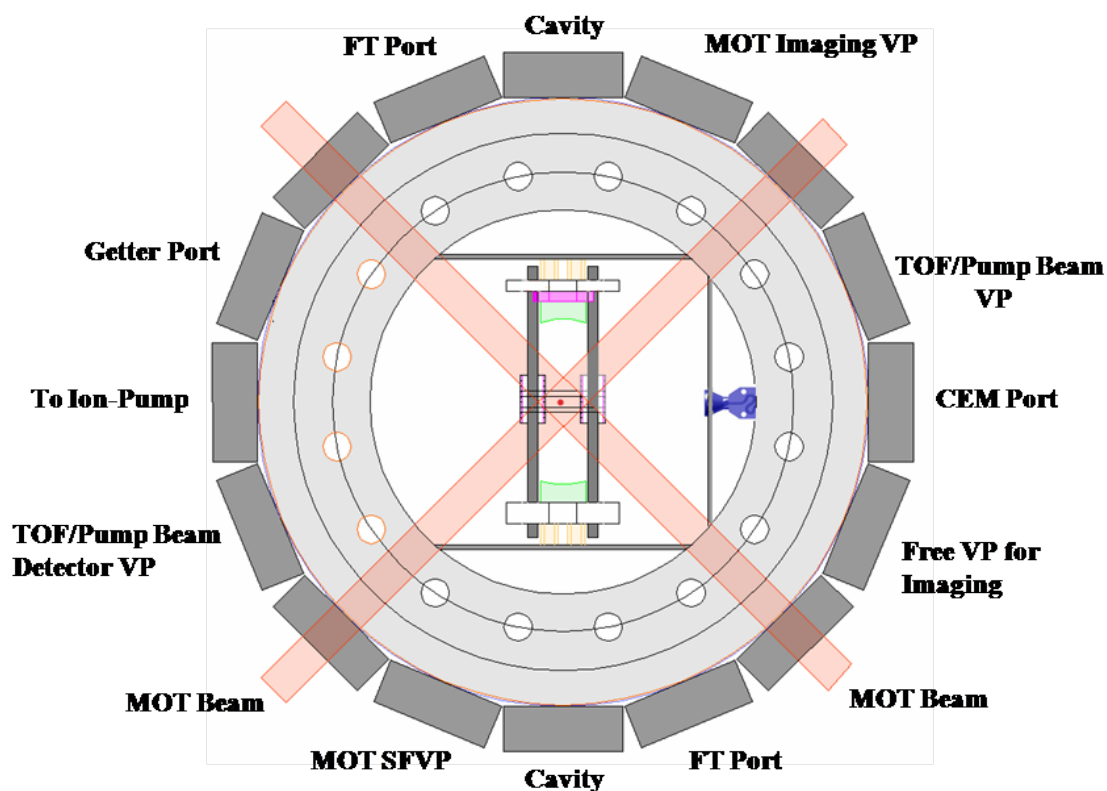


FIGURE 4.1: Schematic of the experimental setup. The Fabry-Perot cavity (mirrors shown in green) as mounted in the 16 port Kimball Physics chamber is shown along with two pairs of MOT beams for cooling and trapping the neutral atoms. The third pair of MOT beams is along the direction perpendicular to the plane of the figure. The filled circle (in red) at the center depicts a cold cloud of atoms trapped in the MOT. Not shown in the picture are the pair of anti-Helmholtz coils used for trapping the atoms in the MOT. Also not depicted in the schematic is the pair of shielding electrodes for compensating the cavity piezo voltage that hinders the operation of the RF ion trap and the aluminium housing with the attached wire grid which houses the channel electron multiplier (CEM) for ion detection. VP stands for viewport, FT stands for feedthrough and SFVP stands for spatial filtering viewport.

Fig. 4.1. We came up with the design keeping a sixteen port chamber in view which allows six independent MOT cooling beam ports (of which four are in the same plane) and twelve other ports for various other beams and components.

The view ports in plane of the chamber would have a free diameter of 16mm to allow the MOT beams of 10mm diameter to easily pass through. Additionally we wanted to keep the coils for the MOT as closely separated as possible so

that with minimal operating current (thus ensuring lower heating up of the coils) through the MOT coils we could successfully operate the magneto-optical trap. The UHV system was manufactured from SS316 by Kimball Physics Inc., USA to ensure least magnetization of the system while operating the experiment on a long term basis. Further, mounting the optical cavity and the CEM for ion detection was enabled via the groove grabber technology provided with the vacuum system. The final assembly of the central part of the vacuum system with all the key components are shown in Fig. 4.2.

The cavity is mounted symmetrically with respect to the chamber using mounting grooves provided in the inner walls of the chamber. The groove grabbers provide a rigid mounting to the entire cavity structure. The mirrors are mounted onto MACOR machinable ceramic holders. One of the holders has an additional annular piezo electric transducer (procured from Piezomechanik Germany) placed under the mirror. This enables scanning of the cavity length over a few free spectral ranges (FSRs) of the cavity. The MACOR holders are secured to the respective groove grabbers using non-magnetic SS304 screws. Orthogonal to the cavity axis is the Ion-pump axis. The UHV chamber has a base pressure of lower than 5×10^{-10} mbar. The MACOR cavity holders have additional holes to allow SS316 non-magnetic rods, threaded at either end, to be inserted through them so as to form a cage-assembly. These rods are tightened on either side via bolts on the threadings. This unique structure maintains a steady axis of the cavity and helps in common mode rejection of any vibrations that can be picked up on either cavity mirror holder through the groove grabbers.

Uncoated CF (conflat) viewports were used on all optically transparent ports. The MOT beam configuration is illustrated in Fig. 4.2. Additional viewports were used for allowing an external probe beam along the cavity axis and measuring the transmission of the cavity. A different viewport apart from the ones mentioned above was used to monitor the cold atom cloud. Photomultiplier

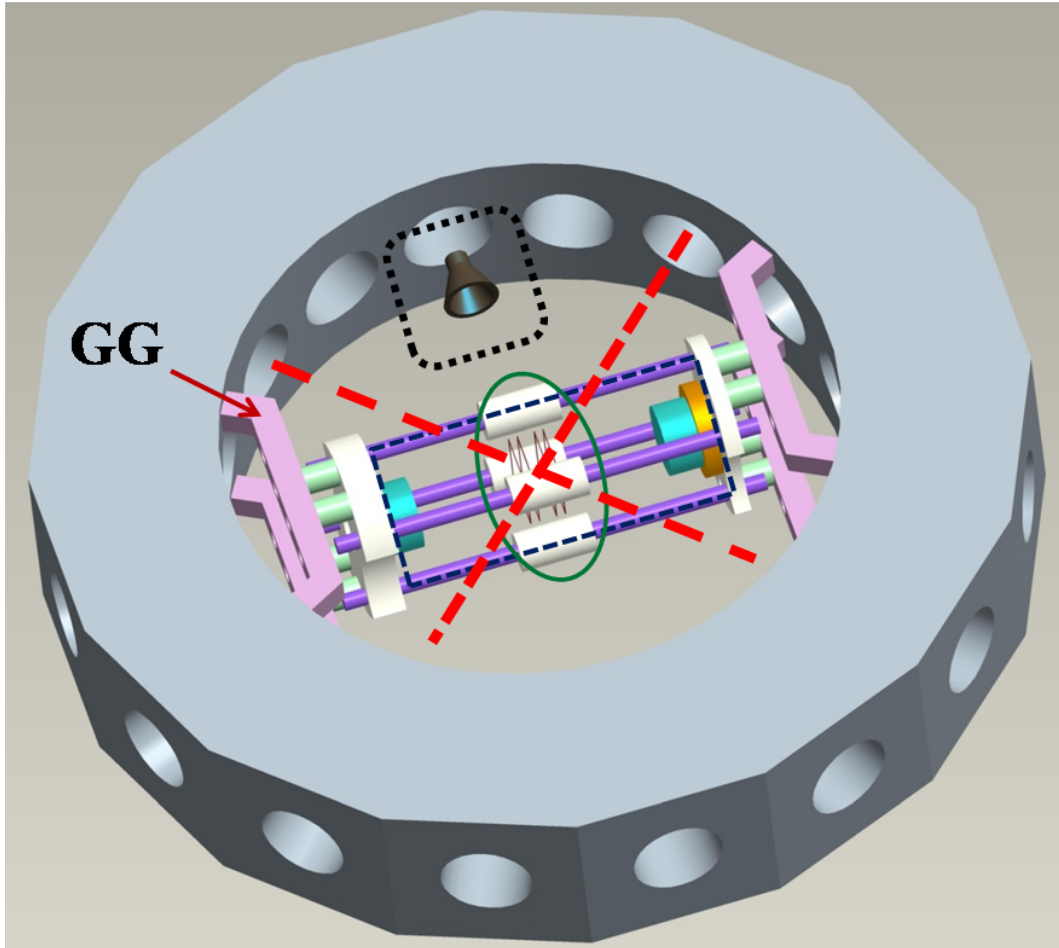


FIGURE 4.2: Three dimensional schematic of the UHV system after mounting all the key components inside it. The Fabry-Perot cavity enclosed in the indigo (dashed) box as mounted in the 16 port Kimball Physics chamber is shown. The two pairs of MOT beams (red dashed lines) for cooling and trapping the neutral atoms is also shown in the plane of the chamber. The third pair of MOT beams is along the direction perpendicular to the plane of the figure. The area shown by green (solid line) oval box depicts the thin wireframe trap. Not shown in the figure is an additional set of thin wire electrodes (placed just beyond the wireframe trap) that ensures smooth operation of the trap by compensating the voltage applied on the cavity piezo electric transducer. The black (dashed box) denotes the CEM for detecting ions. The cavity assembly and the CEM are mounted onto the chambers using the groove grabbers denoted by GG.

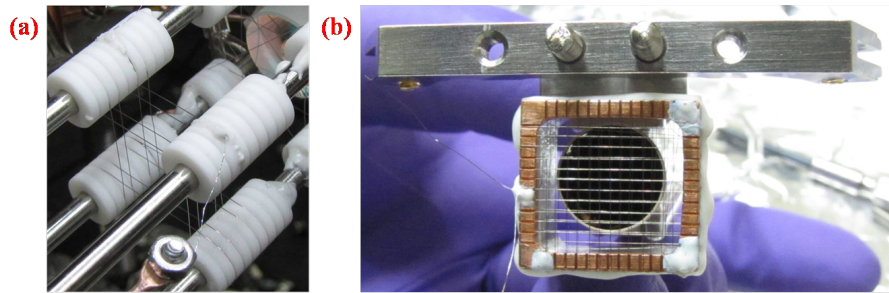


FIGURE 4.3: (a) Close up view of the thin wire ion trap with one of the cavity mirrors in the background. The shielding grid for the high voltage on the piezo electric transducer can be seen oriented between the thin wire ion trap and the cavity mirror. (b) The channel electron multiplier (CEM) placed inside the grounding box constructed of aluminium. Also shown in the figure is the shielding grid to compensate for the voltage applied on the CEM.

tubes (model number R636-10) from Hamamatsu Photonics, Japan are used at all places for light detection through the cavity axis as well as fluorescence measurements from the cold cloud in the MOT. The chamber cavity mounting arrangement is illustrated in Fig. 4.2.

The ion pump is connected to a 4-way CF40 cross from Pfeiffer Vacuum GmbH via a CF600-CF40 reducing flange from Kurt J. Lesker Inc. as shown in Fig. 4.4. The remaining 3 free ends of the 4-way cross are distributed in the following manner: the one having a direct line of sight to the ion pump leads to a conical CF40-CF16 reducing nipple from Pfeiffer Vacuum GmbH which connects the cross (and hence the ion pump) to the chamber, the top port of the 4-way cross is connected to an I-piece which houses the Titanium sublimation filament while the bottom port of the 4-way cross is connected to a CF40 T-connector. The two arms of the T-connector houses respectively the ion-gauge for measuring the pressure in the chamber and a gate valve assembly for isolating the entire vacuum system from the supporting turbo-molecular pump used during the chamber bake-out process.

The possibility of losing the crucial alignment of the cavity mirrors prevented us from resorting to a high temperature bake-out of the vacuum system in the earlier stages of the experiment. The mirror and the ceramic holder assembly

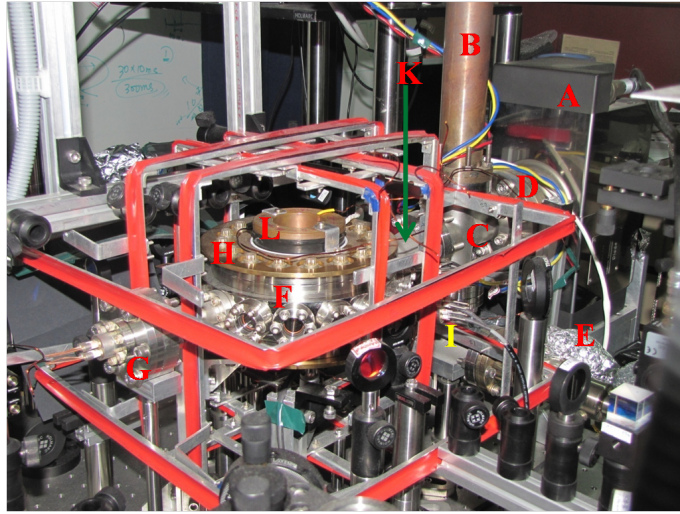


FIGURE 4.4: Side-view of the experimental UHV chamber assembly. The following components are marked by the respective alphabets: A → Ion pump, B → I-piece housing Titanium filament to be used as a sublimation pump, C → 4-way CF40 cross, D → CF600-CF40 zero length reducer to connect to ion pump, E → gate valve connected to one arm of CF40 T-connector, F → UHV chamber from Kimball Physics Inc., G → feedthrough for making electrical connections to channel electron multiplier (CEM), H → magnetic coil holder, I → feedthrough for making electrical connections to cavity piezo electric transducer, L → one of the magnetic coils for the MOT and K → conical CF40-CF16 reducing nipple connecting chamber to the ion pump via the 4-way cross. The structure wrapped in red insulating tapes is the compensation coil assembly for the experiment.

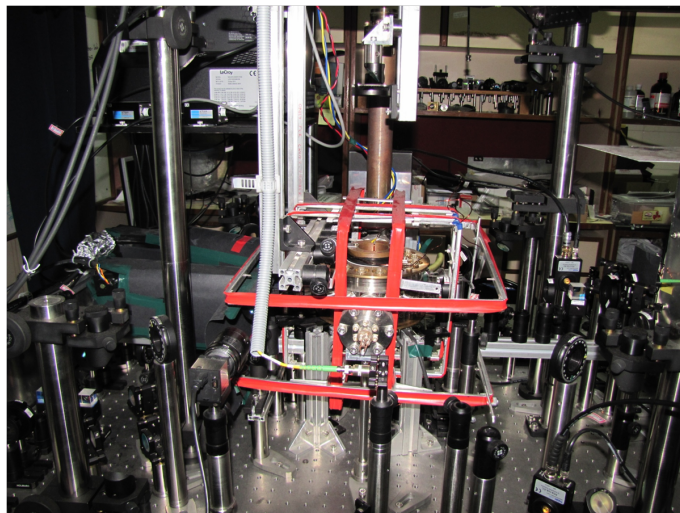


FIGURE 4.5: Front view of the experimental UHV chamber assembly with the ion pump at the far end of the chamber. Also shown are various optics used for the magneto-optical trap and cavity experiments.

have been mounted under relatively strong stress to prevent them from getting misaligned. Our fear was the high temperature bake-out might cause thermal expansions which might disturb the mirror alignment. However, even after a month long pumping by the turbo-molecular pump and the ion pump we were unable to reach a pressure below 3.4×10^{-8} mbar in the chamber. Thus we were forced to resort to a minimal all glass bakeout at around 110°C . The chamber was evenly wrapped with heating tapes and covered with aluminium foil to ensure uniform thermal gradients in the entire UHV chamber assembly. The bakeout lasted for roughly 4 days with close to 48 hours being utilized to keep the UHV chamber at an elevated steady state temperature of 110°C . The ion pump was also baked to a temperature of around 110°C by a heater connected to its body. Close to a fortnight of pumping by the turbo-molecular pump in conjunction with the ion pump was required after the bake-out stage to get to pressure around 5×10^{-10} mbar. In the interim period the titanium sublimation filament was operated twice to substantiate the pumping down of the system.

4.3.1 Cavity alignment and characterization

At the heart of the experiment lies a Fabry-Perot cavity of length 45mm mounted (with a free spectral range (FSR) of 3.33GHz) inside the chamber utilizing groove grabbers. The mirrors for the cavity procured from Linos Photonics, Germany, (currently known as Qioptic GmbH, Germany) have a radius of curvature 50mm and a quoted reflectivity of $99.97 \pm 0.01\%$ @ 780nm. The measured cavity finesse is 2100 corresponding to an average measured cavity linewidth (FWHM) of 1.58MHz. The drop in finesse from the theoretical value of 1.05×10^4 derived using the expression $\pi \frac{R_1^{\frac{1}{4}} R_2^{\frac{1}{4}}}{1 - \sqrt{R_1} \sqrt{R_2}}$ to 2100 is attributed to surface scratches and digs and also to deposits that may have contaminated the mirror surface quality during bake-out of the vacuum chamber. Here R_1

and R_2 are reflectivities of the two mirrors forming the cavity. The alignment procedure and the characterization of the cavity is described in detail below.

The cavity is aligned using an external seed beam from a Toptica DL100 laser and a charge coupled device (CCD) camera. The CCD camera is placed in transmission along the cavity axis. One important issue to keep in mind while aligning the cavity is to ensure that the input beam emerges from an output coupler at the end of the single mode polarization maintaining fiber which gives a relatively non-diverging Gaussian beam profile with a spot size of less than a mm. This ensures that only a very small region close to the axis of the input mirror of the cavity is illuminated when the beam is incident on it. The input beam height is adjusted so as to ensure that the light falls on the central region of the mirrors. A very small aperture is placed in the path of the input beam. A tiny pin hole made on a mm graph sheet serves as a good aperture for the beam alignment to the input cavity mirror. The graph sheet could be stuck with glue on a 2 inch lens mount for mounting purposes along the path of the input beam. The input beam passes through the aperture and falls on the first mirror. The input beam is aligned such that the reflection from the first mirror retro-reflects back along the same direction. Since the input mirror has two surfaces, one concave and the other flat, we see that two reflections of contrasting divergence arise due to the reflection from either surface. If the input beam position and height with respect to the first cavity mirror is adjusted to perfection, then one should be able to observe the reflection from the flat surface directly retro-reflecting back through the small aperture while the diverging reflection from the concave surface of the input mirror being aligned concentrically around the aperture.

Keeping the position of the first mirror fixed, we now focus our attention on the rear cavity mirror. The input intensity to the cavity is kept extremely low such that the charge coupled device (CCD) camera remains far below the saturation level. Two spots well separated on the plane of the CCD camera are

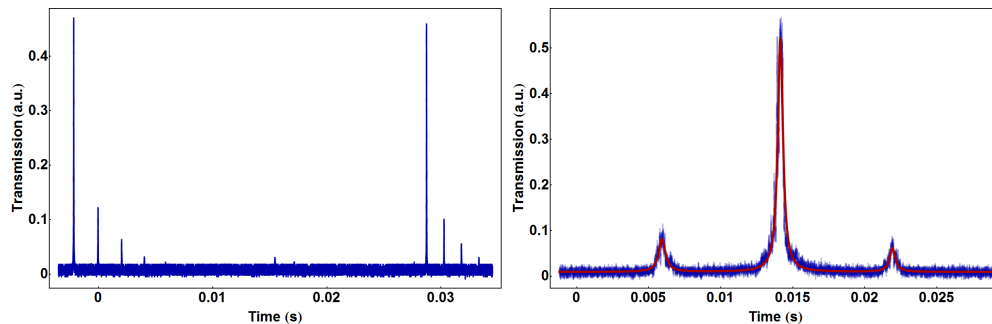


FIGURE 4.6: Left: Typical transmission pattern of the cavity as recorded by a PMT when the input probe beam frequency is fixed and the cavity is being scanned in length by the piezo-electric transducer. The two tallest peaks correspond to the two TEM_{00} modes that are visible when the cavity is being scanned over one free spectral range (FSR) of 3.33GHz. The non-uniform spacings between the right and left set of cavity transmission peaks is due to stretching of the frequency scale because of the nonlinear response of the high voltage amplifier driving the cavity piezo. Right: Typical linewidth of the cavity as recorded by a PMT when the input probe beam is being modulated in frequency by 20MHz using an electro-optic modulator (EOM) causing RF sidebands to occur on either side of the TEM_{00} mode. The cavity is kept at a fixed length by applying suitable offset voltage to the piezo-electric transducer so that it is on resonance while the input probe beam is being frequency modulated. The solid red line is a multiple Lorentzian fit to the data yielding a FWHM of 1.01MHz for the central TEM_{00} mode.

now visible due to weak cavity transmission of the input light incident on the first mirror. Initially only the back mirror of the cavity is adjusted to bring the two spots as close as possible. This serves as the rough adjustment of the cavity mirror axis. Since the mirrors are mounted on ceramic holders which are in turn fixed to individual groove grabber assemblies, it is imperative that the cavity axis is in the same line passing through the center of each mirror. This entire procedure is done with relatively relaxed status of the four quadrupole rods that pass through both ceramic holders of the front and back cavity mirrors. Once we have visible signature of the overlap of these two spots, we iteratively start tightening the nuts on these four rods which pass through the ceramic holders.

The task of final alignment of the two spots which arise due to reflections from the front and back mirrors of the cavity is then initiated. We orient the cavity mirrors by tweaking the groove grabber position as well as the screws

which mount the MACOR holders onto the groove grabbers. After a few iterations the spots merge and the camera saturates (even at that very small input beam intensity to the cavity) which emphasizes that good alignment of the mirrors have been reached. We then insert the mode matching lens and see the transmission through the cavity simultaneously on a photo-diode as well as the CCD camera. Once the mode matching lens to the cavity is in position, we can see the Hermite-Gaussian TEM_{00} modes are visible on the CCD. The transmission pattern of the cavity under vacuum as recorded by a PMT placed in transmission is shown in Fig. 4.6. The linewidth of the cavity peak in transmission is measured by referencing against a pair of RF sidebands separated by 40MHz in frequency as shown in Fig. 4.6.

4.3.2 Wireframe trap construction

In this section we shall very briefly describe the construction of the thin wire trap that has been incorporated in the UHV system and its operation as predicted by the numerical simulations done in SIMION and MATHEMATICA. The thin wire ion trap consists of four wires wrapped around ceramic spacers in a square geometry with the inner 2 wires located symmetrically around the central plane of the MOT. The ceramic spacers were machined in-house at the RRI workshop and requisite grooves of 100 micron depth were etched onto it at regular intervals of 1.5mm throughout the length of the spacer. The distance between the two inner wires of the ion trap is 3mm while the outer two wires are located 1.5mm apart from the individual central wires. This amount of space between the two inner electrodes has the dual advantage of ensuring that the center of the MOT is not blocked while simultaneously allowing large electric field gradients to be possible around the center with appropriate choice of voltage configuration on the electrodes. The wires of the trap are made of Tungsten having a thickness of 80 microns. We initially attempted to use wires

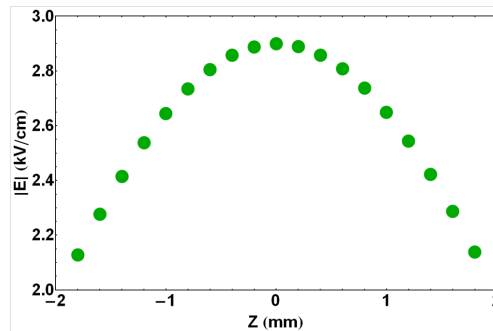


FIGURE 4.7: Electric field strength in the x-y plane as a function of z. Here the cavity axis is taken as the z direction.

of 25 micron thickness in the ion trap construction. However failure to reliably connect the wires to the copper feedthroughs without breaking them forced us to go for wires of higher thickness. The wires are wound on ceramic sleeves which sit around the quadrupole rods as shown in Fig. 4.2. These extremely thin wires were wound around the ceramic using a needle and fixed onto them permanently using TorrSeal. The windings were initiated from the cavity piezo end with the compensation wire pair for the high voltage on the cavity piezo being wound first. Care was taken to ensure that the wires maintained reasonable tension without slacking or breaking away while the winding procedure was being done.

We have earlier mentioned that we wanted to investigate the effect of electric fields in trapping of polar molecules and also explore atom-cavity physics mediated by Stark interaction generated by the electric field created from the wire ion trap. To demonstrate the strength of the electric field that can be achieved using the above wire geometry, we have shown in Fig. 4.7(d) the variation in the electric field magnitude as a function of z. For the electric field gradient reported in Fig. 4.7(d) the voltage configuration applied to the thin wire trap is as follows: starting from one end, the first outer wire is maintained at +3kV, the following inner wires is kept at +2kV, the next inner wire is maintained at -2kV while the final outer wire is kept at -3kV. Given the magnitude of electric fields

that can be generated depending on the configuration and applied voltage on the wires, one may explore trapping of polar molecules [48] or explore the steady state field induced enhancement and inhibition of spontaneous emission of atoms in an optical cavity [49]. One may also explore effects such as the change in the normal mode splitting when a composite atom-cavity system is being probed in the presence of strong steady DC electric field.

4.4 Imaging system set-up for atom and cavity

light detection and characterization of PMTs

In this section we discuss the imaging systems that were incorporated in the experiment for accurate and reliable measurements of the atom-cavity experiments that are to follow. We use identical PMTs (model number R636-10) from Hamamatsu Photonics, Japan. The pre-amplifiers (model number C7319) used in conjunction with the PMTs are again procured from Hamamatsu Photonics, Japan. For imaging the cold atoms in the MOT, we designed and set up a spatial filter assembly to minimize the background of scattered light that arose from the wireframe trap as well as from the MOT cooling and repumper beams. A schematic of the spatial filter for imaging the cold atoms in the MOT is shown in Fig. 4.8(a). We have realized a signal to noise ratio of 2 on the MOT PMT using the spatial filter assembly to detect fluorescence from trapped atoms in the MOT. A different approach was taken to measure and image the light coming out of the cavity. Here we use a combination of a single lens and an aperture to cut down the amount of background light being picked up on the PMT placed along the path. The aperture position was optimized by observing the signal being monitored on the (cavity) PMT while at the same time ensuring that the background light was brought down to a minimal level. A schematic of the imaging system along the cavity axis is also depicted in Fig. 4.8(b). This

4.4 IMAGING SYSTEM SET-UP FOR ATOM AND CAVITY LIGHT DETECTION AND CHARACTERIZATION OF PMTS

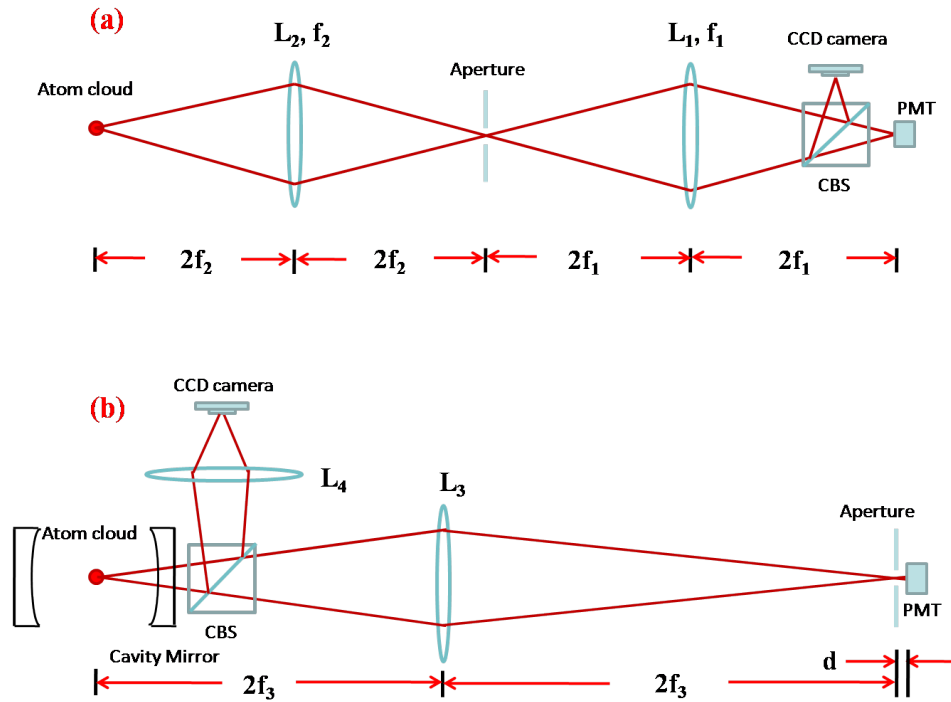


FIGURE 4.8: (a): A schematic of the spatial filter assembly to image the cold atoms trapped in the MOT and also to detect and measure the fluorescence from cold atoms onto the PMT. (b): A schematic of the imaging system for detecting and measuring the light being transmitted out of the cavity mirror. Here L_1 is a plano-convex lens while L_2 is an achromat with focal lengths $f_1 = 60\text{mm}$ and $f_2 = 75\text{mm}$ respectively. L_3 is a plano-convex lens with focal length $f_3 = 75\text{mm}$. L_4 is a lens combination system used to image cavity modes onto a CCD. The distance d is $\approx 50\text{mm}$. CBS stands for common beam splitter and CCD represents a charge-coupled device camera. The distances depicted in the figure are not to scale.

procedure ensured a high signal to noise ratio on the PMT placed along the cavity axis. Further, interference filters at 780nm with a bandwidth of $\pm 10\text{nm}$ were placed before the individual PMTs on the MOT as well as the cavity axis to reduce unwanted responses of the PMTs to ambient light. We finally covered the entire path of the individual imaging systems with thick black paper to minimize background light effects.

In order to characterize the responses of the respective PMTs an elaborate experimental characterization of the various optical elements was undertaken.

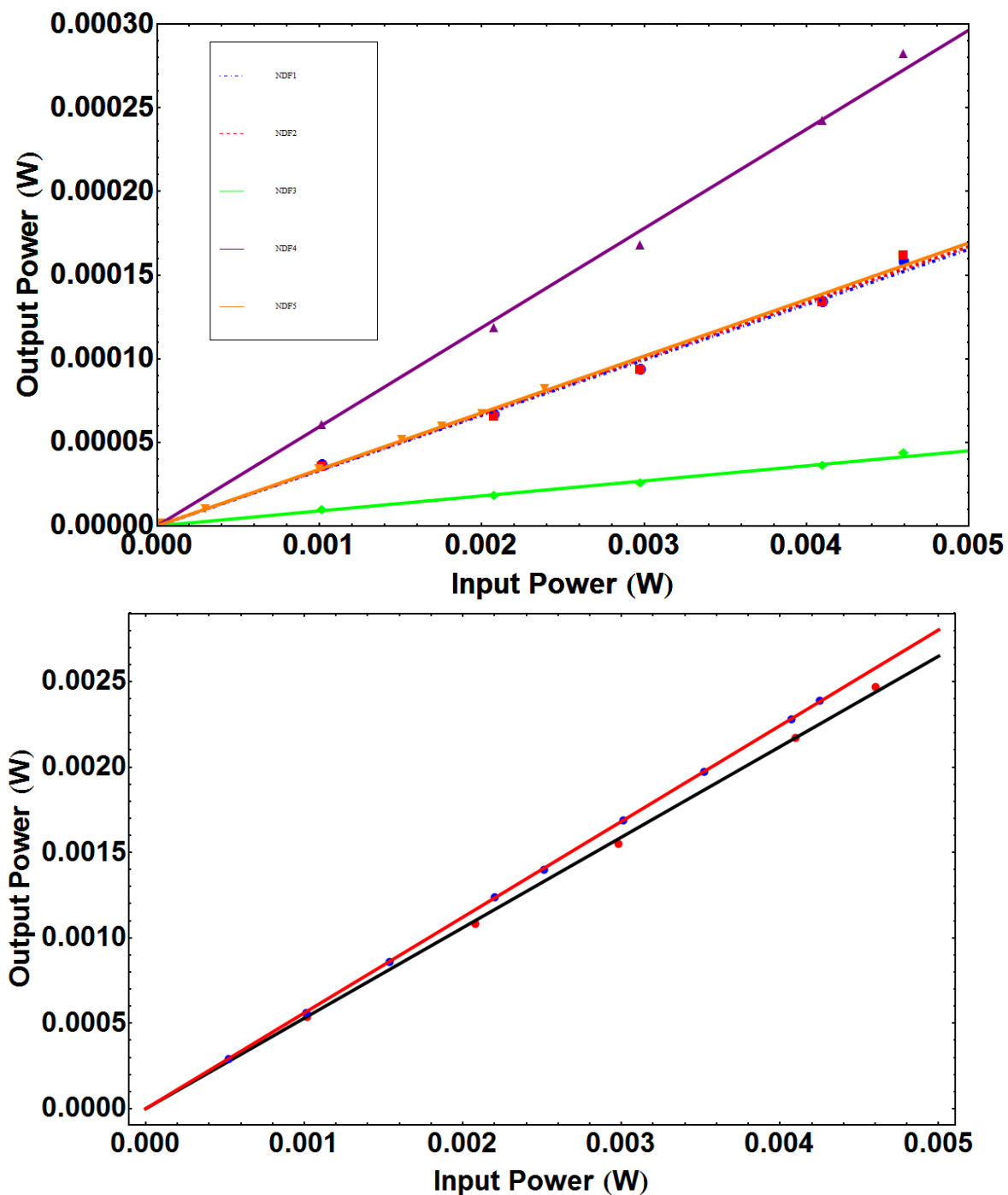


FIGURE 4.9: Top: Calibration curves for the various NDFs used in the experiment. Bottom: Calibration curves for the common beam splitters (CBS) used in the MOT spatial filter and the cavity imaging axis. The red dots represent data points for the MOT CBS while the blue points depict data for the cavity CBS.

4.4 IMAGING SYSTEM SET-UP FOR ATOM AND CAVITY LIGHT DETECTION AND CHARACTERIZATION OF PMTs

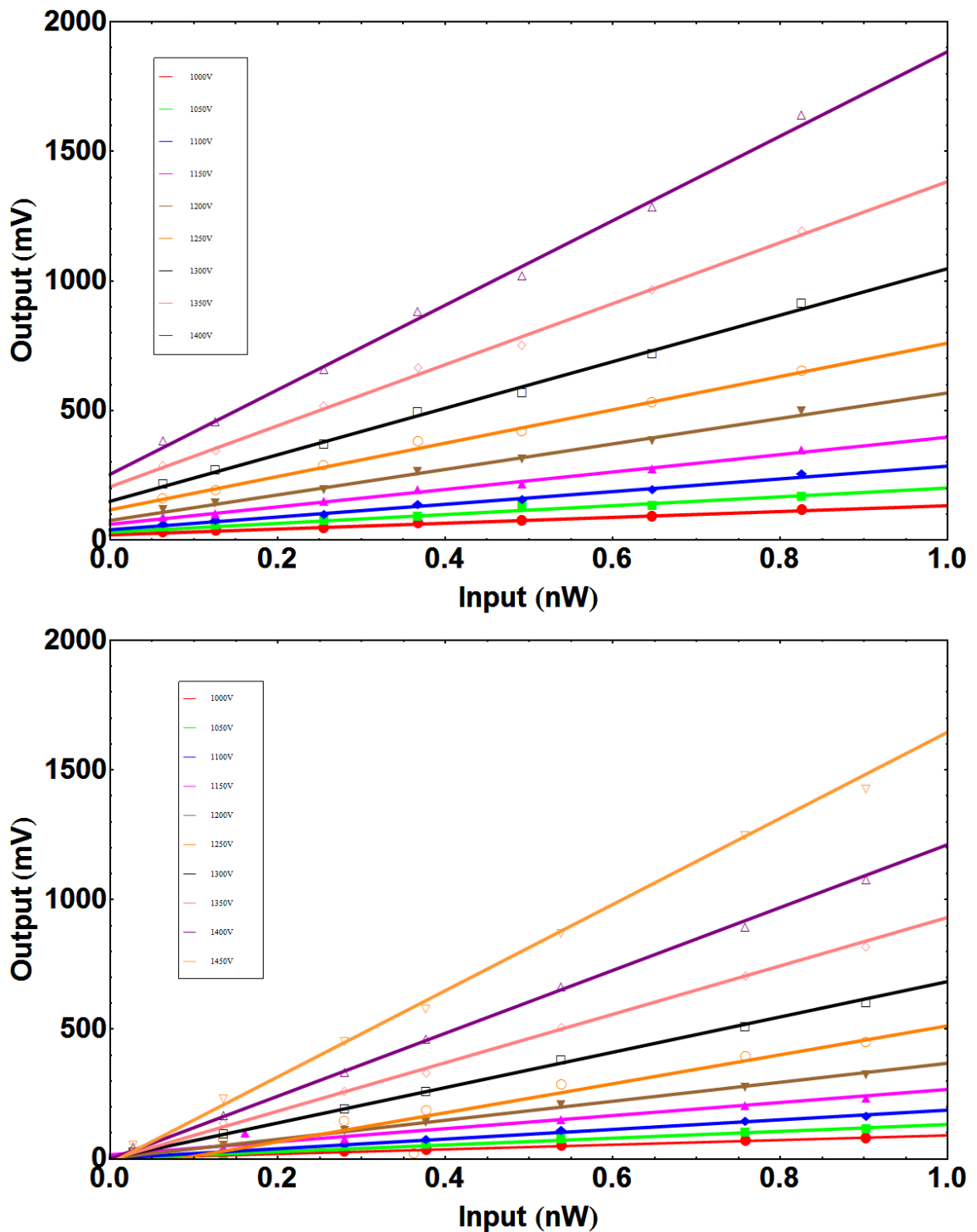


FIGURE 4.10: (Top: Calibration curves for the PMT used at the end of the MOT spatial filter set up. Bottom: Calibration curves for the PMT used to detect light out of the cavity.

Individual lenses placed in the spatial filter assembly as well as the cavity imaging apparatus were characterized. Common beams splitters (CBS) used to split light either from the cold atoms trapped in the MOT or from emission into cavity modes were also characterized (see Fig. 4.9). Additional characterization of neutral density filters (NDFs) (see Fig. 4.9) used in the experiments and in calibrating the PMTs were also done. The responses of the individual PMTs at different voltages against an input light power have been shown in Fig. 4.10. Both PMTs were operated at low bandwidth of the respective pre-amplifiers. The operating voltage of both PMTs was maintained at -1350V. The gain settings on the individual pre-amplifiers were maintained at 10^5 V/A.

The number of atoms trapped in the MOT was estimated in the following manner. The background light signal was recorded in the absence of atoms. Once the MOT was loaded fully from the ambient vapor a higher signal level was recorded. This higher signal was due to additional light from fluorescing atoms trapped in the MOT. Subtracting the background signal level from the total light level recorded in the presence of atoms gave the net light level from the cold atoms. We estimated the solid angle subtended by the first lens of the MOT spatial filter assembly. The ratio of this solid angle to the total solid angle of 4π would give us the fraction of the total power being scattered along the MOT spatial axis. The total photon scattering rate for an individual atom was then estimated using the equation

$$R_{scatt} = \frac{\Gamma}{2} \frac{\frac{I}{I_{sat}}}{1 + \frac{I}{I_{sat}} + 4\frac{\delta^2}{\Gamma^2}} \quad (4.1)$$

where Γ is the linewidth of the excited state of the ^{85}Rb D_2 transition, I_{sat} ($=1.67\text{mW/cm}^2$) is the saturation intensity for circularly polarized light, δ is the detuning of the cooling laser and I is total intensity of the MOT cooling beam being put into the experiment.

Two additional quantities are estimated from the calibration and characterization curves of the various optical elements used in the MOT spatial filter assembly and also from the calibration curves of the MOT PMT used at the end of the spatial set-up. One of these quantities denoted by *powCalib* incorporates the losses incurred at each optical element and the power to voltage ratio at the given operating voltage of the PMT. Thus, using this quantity the net power measured by the MOT PMT can be estimated. The second quantity denoted by *MOTfactor* is determined by dividing the earlier quantity *powCalib* by a product of the scattering rate $R_{scatt} \times \text{solid-angle ratio} \times h\nu$, where h is the Planck constant and ν is frequency of the MOT cooling light. The total number of atoms in the MOT can now be estimated by multiplying the net signal observed on the MOT PMT with the *MOTfactor*.

4.5 Cold atom trap characterization

Realization of a magneto-optical trap(MOT) in the designed UHV chamber was different and difficult due to the following reasons. The thin wireframe trap could create severe diffraction effects on the atoms to be confined in the MOT and thus affect effective cooling by the MOT beams. Also the cavity could cause a modification of the electro-magnetic boundary conditions perceived by the atom and thus affect the regular operation of the MOT by causing a change in the spontaneous emission rates of the atom. Another issue that needed to be addressed was the proper positioning of the cold atom cloud so that effective coupling to the cavity modes could be achieved. Further, an accurate imaging system was required to perform reliable measurement of the atom cavity interactions. These issues were in stark contrast to realizing a MOT in a conventional UHV system without an optical cavity and a thin wireframe trap overlapping the mode of the optical cavity. A clear optical axis for detecting the fluorescence of the cloud was difficult given the number of components

mounted in the UHV system.

Cold atom trapping and cooling is achieved by a regular six beam magneto-optical trap (MOT) so as to trap the atoms at the origin by balancing the radiation pressure from laser light. Fine adjustments in the position of the MOT are made possible with the MOT coil mountings through small coil adjustments. The coils comprise of 100 turns of 1.3mm diameter wire in a 10×10 cross sectional stack, wound on a copper former and is capable of sustaining over 10 Ampere continuous current without water cooling. A circulating current of 5.0 Ampere in anti-Helmholtz configuration produces a gradient magnetic(B) field of 22Gauss/cm.

We use alkali metal dispensers from SAES Getters Inc. for loading the ^{85}Rb MOT. A Rb getter (SAES: Rb/NF/4.8/17FT10+10), which emits atoms upon resistive heating by the passage of around 3.0 Amperes of current is used to create enough background vapor pressure to load the MOT. The MOT itself can either be loaded directly from the atoms emitted by the Rb getter, or alternatively, using desorbed atoms from the walls of the vacuum chamber. For all the experiments reported here, we use the direct atomic vapor from the getter to load the MOT.

The cooling light is derived from a home-built diode laser system capable of top of fringe stabilization using the Pound-Drever-Hall method. This laser is tuned to the $5^2\text{S}_{1/2}F=3 \Rightarrow 5^2\text{P}_{3/2}F'=4$ transition of the ^{85}Rb D₂ line. A part of this light goes into a 2 stage double pass acousto-optic modulator (AOM) setup and the remainder goes to a tapered amplifier (model BoosTa procured from Toptica Photonics, GmbH, Germany) system. The double pass AOM setup is used to detune the cooling beam light by 10-15MHz below the cooling transition. A second DL100 laser procured from Toptica Photonics GmbH, Germany tuned to the $5^2\text{S}_{1/2}F=3 \Rightarrow 5^2\text{P}_{3/2}F'=3$ transition of the ^{85}Rb D2 line, provides the relevant light for repumping the atoms from the dark state of the MOT. The repumper light is kept on resonance by referencing it with a saturated

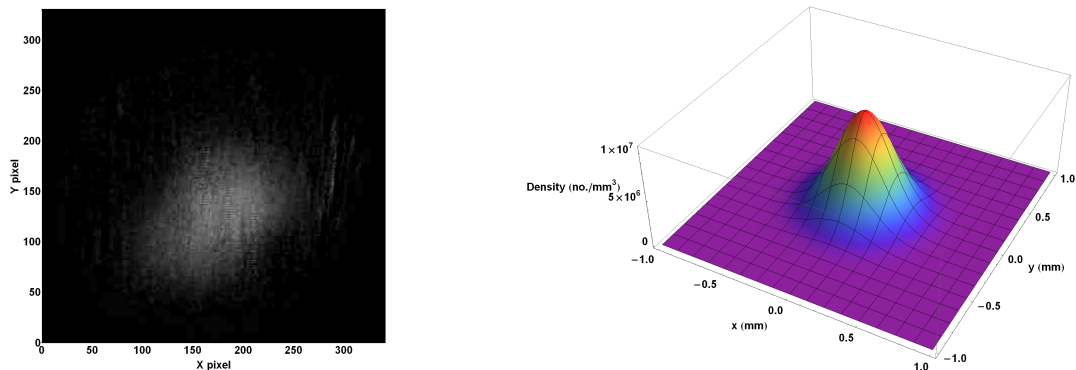


FIGURE 4.11: Left: Normalized image (after background subtraction) of cold atom cloud trapped in the MOT, as captured by a CCD camera in the spatial filtering setup. The image shows the intensity value of the pixels of the CCD chip. Right: The plot shows the number density profile of the image in both the directions by fitting a three dimensionally symmetric Gaussian density distribution.

absorption spectroscopy and stabilizing the laser via a top of fringe lock. The cooling beam intensity is amplified by feeding the light to a tapered amplifier system. Six beams, each with a diameter of 10mm and power in the range of 2.0mW - 4.5mW, of appropriate circular polarization derived from the output of the tapered amplifier system intersect at the center of the chamber. The number of atoms in the MOT vary from the high 10^5 to low 10^6 range depending on the amount of repumping light used. The spatial distribution of the MOT atoms obtained has typically a full width at half maximum of $\approx 430\mu\text{m}$. A fluorescence image of the ^{85}Rb MOT, taken by the CCD camera, placed at the end of the MOT spatial filter assembly (discussed in the previous section) is shown in Fig. 4.11. The lifetime of the cold atoms trapped in the MOT with the getter source powered off to prevent additional loading of the MOT during the decay cycle is measured to be $(4.29 \pm 0.48)\text{s}$. The loading rate of the atoms into the MOT starting from a point where the dispenser/getter source is powered on at time $t=0$ is $(42.72 \pm 6.58)\text{s}$.

4.6 Why study atom cavity dynamics with cold atoms?

In chapter 3 we have investigated the evolution of the cavity transmission through the atomic medium in the presence/absence of a control beam. Those studies were conceived to get a better understanding on what to expect when we load cold atoms into the cavity. While there are significant differences in the two cases, there are also plenty of similarities. These have been point-wise noted as follows:

Differences:

1. In the case of the MOT, we have a localized atom density, whereas in the vapor cell we have a uniform density distribution of atoms.
2. There is no additional probe/seed laser along the cavity axis.
3. The Doppler spectrum is very narrow in case of laser cooled atoms in the MOT.
4. There exists gradient magnetic fields due to the anti-Helmholtz coils of the MOT.
5. The atomic medium placed at the center of the cavity is pumped from the side and not along the cavity axis.
6. The atomic fluorescence couples to the cavity modes.

Similarities:

1. We have chosen the same atomic resonances (i.e. the D_2 transitions of the Rb atom).
2. We have the freedom to apply a seed light along the cavity axis.

The question then arises as how do the laser cooled atoms couple to a cavity mode, when the beam configuration (cooling-repumper) which extinguishes cavity mode build-up in the vapor cell cavity experiments is present in the MOT at all times. Below we probe both the steady state and transient regimes of the coupling of laser cooled atomic sample to a cavity mode.

4.7 Cold atom emission into cavity modes

Cold atoms trapped in the MOT cause light to build up in the cavity modes. We have characterized the emission from cold atoms into these modes using a PMT and a CCD. The intensity of light build up in the cavity modes is proportional to the number of atoms trapped in the MOT. We finely adjust the position of the cold atom cloud using a pair of anti-Helmholtz coils till we have the best signal to noise ratio on the cavity peaks. We also monitor the spatial profile of the modes being picked up at the end of the cavity mode imaging assembly.

We start the procedure by putting a very small voltage on the cavity piezo and adjusting it by a suitable offset voltage so as to ensure formation of cylindrically symmetric Laguerre-Gaussian(LG) modes. We position our cavity piezo at a point where we see a higher order LG mode, typically TEM_{30} . Initially poor overlap with the cold atom cloud position and the cavity mode results in a distorted LG TEM_{30} . However by adjusting the pair of MOT coils, we get to a point where we have symmetric circular profile of the LG TEM_{30} modes visible. We also ensure that the image of the cold atom cloud is at all times formed roughly at the center of the CCD array positioned at the end of the MOT spatial filter set-up. At the optimized position, light from cold atoms is coupled to the cavity modes and we can see dips in the MOT fluorescence level corresponding to peaks in the cavity emission spectrum. These dips are typically estimated to be around $\approx 15\text{-}20\%$ of the net magnitude of fluorescence recorded by the PMT placed at the end of the MOT spatial filter assembly. However a systematic characterization of these dips with varying atom number in the MOT were difficult given the day to day variation in the coupling of the MOT fluorescence into the cavity modes. A typical cavity emission spectrum from cold atoms in MOT is illustrated in Fig. 4.12.

We wanted to perform the experiment at a point where there would be typically only a single isolated LG TEM_{00} and LG TEM_{10} formed by coupling the fluorescence from trapped atoms in the MOT while scanning the cavity. This

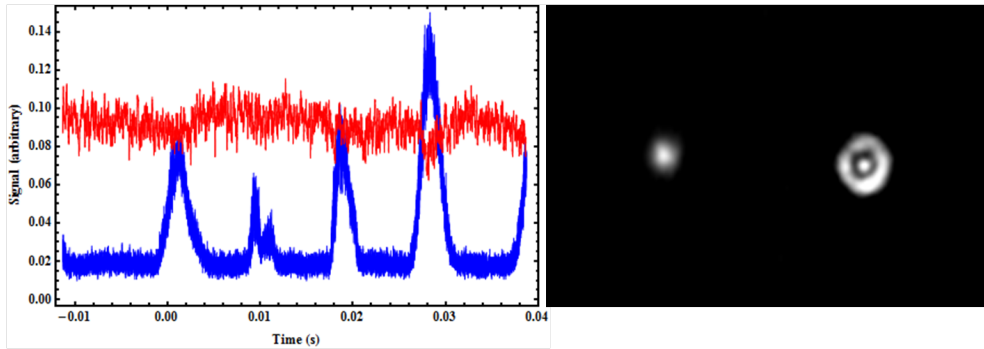


FIGURE 4.12: Left: Cavity transmission spectrum (blue trace) as recorded in PMT due to emission of light into cavity modes from cold atoms. The red trace (averaged) on top depicts the MOT light level as recorded by a PMT after spatial filtering of MOT fluorescence. Clearly visible are dips in the MOT fluorescence profile coincident with cavity modes. The first peak depicts a LG TEM_{00} mode while the fourth peak depicts a LG TEM_{10} mode while scanning the cavity piezo from a low to a high value. Right: Images of the LG TEM_{00} mode and the LG TEM_{10} mode as recorded by a charge coupled device (CCD) camera placed on the cavity axis.

would enable us to clearly avoid the spurious and complicated mode dynamics that would arise due to mode competition being built up due to high density of the cold atom cloud. Initially we tried to do the experiment at typical total cooling and repump beam powers of 24mW and 2mW respectively. However, we found that at these values of cooling and repump beam powers the spectrum of the scanning cavity is very complicated, diffuse and shows mode overlap. An example of such a spectrum is shown in the figure below. Hence we experimentally deduced the parameter range where we could get only a single isolated LG TEM_{00} and LG TEM_{10} modes by making a grid of the cooling and repumping beam powers, keeping a constant red detuning of 10MHz of the cooling beam laser, as tabulated below.

We found that the most optimal total cooling beam power was in the range 22-24mW while the total repumper beam intensity for observing a clean (as observed by both the CCD camera and the PMT along the cavity axis) TEM_{00} mode into the cavity would be in the range $50-250\mu\text{W}$. A clean TEM_{00} mode would be devoid of mode contamination from other modes. The fact that we

Table 4.1: Experimental grid to find the suitable operating range for the coupling a purely single TEM₀₀ mode from cold atoms in the MOT.

Set number	Total cooling beam power range (in steps of 2mW)	Total repump beam power (μ W)
I	14-30	100
II	14-30	150
III	14-30	200
IV	14-30	250
V	14-30	300
VI	14-30	350
VII	14-30	400
VIII	14-30	450

could go down to 50 μ W in total repump beam power and still observe reasonable amount of fluorescence over and above the background scatter on the MOT PMT, was another highlight of the experiment.

An important point to note here is that for the typical measurements as depicted in the above Fig. 4.12, we operate the MOT at very low repumping beam powers and a high gradient magnetic field. We explored in detail a large parameter space concerning the MOT cooling and repumper beam intensity as well as the gradient magnetic field for optimizing the coupling of light from cold atoms into cavity modes. We noted that the cavity transmission spectrum is complicated and unclean at higher repumper beam intensities. A host of spurious peaks appear on the regular low order LG modes at high repumper beam powers. Typically we get a clean spectrum of regular LG spatial modes at around 200-300 μ W of total repumper beam intensity and 12-30mW of total cooling beam intensity. The transmission spectrum of the cavity gets complicated again as we go up in cooling beam intensity beyond 30mW. The gradient magnetic field at this point with a constant coil current of 5.0A is 22 Gauss/cm. Higher gradients of magnetic field lead to tighter confinement of the cold atoms in the MOT and thus ensures a good overlap with the cavity modes.

We further characterize the linewidth of the LG TEM₀₀ and LG TEM₁₀ as a

4. EXPERIMENTS WITH COLD ATOMS IN A CAVITY

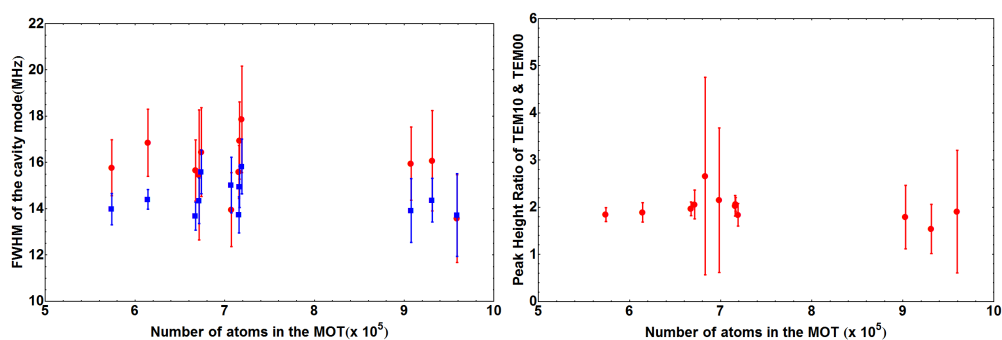


FIGURE 4.13: Left: Linewidth (FWHM) of LG spatial modes (obtained by fitting data to a Gaussian lineshape) as a function of the total number of atoms in the MOT. The filled circles are FWHM data for TEM₀₀ modes while the squares represent FWHM data for TEM₁₀ modes. Right: The ratio of peak heights for TEM₁₀ to TEM₀₀ after a Voigt profile fit to data.

function of the total number of atoms trapped in the MOT. Keeping the total re-pumping beam intensity for the MOT at a constant value of $250\mu\text{W}$, we vary the total cooling beam intensity for the MOT from 6mW - 29mW . We keep the magnetic field constant at 22Gauss/cm throughout this experiment. At each point of cooling beam power, a transmission spectrum for the cavity was recorded along with the total light level for the MOT as detected on the PMT. The cavity piezo was scanned at a rate of 12.4Hz . The entire experiment was triggered on the high voltage ramp to the cavity piezo. The full width at half maximum (FWHM) for the LG TEM₀₀ and the TEM₁₀ modes are obtained by fitting the data with Gaussian lineshapes. The typical linewidths obtained after the Gaussian fit to the data for the LG TEM₀₀ and LG TEM₁₀ is $(15.85\pm 5.42)\text{MHz}$ and $(14.46\pm 5.42)\text{MHz}$ respectively. The variation of the cavity mode linewidth for these two modes versus the total number of atoms in the MOT is shown in Fig. 4.13.

It is expected that the ideal linewidth of the cavity peaks induced by emission of light from cold atoms in the MOT can be deduced only after accounting for the natural or spontaneous emission lifetime of the excited state and also by taking into account the Zeeman shift due to the MOT coils that shall play a

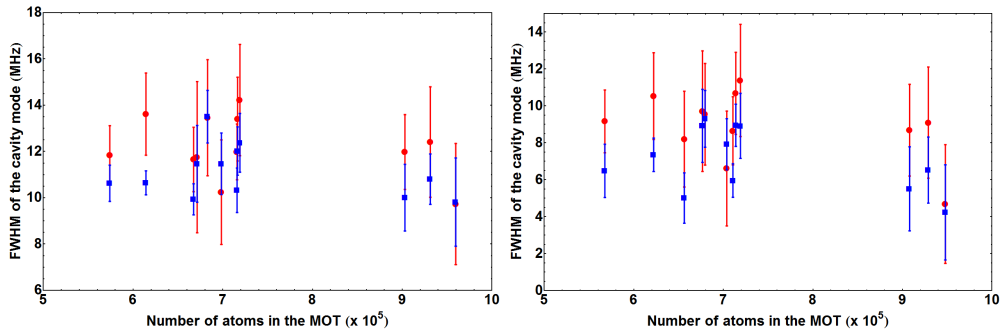


FIGURE 4.14: Left: Linewidth (FWHM) of LG spatial modes as a function of the total number of atoms in the MOT after a Voigt profile fit. The filled circles are FWHM data for TEM_{00} modes while the squares represent FWHM data for TEM_{10} modes. Right: Linewidth (FWHM) of LG spatial modes as a function of the total number of atoms in the MOT after accounting for the Zeeman shift broadening that arises due to the inhomogeneous magnetic field from the MOT coils in the anti-Helmholtz configuration.

small but significant role in altering the linewidth of emission of cold atoms in the MOT. We assume that there is no significant Doppler broadening since the atoms are being constantly cooled by the laser beams while the experiment is being conducted. For this purpose we initially fit a Voigt profile to the observed cavity lineshape by keeping the natural linewidth of the $5^2P_{3/2} F'=4$ state of the ^{85}Rb D_2 transition as a constant parameter. Fitting the cavity lineshape with a Voigt profile having this constraint, we obtain a set of parameters defining the Gaussian contribution. The full width at half maximum (FWHM) for the LG TEM_{00} and the TEM_{10} modes are now plotted against atom number after fitting via the Voigt function and is depicted in Fig. 4.14. The typical linewidths for the LG TEM_{00} and LG TEM_{10} after the Voigt profile fit is $(12.19 \pm 1.34)\text{MHz}$ and $(11.08 \pm 1.12)\text{MHz}$ respectively. We also show the variation in the peak height for these two modes versus atom number after the Voigt profile fit as shown in Fig. 4.13.

We then use these set of parameters to generate a data set which yields a Gaussian distribution. We now further account for the Zeeman shift by treating this new data set as a convolution of two Gaussian beams, one of which arises from the maximal Zeeman shift that can be accounted for due to the

axial magnetic field of the MOT coils. This shows that the true linewidth of the MOT cavity peaks for the LG TEM₀₀ and LG TEM₁₀ are (8.91 ± 1.83) MHz and (7.09 ± 1.73) MHz respectively. The full width at half maximum (FWHM) for the LG TEM₀₀ and the TEM₁₀ modes after the Gaussian deconvolution due to the Zeeman shifts are plotted against atom number in the mode as shown in the Fig. 4.14.

It is interesting to note that even after accounting for all possible broadening mechanisms such as the Doppler and the Zeeman effect, the typical linewidths for the LG TEM₀₀ and the TEM₁₀ modes lie in the range 7-9 MHz, while the inherent cavity linewidth is measured to be around 1.58 MHz using an external weak probe beam coupled into the cavity mode from a frequency stabilized diode laser referenced to the ⁸⁵Rb (Rubidium) D₂ transition. This may be attributed to the fact that for the external beam coupling into the mode of the cavity we are ensuring the best possible mode matching condition possible via coupling mirror alignment, whereas in the modes formed from cold atom emission into the cavity modes the only spatial resolution is provided via tweaking the pair of anti-Helmholtz coils of the MOT. Further there is no mechanism to ensure that the coupling at the mirrors happens at the best quality surface available on the mirror. As mentioned earlier, the mirror surface quality may have been compromised during the bake-out procedure of the ultra-high vacuum (UHV) chamber assembly. Thus there is a finite possibility that mirror aberrations prevailing at the surface of the mirror limit the linewidth that is measured in the experiment. One interesting argument in favor of the higher linewidth measured maybe due to suppression of optical cooling along the cavity axis. Given the fact that the cooling in the MOT happens via continuous spontaneous emission of photons by atoms in all possible directions, one may argue from a physical point of view that the optical cavity alters the rate of spontaneous emission along the cavity axis, thus leading to a change in the rate of

scattering of an atom located at the cavity mode. However, one needs independent verification of the axial and radial temperature of the cold atom cloud with the cavity on and off resonance to ascertain the validity of this hypothesis. The current body of work recorded in this thesis does not include any attempts at measuring the temperature of the cold atom cloud in the MOT.

4.8 Dynamics of atomic population on MOT repumper beam switching

We investigated the dynamics of the atom-cavity system by tuning the population distribution of the ground states of the D_2 line of ^{85}Rb . This was achieved by a temporal modulation of the intensity of the MOT repumper beam using an AOM. We modulated the AOM for the entire duration of the cavity scan with a 1ms period with pulse widths of $200\mu\text{s}$, $300\mu\text{s}$, $400\mu\text{s}$ and $500\mu\text{s}$ respectively. The MOT was typically operated with a total cooling beam intensity in the range 18-24mW while the total repumper beam power was kept constant at $250\mu\text{W}$.

The experiment was executed in the following manner. The cavity piezo was tuned modulated by a small voltage on the piezo and the offset voltage on it was adjusted to zoom onto a LG TEM_{00} mode formed due to emission from cold atoms trapped in the ^{85}Rb MOT. This spatial mode was confirmed by a CCD camera placed in transmission along the cavity imaging axis. The offset to the cavity piezo was adjusted at all times so that the TEM_{00} mode is always positioned at the center of the high voltage (HV) ramp fed into the cavity piezo. At this point the repumper beam intensity modulation was initiated to study the temporal dynamics of the atom-cavity system. A typical experimental run is shown in Fig. 4.15.

During each run, the decay of fluorescence from the MOT in free space as opposed to the decay of the cavity transmission was monitored by PMTs

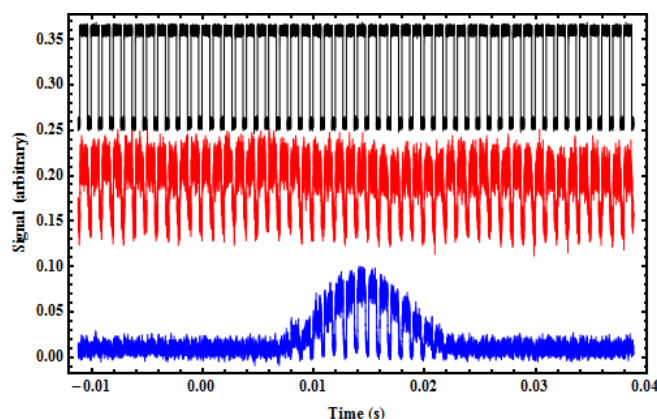


FIGURE 4.15: Cavity transmission spectrum and MOT fluorescence as recorded by PMTs due to intensity modulation of MOT repumper beam intensity. The black trace depicts the time sequence of the repumper intensity modulation. The red trace shows the MOT fluorescence and the corresponding dips in the fluorescence synchronous with the switching OFF of the repumper beam. The blue trace is the cavity mode formed due to emission by cold atoms into the cavity mode. The dips in cavity transmission are due to a drop in the MOT fluorescence when the repumper beam intensity is modulated.

positioned in the MOT spatial filter path and the cavity transmission axis. It was noted that the decay at the peak of the cavity transmission was faster than the decay of the MOT fluorescence recorded during the same repumper OFF time interval. The time constants of decay of the fluorescence from the MOT as recorded by the PMT is $62.31\ \mu\text{s} \pm 6.83\ \mu\text{s}$, while the time constant for decay of the cavity mode emission at the peak of the cavity is $31.23\ \mu\text{s} \pm 3.28\ \mu\text{s}$. A typical run recorded for a $300\ \mu\text{s}$ pulse width is shown in Fig. 4.16. The finite offsets on both signals as seen on the traces recorded by the respective PMTs are due to background light pick-up on both PMTs.

In order to verify the above observations of decay time constants of atomic fluorescence measured along the respective PMTs placed in the MOT spatial filter path and the cavity axis path, we performed the experiment in a completely different manner and regime of operation. Instead of scanning the cavity via the piezo electric transducer we zoomed onto the peak of the TEM_{00} mode by adjusting the offset voltage on the cavity piezo element. Further since that

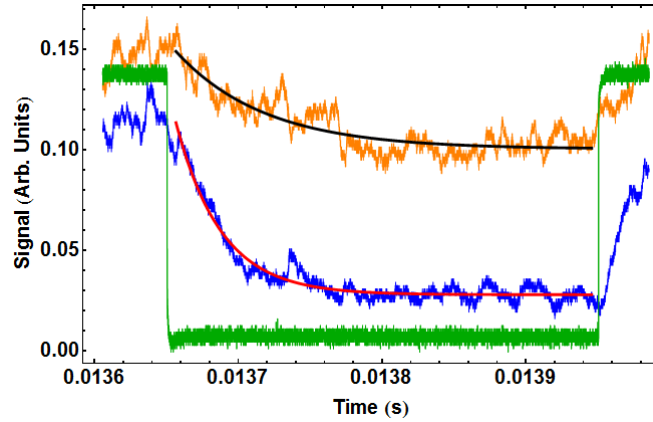


FIGURE 4.16: Typical cavity intensity and MOT fluorescence decay at the peak of cavity transmission during the OFF period of MOT repumper beam as recorded by PMTs due to intensity modulation of MOT repumper beam intensity. The orange trace depicts the decay of MOT fluorescence as picked up on the PMT after the spatial filter assembly while the blue trace depicts the decay in cavity intensity picked up in transmission by another PMT placed along the cavity axis. The green trace shows the switch off cycle of the MOT repumper beam picked up on a reference photo-diode after reflection from a glass plate. The black and red traces are single exponential decay fits on the MOT and cavity decay data respectively.

we were positioned at the peak of cavity transmission we no longer had the requirement of keeping a low power on the MOT repumper beam. Instead we performed the experiment at the following values of total cooling and repumping beam powers as given in Table 4.2.

Table 4.2: Table of operating parameters for measuring decay time constant of atomic fluorescence from cold atoms in the MOT.

Set number	Total cooling beam power (mW)	Total repump beam power (μ W)
I	30.0	2760
II	28.0	1400
III	29.6	1100

In the earlier experiment we had used a comb of pulses to systematically modulate the repumper beam intensity at various duty cycles. Now we put a single pulse of 1 millisecond duty cycle to modulate the repumper beam intensity. We operate the MOT at low getter current so that there is minimal thermal invasion on the cavity structure and piezo which sits on close proximity the

alkali metal getters. We put on the getter at low value of current and allow the system to equilibrate so that enough vapor pressure builds to load a cold atom cloud into the MOT from the background vapor. The long thermal equilibration time also aids in lesser thermal drifts of the cavity structure and the piezo-electric transducer. Thus we find that even without active stabilization on the cavity piezo via a control loop feedback, we could in fact maintain the cavity transmission at its peak for a few seconds before it drifted away slowly from the peak of resonance. In order to maintain the cavity transmission at the peak of its resonance, we set a voltage cursor level on the oscilloscope which coincided with the maximum absolute value of transmission recorded by the PMT on the cavity axis and then we gradually adjusted the offset voltage on the cavity piezo such that we maintained the voltage level already set by the pre-defined cursor. During this entire cycle of operation we ensured that we had a visible signature of the TEM_{00} mode imaged by a charge coupled device (CCD) camera placed on the path of transmission of the cavity.

A typical experimental cycle for the above described experiment is given in Fig. 4.17. The starting point on the time axis as shown in Fig. 4.17 defines the trigger point for the start of the singular pulse modulation. The typical time constants for the MOT fluorescence and the cavity intensity decay when the cavity is maintained at its peak transmission as recorded by the respective PMTs, are $(68.61 \pm 21.43) \mu s$ and $(22.78 \pm 1.78) \mu s$ respectively. The typical time constants for the MOT fluorescence decay when the cavity is maintained at its off resonance point is $(74.57 \pm 15.21) \mu s$. The finite offsets on all signals seen in Fig. 4.17 are due to background light pick-up on both PMTs placed along the cavity axis as well as at the end of the spatial filter assembly to record MOT fluorescence.

4.9 QUALITATIVE MODEL FOR ESTIMATING FLUORESCENCE DECAY TIME CONSTANT ALONG MOT SPATIAL FILTER ASSEMBLY AXIS

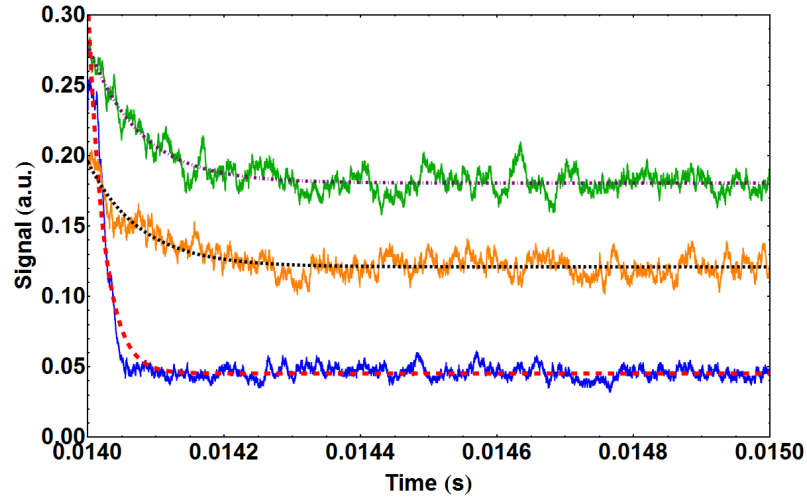


FIGURE 4.17: Cavity intensity and MOT fluorescence decay at the peak of cavity transmission during the OFF period of MOT repumper beam as recorded by PMTs due to a singular pulse modulation of MOT repumper beam intensity. Two cases are depicted: the orange trace depicts the decay of MOT fluorescence when the cavity is on resonance and maintained at the maxima of its transmission while the blue trace depicts the decay in cavity intensity picked up in transmission by another PMT placed along the cavity axis under the same condition. The green trace shows the decay of the MOT fluorescence when the cavity is maintained at off resonance point such that no light build up happens in the cavity mode. The yellow trace is shifted vertically in offset to give greater clarity on the dynamics. The black and red traces are single exponential decay fits on the MOT and cavity decay data respectively when the cavity is at the maxima of its transmission. The purple dot-dashed trace is a single exponential fit to the MOT fluorescence decay data when there is no build up of light in the cavity mode.

4.9 Qualitative model for estimating fluorescence decay time constant along MOT spatial filter assembly axis

The MOT repumper switching beam experiment is operated with the MOT cooling beams tuned to the ^{85}Rb cooling transition ($F=3 \rightarrow F'=4$, D_2 line) and the repumping beam tuned to the ^{85}Rb repump transition ($F=2 \rightarrow F'=3$, D_2 line). Here we propose a simplified four level model based only on hyperfine levels involved. We take the density matrix approach and solve for the time dependent

equations for the population terms. We model the experimentally observed decay rates of the MOT fluorescence along the MOT spatial filter assembly axis based on the rate of transfer of population from the F=3 ground state to the F=2 ground state by removal of the repumping light field applied in combination with the cooling light field in order to realize a cloud of cold atoms in the MOT. The entire model is based on the primary assumption that only cold atoms in the MOT are participating in the decay of fluorescence observed.

The total Hamiltonian for the system (see Fig. 4.18) consisting of the atom with the cooling and repumping light fields in the interaction picture is expressed as

$$H = H_0 + H_I \quad (4.2)$$

where H_0 is the Hamiltonian for the bare atom and H_I the light-atom interaction Hamiltonian. These are given by

$$H_0 = \hbar\omega_1|1\rangle\langle 1| + \hbar\omega_2|2\rangle\langle 2| + \hbar\omega_3|3\rangle\langle 3| + \hbar\omega_4|4\rangle\langle 4| \quad (4.3)$$

and

$$H_I = -\frac{\hbar}{2}[\Omega_{24}|2\rangle\langle 4|exp(-i\omega_{24}t) + \Omega_{23}|2\rangle\langle 3|exp(-i\omega_{24}t) + \Omega_{13}|1\rangle\langle 3|exp(-i\omega_{13}t) + H.C.] \quad (4.4)$$

Here the $\hbar\omega_i$ represent the energies of the levels as represented in Fig. 4.18, with ω_c and ω_r the frequencies of the cooling and repumping laser beams and Ω_{ij} denoting the Rabi frequency connecting the ground level $|i\rangle$ to the excited level $|j\rangle$. Thus the term Ω_{24} would be denoted by Ω_c , the Rabi frequency of the cooling light field and the term Ω_{13} would be denoted by Ω_r , the Rabi frequency of the repumping light field. The term ‘‘H.C.’’ refers to hermitian conjugate.

The dynamics of the system described by the above Hamiltonian can be

4.9 QUALITATIVE MODEL FOR ESTIMATING FLUORESCENCE DECAY TIME CONSTANT ALONG MOT SPATIAL FILTER ASSEMBLY AXIS

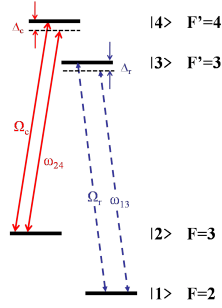


FIGURE 4.18: A simplified schematic of a four level atomic system to model the switching phenomena. The cooling field is labeled as Ω_c connecting states $|2\rangle$ and $|4\rangle$ while the repumping field is labeled as Ω_r connecting states $|1\rangle$ and $|3\rangle$.

studied using the density matrix $\rho = \sum \rho_{ij} |i\rangle\langle j|$. The time evolution of the density matrix ρ is given by the Liouville equation

$$\dot{\rho} = \frac{i}{\hbar} [\rho, H] + \mathcal{L}_{dissipation} \quad (4.5)$$

where the first term on the right hand side of equation (4.5) describes the coherent evolution of the density matrix operator ρ under the Hamiltonian H while the second term on the right hand side of equation (4.5) describes the operator $\mathcal{L}_{dissipation}$ of the Lindblad form and contains all possible modes of dissipation or relaxation existing in the system. The damping/dissipation operator is defined as

$$\mathcal{L}_{dissipation} = \sum \left[\frac{\Gamma_{ij}}{2} (2\sigma_{ij}\rho\sigma_{ij}^\dagger - \sigma_{ij}^\dagger\sigma_{ij}\rho - \rho\sigma_{ij}^\dagger\sigma_{ij}) \right] \quad (4.6)$$

Here ρ is the density matrix defined in the usual notation above while the σ_{ij} defines the creation operator for atomic excitation while σ_{ij}^\dagger denotes the annihilation operator for atomic excitation. Γ_{ij} is the decay rate connecting states $|i\rangle$ and $|j\rangle$.

The two ground states $|2\rangle$ and $|1\rangle$ can be defined as

$$|2\rangle = \begin{pmatrix} 0 \\ 1 \\ 0 \\ 0 \end{pmatrix}, \quad |1\rangle = \begin{pmatrix} 1 \\ 0 \\ 0 \\ 0 \end{pmatrix} \quad (4.7)$$

while the two excited states $|3\rangle$ and $|4\rangle$ are given by

$$|3\rangle = \begin{pmatrix} 0 \\ 0 \\ 1 \\ 0 \end{pmatrix}, \quad |4\rangle = \begin{pmatrix} 0 \\ 0 \\ 0 \\ 1 \end{pmatrix} \quad (4.8)$$

Thus σ_{ij} is defined by $g_j \cdot e_i^\dagger$ where g_j and e_i are according to the definitions given in equations (4.7) and (4.8).

The other assumptions which go into developing and solving the density matrix based rate equation model are outlined as following:

a. The $F=3$ ground state, including its six Zeeman sublevels, is modeled as a single state and the $F=2$ ground state is modeled as another state. For simplicity of nomenclature in the density matrix approach we label these as $|2\rangle$ and $|1\rangle$ respectively as shown in Fig. 4.18.

b. For simplicity, the two excited states are labeled as $|3\rangle$ and $|4\rangle$ respectively, where we again ignore the splitting of the hyperfine levels due to the presence of inhomogeneous magnetic field of the MOT.

c. We assume that polarization-dependent effects are not affecting the decay of fluorescence observed.

d. We are accounting only for spontaneous emission processes in this model and do not take into account the role of stimulated absorption.

e. We also assume that the atoms at time $t=0$ are distributed between the

4.9 QUALITATIVE MODEL FOR ESTIMATING FLUORESCENCE DECAY TIME CONSTANT ALONG MOT SPATIAL FILTER ASSEMBLY AXIS

upper ground state $F=3$ and the upper excited state $F=4$, with the relative ratio in each state only dependent on the intensities of the cooling beam light fields. The total atomic population is taken to be 1.

f. We further ignore any possibility of collisional decay of excited state atoms in the model.

g. For simplicity, we have ignored transit time broadening for the atoms when they are in the overlap region of the probe and switching fields.

Under the above assumptions, we can write down the following rate equations for atomic densities which account for relaxations and repopulations due to optical transitions (absorption and emissions) of the atoms through the beam. The final set of equations for the populations and the coherences after applying the rotating wave approximation (RWA) is given below:

$$\dot{\rho}_{11} = \Gamma_{21}\rho_{22} + \Gamma_{31}\rho_{33} + \Gamma_{41}\rho_{44} + \frac{i}{2}(\rho_{31}\Omega_p^* - \rho_{13}\Omega_p) \quad (4.9a)$$

$$\dot{\rho}_{22} = \Gamma_{42}\rho_{44} + \Gamma_{32}\rho_{33} - \Gamma_{21}\rho_{22} + \frac{i}{2}(\rho_{32}\Omega_{23}^* - \rho_{23}\Omega_{23} + \rho_{42}\Omega_s^* - \rho_{24}\Omega_s) \quad (4.9b)$$

$$\dot{\rho}_{33} = \Gamma_{43}\rho_{44} - \Gamma_{32}\rho_{33} - \Gamma_{31}\rho_{33} + \frac{i}{2}(\rho_{23}\Omega_{23} - \rho_{32}\Omega_{23}^* + \rho_{13}\Omega_p - \rho_{31}\Omega_p^*) \quad (4.9c)$$

$$\dot{\rho}_{44} = -(\Gamma_{43} + \Gamma_{42} + \Gamma_{41})\rho_{44} + \frac{i}{2}(\rho_{24}\Omega_s - \rho_{42}\Omega_s^*) \quad (4.9d)$$

$$\dot{\rho}_{21} = -\tilde{\gamma}_{21}\rho_{21} - \frac{i}{2}\rho_{23}\Omega_p + \frac{i}{2}\rho_{31}\Omega_{23}^* + \frac{i}{2}\rho_{41}\Omega_s^* \quad (4.9e)$$

$$\dot{\rho}_{31} = -\tilde{\gamma}_{31}\rho_{31} + \frac{i}{2}\rho_{21}\Omega_{23} + \frac{i}{2}(\rho_{11} - \rho_{33})\Omega_p \quad (4.9f)$$

$$\dot{\rho}_{41} = -\tilde{\gamma}_{41}\rho_{41} - \frac{i}{2}\rho_{43}\Omega_p + \frac{i}{2}\rho_{21}\Omega_s \quad (4.9g)$$

$$\dot{\rho}_{32} = -\tilde{\gamma}_{32}\rho_{32} + \frac{i}{2}(\rho_{22} - \rho_{33})\Omega_{23} + \frac{i}{2}\rho_{12}\Omega_p - \frac{i}{2}\rho_{34}\Omega_s \quad (4.9h)$$

$$\dot{\rho}_{42} = -\tilde{\gamma}_{42}\rho_{42} - \frac{i}{2}\rho_{43}\Omega_{23} + \frac{i}{2}(\rho_{22} - \rho_{44})\Omega_s \quad (4.9i)$$

$$\dot{\rho}_{43} = -\tilde{\gamma}_{43}\rho_{43} + \frac{i}{2}\rho_{23}\Omega_s - \frac{i}{2}\rho_{42}\Omega_{23}^* - \frac{i}{2}\rho_{41}\Omega_p^* \quad (4.9j)$$

where according to the above configuration of states Ω_{24} and Ω_{13} are the Rabi frequencies of the cooling and repumping light fields respectively. The Rabi

frequencies for the model above are given by

$$\Omega_{24} = \Omega_c = \mu_{24} \frac{E_c}{\hbar} = \Gamma_4 \sqrt{\frac{I_c}{2I_{sat}}} \quad (4.10a)$$

$$\Omega_{13} = \Omega_r = \mu_{13} \frac{E_r}{\hbar} = \Gamma_3 \sqrt{\frac{I_r}{2I_{sat}}} \quad (4.10b)$$

$$\Omega_{23} = 10^{-4} \Omega_c \quad (4.10c)$$

where the prefactor of 10^{-4} is the probability that an atom will absorb a photon from the cooling field and get optically pumped to state $|3\rangle$. The above factor of 10^{-4} has been estimated from the fact that in the case of laser cooling using a closed cycle transition, one out of every 10,000 atoms absorbs a photon from the cooling laser field due to off resonant pumping and ends up in an excited state which is not closed. Here I_c and I_r are the intensities of the MOT cooling and repumping laser fields respectively. I_{sat} ($=1.67\text{mW/cm}^2$) is the saturation intensity for the ^{87}Rb D_2 transition for circularly polarized light. Further Γ_4 and Γ_3 denote the lifetimes of the excited states $|4\rangle$ and $|3\rangle$ respectively. The decay from $|4\rangle$ to $|1\rangle$ is possible via an electric quadrupole transition which is estimated to be a factor (a_0/λ) lower than the dipole transition from $|4\rangle$ to $|2\rangle$ [50]. Here a_0 is the Bohr radius in angstroms and λ is the wavelength of the light coupling states $|4\rangle$ and $|2\rangle$.

We further define the following detunings:

$$\tilde{\gamma}_{21} = \gamma_{21} - i(\Delta_r - \Delta_{23}) \quad (4.11a)$$

$$\tilde{\gamma}_{31} = \gamma_{31} - i\Delta_r \quad (4.11b)$$

$$\tilde{\gamma}_{41} = \gamma_{41} - i(\Delta_r - \Delta_{23} + \Delta_c) \quad (4.11c)$$

$$\tilde{\gamma}_{32} = \gamma_{32} - i\Delta_{23} \quad (4.11d)$$

$$\tilde{\gamma}_{42} = \gamma_{42} - i\Delta_c \quad (4.11e)$$

$$\tilde{\gamma}_{43} = \gamma_{43} - i(\Delta_c - \Delta_{23}) \quad (4.11f)$$

4.9 QUALITATIVE MODEL FOR ESTIMATING FLUORESCENCE DECAY TIME CONSTANT ALONG MOT SPATIAL FILTER ASSEMBLY AXIS

where $\Delta_r = \omega_r - \omega_{13}$, $\Delta_{23} = 0$ and $\Delta_c = \omega_c - \omega_{24}$ are the detunings of the switching, the off resonant and the probe (cavity input) fields respectively with respect to the appropriate atomic transitions connected through these fields.

We define Γ_{nm} as the natural decay rate between any two levels $|n\rangle$ and $|m\rangle$. Also we define γ_{nm} as

$$\gamma_{nm} = \frac{1}{2}(\Gamma_n + \Gamma_m) \quad (4.12)$$

where Γ_n and Γ_m are the individual decay rates of the states $|n\rangle$ and $|m\rangle$ respectively.

The initial conditions at time $t=0$ for solving the equations (4.9) for the relevant parameters are as follows:

$$\rho_{11} = 0.0 \quad (4.13a)$$

$$\rho_{22} = 1.0 - \frac{\left(\frac{I_c}{2I_{sat}}\right)}{1 + 4\left(\frac{\Delta_c}{\Gamma_4}\right)^2 + \left(\frac{I_c}{I_{sat}}\right)} \quad (4.13b)$$

$$\rho_{33} = 0.0 \quad (4.13c)$$

$$\rho_{44} = \frac{\left(\frac{I_c}{2I_{sat}}\right)}{1 + 4\left(\frac{\Delta_c}{\Gamma_4}\right)^2 + \left(\frac{I_c}{I_{sat}}\right)} \quad (4.13d)$$

The detuning Δ_r of the MOT repumper beam is set to zero for solving the dynamical conditions described by the equations (4.9) above.

We solve the dynamical equations of motion for the MOT repumper beam OFF case for the population terms using a numerical algorithm such as the NDSolve function in MATHEMATICA[®]. We find that the rate of evolution of the population terms can be well described by a single exponential decay having a unique time constant. We note that for the given conditions of the experimental situation (with the requisite detuning and intensity values of 1.64Γ and $\approx 4.5\text{mW}$ of power per MOT cooling beam) for realizing the MOT we obtain from the model a decay time constant of the order of 536 microseconds. This is a factor of about 8 more than the experimentally recorded time constants by

the photo-multiplier tube (PMT) placed along the MOT spatial filter axis. Given the fact that the actual situation can be represented by the simplified model described above and the fact that we can obtain a time scale which is relatively on the same order of magnitude as the one experimentally observed, we can claim that the above model is a successful one in explaining the transient dynamics of the system when the MOT repumper beam is switched OFF. We have tried to explore the time taken to transfer the atomic population from the upper ground state $F=3$ to the lower ground state $F=2$ using the above model in terms of the total cooling light beam intensity for various values of detuning of the cooling light field, keeping all other parameters constant. A representative plot is shown below in Fig. 4.19. One may expect that if a full scale modelling of the entire atom-field system comprising of all the magnetic hyperfine sublevels of the ground and excited states is considered in three dimensions, with appropriate polarizations and decay channels incorporated, and quantum Monte-Carlo simulations are performed, then one may arrive at the timescales as measured in the experiment. Such an approach is beyond the scope of the present work and has not been dealt with in the current framework of experiments reported in this thesis.

4.10 Qualitative model for estimating fluorescence decay time constant along cavity axis

We now focus our attention towards explaining the timescales observed along the cavity axis for the MOT repumper beam switching experiment. Experimentally it is observed that the light coupling into the cavity modes to form a TEM_{00} mode is predominantly resonant with the cooling transition of ^{85}Rb . As long as

4.10 QUALITATIVE MODEL FOR ESTIMATING FLUORESCENCE DECAY TIME CONSTANT ALONG CAVITY AXIS

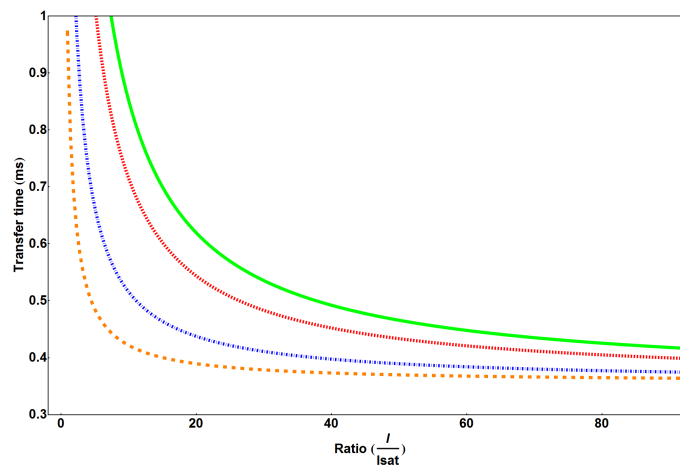


FIGURE 4.19: Plot of time taken for transfer of atomic population from the $F=3$ ground state to the $F=2$ ground state as a function of total cooling beam light intensity of the MOT keeping the cooling beam detuning as a parameter. The orange (thick dashed) curve corresponds to a detuning of 0.5Γ , the blue (dot-dashed) curve represents a plot for a detuning of 1.0Γ , the red (small dashing) curve corresponds to a detuning of 1.64Γ while the green (solid line) curve represents a plot for a detuning of 2Γ . Here Γ represents the linewidth of the $5^2P_{3/2}$ $F'=4$ state. The detuning of the MOT cooling beam is usually expressed in terms of Γ .

the MOT repumper beam is kept ON, the atomic population maintains a steady state equilibrium value with the majority population residing in the ground $F=3$ state while a small fraction (which is $\approx 18\%$ in our experiments, determined by the combined intensity of the six MOT cooling beams) resides in the excited $F'=4$ state. As soon as the MOT repumper beam is switched OFF with the aid of an AOM, the entire atomic population starts getting optically pumped into the ground $F=2$ state. This has dramatic consequences on the dynamics of the atomic population being monitored through two independent photo-multiplier tube (PMT) assemblies with one of them being kept along the cavity axis while the other one is placed at the end of a spatial filtering apparatus to pick up the fluorescence from the cold atoms trapped in the MOT.

We model the system as a two level atom (comprising of the ground state $F=3$ and the excited state $F'=4$) coupled to the cavity mode. We assume that there is no ambient magnetic field perturbing the atoms and hence we assume

that only the ground states $F=3$ and the excited state $F'=4$ of ^{85}Rb are relevant to the problem. Although we address the problem for a single atom, in effect it describes the behavior of all the atoms, which are assumed to be non-interacting, placed in the cavity mode by the trapping forces and fields of the MOT. We further ignore any sense of polarization to be associated with the various fields applied into the system. In true sense the ideal scenario would be that of a four level atomic system coupled to the field of a single mode in the cavity in the presence of two light fields addressing the atom. However one should note that even this oversimplified approach of a two level model coupled with a single mode of the cavity can provide us with the much needed crucial inputs to estimate, at least in order of magnitude, the timescales associated with the transient dynamics of the system. We embark on the density matrix formalism to address the transient dynamics that governs the time evolution of population terms of the atom and the photon in the composite atom-cavity system.

The master equation for the above system is given by

$$\dot{\rho}_{atomcav} = \frac{i}{\hbar} [\rho_{atomcav}, H_{atomcav}] + \mathcal{L}_{atomcav-dissipation} \quad (4.14)$$

where $\rho_{atomcav}$ is the 3×3 density matrix describing the composite atom-cavity system. Further $H_{atomcav}$ is the total Hamiltonian for the atom-cavity system while $\mathcal{L}_{atomcav-dissipation}$ is the dissipation operator for this system by taking into account the various decay rates (which are the sources of decoherence in the system) involved in the system. The decay rates involved are Γ and κ and arise from the finite lifetime of the excited state of the atom and the finite reflectivity of the cavity mirrors respectively. The coherent fields in the system are the field ϵ present in the single mode cavity and the atom-cavity coupling factor g given by $\sqrt{\frac{6c^3\Gamma}{\omega_c^2 w_0^2 L}}$, where L is the cavity length, w_0 is the cavity waist, Γ is the linewidth of the excited state, ω_c is the transition frequency connecting the ground and

excited states (which is also incidentally equivalent to the cavity resonance frequency) and c is the velocity of light. The field ϵ is necessary to compensate for the loss of photons due to the finite reflectivity of cavity mirrors and is given by $\sqrt{\frac{2P}{c\epsilon_0 T}}$, where P is the output power through the cavity mirror at resonance, c is the velocity of light, ϵ_0 is the permittivity of free space and T is the transmittivity of the output mirror of the cavity. The factor 2 is to account for the fact the emission out of the cavity is happening at both the mirrors. We invoke the weak field approximation and assume that ϵ is very small such that at most one excitation in the system is present. Thus the weak field approximation allows us to treat the system in the perturbative limit. We further apply the Markovian approximation under which the system is independent of its past evolution and can be regarded as having no memory.

The total Hamiltonian for the atom-cavity system is given by

$$\begin{aligned} H_{atomcav} &= H_{atom} + H_{cavity} + H_{Int} + H_{ext} \\ &= \hbar\Delta_{atom-laser}\sigma^\dagger\sigma + \hbar\Delta_{cavity-laser}a^\dagger a + \hbar g(\sigma^\dagger a + \sigma a^\dagger) + \hbar\epsilon(a^\dagger + a) \end{aligned} \quad (4.15)$$

where $\Delta_{atom-laser}$ and $\Delta_{cavity-laser}$ are the detunings of the externally applied laser field frequency ω_l from the atomic ω_a and cavity ω_c resonances respectively while the σ -s and the a -s represent the Bosonic field operators for atomic and photon excitation in the cavity mode. Thus $\Delta_{atom-laser}$ and $\Delta_{cavity-laser}$ are given by

$$\Delta_{atom-laser} = \omega_a - \omega_l \quad (4.16a)$$

$$\Delta_{cavity-laser} = \omega_c - \omega_l \quad (4.16b)$$

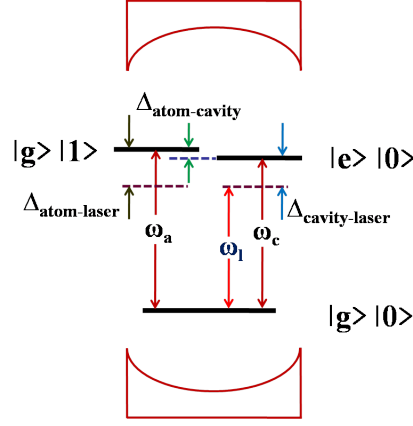


FIGURE 4.20: A simplified schematic of the two level atom-cavity system to model the switching phenomena. The three lowermost states relevant to the problem have been shown. ω_a , ω_c and ω_l denote respectively the atomic transition frequency, the cavity resonance frequency and the frequency of the external probe field. The atom-cavity detuning is given by $\Delta_{atom-cavity}$ while the cavity-laser detuning is given by $\Delta_{cavity-laser}$. The atom-laser detuning is given by $\Delta_{atom-laser}$. Ideally the states $|g\rangle|1\rangle$ and $|e\rangle|0\rangle$ are degenerate. The degeneracy is lifted in the strong coupling regime ($g \gg \kappa, \Gamma$). However, they may be detuned with respect to each other due the effective detuning between the probe laser field with the atomic and cavity transition frequencies as depicted in the most general case here.

The damping operator $\mathcal{L}_{atomcav-dissipation}$ is given by

$$\begin{aligned} \mathcal{L}_{atomcav-dissipation} &= \mathcal{L}_{atom-dissipation} + \mathcal{L}_{cavity-dissipation} \\ &= \frac{\Gamma}{2}(2\sigma\rho\sigma^\dagger - \sigma^\dagger\sigma\rho - \rho\sigma^\dagger\sigma) + \frac{\kappa}{2}(2a\rho a^\dagger - a^\dagger a\rho - \rho a^\dagger a) \quad (4.17) \end{aligned}$$

Under the weak field approximation we consider only the three lowermost states of the composite atom-cavity system which are given by $|g\rangle|0\rangle$, $|g\rangle|1\rangle$ and $|e\rangle|0\rangle$. Here $|g\rangle$ and $|e\rangle$ are the atomic ground and excited states respectively while $|0\rangle$ and $|1\rangle$ are the states with zero and one photon in the cavity mode respectively. The relevant energy level diagram is shown below in Fig. 4.20.

The two bosonic operators for creation and annihilation of photons in the

cavity mode can be represented by the matrices

$$a^\dagger = \begin{pmatrix} 0 & 0 & 1 \\ 0 & 0 & 0 \\ 0 & 0 & 0 \end{pmatrix}, \quad a = \begin{pmatrix} 0 & 0 & 0 \\ 0 & 0 & 0 \\ 1 & 0 & 0 \end{pmatrix} \quad (4.18)$$

while the similar bosonic operators for creation and annihilation of atomic excitation in the cavity mode can be represented by the matrices

$$\sigma^\dagger = \begin{pmatrix} 0 & 0 & 0 \\ 0 & 0 & 1 \\ 0 & 0 & 0 \end{pmatrix}, \quad \sigma = \begin{pmatrix} 0 & 0 & 0 \\ 0 & 0 & 0 \\ 0 & 1 & 0 \end{pmatrix} \quad (4.19)$$

The final set of equations for the population terms as well as the coherences after applying the rotating wave approximation (RWA) are given by

$$\dot{\rho}_{11} = -\kappa\rho_{11} + i(g(\rho_{12} - \rho_{12}^*) + \epsilon(\rho_{13} - \rho_{13}^*)) \quad (4.20a)$$

$$\dot{\rho}_{22} = -i(g(\rho_{12} - \rho_{12}^*) - \Gamma\rho_{22}) \quad (4.20b)$$

$$\dot{\rho}_{33} = \kappa\rho_{11} + \Gamma\rho_{22} - i\epsilon(\rho_{13} - \rho_{13}^*) \quad (4.20c)$$

$$\dot{\rho}_{12} = -\frac{1}{2}(\Gamma + \kappa)\rho_{12} + i(g(\rho_{11} - \rho_{22}) - \epsilon\rho_{23}^* + \Delta_{atom-cavity}\rho_{12}) \quad (4.20d)$$

$$\dot{\rho}_{13} = -\frac{\kappa}{2}\rho_{13} + i(\epsilon(\rho_{11} - \rho_{33}) - g\rho_{23} - \Delta_{cavity-laser}\rho_{13}) \quad (4.20e)$$

$$\dot{\rho}_{23} = -\frac{\Gamma}{2}\rho_{23} + i(-g\rho_{13} + \epsilon\rho_{12}^* - \Delta_{atom-laser}\rho_{23}) \quad (4.20f)$$

where $\Delta_{atom-cavity} = \omega_a - \omega_c$.

Following the treatment given in [51], we may set $\Gamma = 0$ and solve the above set of equations (4.20) using the NDSolve function in MATHEMATICA® with the parameters $\kappa = 2\pi \times 1.58\text{MHz}$, $g = 2\pi \times 0.31\text{MHz}$ (deduced from the following cavity parameters: cavity waist = $78\mu\text{m}$, cavity length = 45mm) and Γ

$= 2\pi \times 6.02\text{MHz}$ and with the appropriate detunings for the various fields addressing the atom and the cavity mode. We also assume the initial conditions $\rho_{11}(t=0)=1$, while $\rho_{22}(t=0)=\rho_{33}(t=0)=0$ and $\rho_{13}(t=0)=\rho_{12}(t=0)=\rho_{23}(t=0)=0$. It is seen that the decay rate of the excited state population has a time constant $\approx 4\mu\text{s}$. In contrast the experimentally measured decay rate along the cavity axis has a time constant of $31\mu\text{s} \pm 3\mu\text{s}$. The factor of about 7 difference in the decay rates observed can be attributed to a higher value of the atom cavity coupling constant used. The atom coupling constant should be suitably modified (using the relevant Clebsch-Gordon coefficients) incorporating the polarization of the field in the cavity mode as well as the quantization axis of the magnetic field applied in the system to prepare the atoms in a particular Zeeman state. A more real solution incorporating the various Zeeman sublevels with a suitably modified value of the atom-cavity coupling factor g should give a better agreement with the experimentally measured time constants.

4.11 Normal mode splitting from cold atoms

An important application of the Purcell effect [52] could be the detection single atoms with high efficiency using cavity-aided fluorescence detection and to count small numbers of atoms with very good resolution using both fluorescence and absorption methods. This technique of atom detection could well be extended to the detection of molecular states where one could stimulate the molecules to decay along the cavity mode with suitable pumping schemes. In order to realize the above physics goals, the atom-cavity interactions in our experiments need to be in the strong coupling domain. An important quantity in characterizing cavity enhanced detection is the single atom cooperativity factor [53] $C = g^2/2\kappa\Gamma$, where g is the single-photon Rabi frequency at the peak of the cavity intensity distribution, κ is the cavity linewidth (full width at half maximum), and Γ is the natural atomic linewidth. The first step towards this effect would be

to investigate the normal mode spectrum of the composite atom cavity system which is described in detail below.

We demonstrate the capability of the atom cavity system to enter the regime strong coupling ($g_{eff} \gg \kappa, \Gamma$) through collective interaction of N atoms present in the cavity mode. Here g_{eff} represents the multiatom cavity coupling constant, κ is the linewidth (FWHM) of the cavity and Γ is the spontaneous emission decay rate for the $5^2P_{3/2}|F'=4\rangle \Rightarrow 5^2S_{1/2}|F=3\rangle$ transition of the ^{85}Rb D_2 line. If N atoms collectively interact with the cavity mode, the coupling coefficient becomes $g_{eff} = g_0 \sqrt{N}$, where $g_0 \equiv \frac{\vec{\mu} \cdot \vec{E}}{\hbar}$, is the single atom cavity coupling constant. \vec{E} is the electric field amplitude of a single photon in the cavity mode volume V and polarization \hat{x} and thus g_0 is defined as $\sqrt{\frac{\hbar\omega_a}{2\epsilon_0 V}} \hat{x}$, where μ is the transition dipole moment of the two level atomic system coupling to the field of a single mode cavity, \hbar is the Planck constant divided by 2π and ϵ_0 is the permittivity of free space. The scaling of the single atom-cavity coupling constant g_0 with the square root of the number of atoms in the cavity modes allows the multiatom vacuum splitting to be observed even in a cavity of moderate mode volume and finesse.

The coupling constant g_{eff} varies in space with the cavity mode function. It also depends upon the input drive polarization coupling the two level atomic system with a single mode cavity, since the single-atom dipole coupling frequency g_0 for the driven cavity mode depends on the Clebsch-Gordan coefficient for the particular states involved. Our experimental cavity has a waist of $78\mu\text{m}$ and a finesse of $2100@780\text{nm}$ as mentioned earlier in the text. Table I gives the expected range of values for g_0 for transitions between the $F=3$ ground state and the $F'=4$ excited state of the D_2 line of ^{85}Rb at 780 nm . The strongest coupling for π -polarized light occurs for $m_F=0$ and the weakest for $m_F=3$.

The experiment to observe normal mode splitting is performed in a sequential mode as follows. All lasers are turned on or off by acousto-optic modulators

Table 4.3: Clebsch-Gordan (CG) coefficients, single-atom coupling constants g_0 for different transitions in the D_2 line of ^{85}Rb from $F=3 \rightarrow F'=4$ for different drive polarizations π or σ^+ .

	F=3	F'=4	CG	$g_0(\text{MHz})$
π	$m_F = 0$	$m_{F'} = 0$	$-\sqrt{\frac{2}{7}}$	0.1661
	$m_F = 3$	$m_{F'} = 3$	$-\sqrt{\frac{1}{8}}$	0.1098
σ^+	$m_F = 0$	$m_{F'} = 1$	$\sqrt{\frac{5}{28}}$	0.1313
	$m_F = 3$	$m_{F'} = 4$	$\sqrt{\frac{1}{2}}$	0.2197
	$m_F = -3$	$m_{F'} = -2$	$\sqrt{\frac{1}{56}}$	0.0415

(AOMs) according to the time sequence described below. The experiment is triggered on the high voltage (HV) saw-tooth pulse from the scan generator feeding the HV to the cavity piezo in vacuum. A part of this signal is fed as an external trigger to a SRS delay generator to provide voltages at appropriate times to control the AOMs for switching off the MOT cooling and repumper beams and also switch on the probe beam scanning in frequency across the cavity. The probe(seed) beam is derived from a home built extended cavity diode laser (ECDL) in Littrow configuration and is linearly horizontally polarized. The probe beam is kept scanning across the ^{85}Rb cooling transition with a $\pm 100\text{MHz}$ bandwidth by modulating the current to the laser diode of the probe ECDL as shown in Fig. 4.21. All laser beams are prepared on the experimental table and are transported via single mode polarization maintaining fibers to the experimental table. There are two saturated absorption spectroscopy (SAS) set-ups for frequency referencing the probe beam into the cavity. One of them is a reference SAS while the other is the SAS whose signal is derived only in the time window for which the probe(seed) beam to the cavity. The seed beam to the cavity is passed through an optical isolator to prevent any feedback that may arise due to back reflection from the input cavity mirror. Not shown in Fig. 4.21 is a fiber bases electro-optic modulator (EOM) from EOSpace Inc. which is utilized to calibrate the width of the cavity resonances after each experimental cycle. The EOM generates sidebands of 20MHz around the cavity

resonance mode matched with the TEM_{00} mode.

The cold atoms are initially loaded into the magneto-optical trap (MOT) and the spatial filtered signal from the MOT is observed onto a PMT till the MOT is fully loaded. Once steady state for MOT loading is reached and the PMT signal shows saturation, the experimental sequence starts with a period of 5ms. During this entire experimental sequence as shown in Fig. 4.22, the current to the anti-Helmholtz coils for the MOT are not switched off. For each period of 5ms, the MOT cooling beam is switched off after ~ 1.29 ms. The MOT repumper beam is switched off next with a delay of 150 microseconds. This essentially prepares the atoms in the $5^2S_{1/2}F=3$ state of ^{85}Rb D_2 line. The probe beam along the cavity is switched on after a further delay of $150\mu\text{s}$ for a 2ms window during which it is scanned with a symmetric triangular pulse of 50% duty cycle across the ^{85}Rb D_2 $5^2S_{1/2}|F=3\rangle \rightarrow 5^2P_{3/2}|F'=4\rangle$ transition.

The normal mode spectra are recorded versus the probe frequency detuning in transmission on a PMT placed along the cavity axis. There is a continuous loss of atoms from the cavity mode with time due to absence of the MOT cooling beams and collisions with background atoms present in the ambient vapor in the chamber. It is experimentally observed that the upward scan shows a larger normal mode splitting than the downward scan. This is due to a larger number of atoms present in the cavity mode in the upward scan than the downward scan. Further the absolute height of the peaks are higher in the downward scan due to lower absorption of the probe beam by atoms present in the cavity mode.

In our experiment, the cavity can stay around the resonance ($\geq 95\%$ of the peak transmission) for at least a couple of seconds before it slowly drifts away. This is a long enough time to record a sufficient number of the experimental measurements given the fact that the probe beam is scanning over the cavity resonance within 2 milliseconds. The empty cavity frequency is therefore not

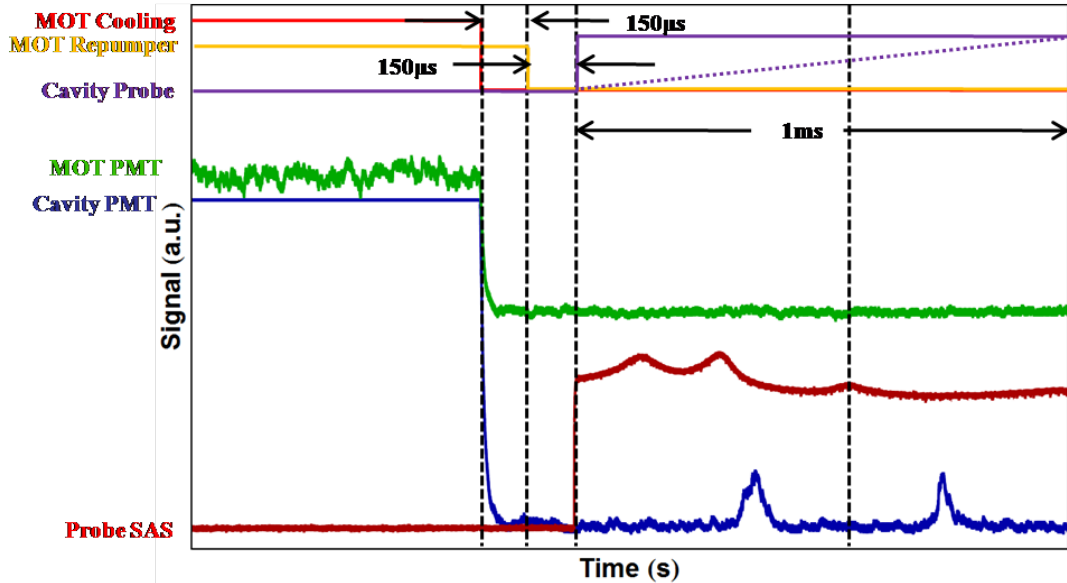


FIGURE 4.22: Only the upward scan of the probe beam is shown in the timing diagram since the relevant measurements for the normal mode splitting are inferred from the upward cycle of the probe scan. The red and the orange traces labeled ‘MOT Cooling’ and ‘MOT Repumper’ depict the switching OFF of the MOT cooling and MOT repumper beams respectively. The purple trace marked ‘Cavity Probe’ shows the switching ON of the probe beam along the cavity axis. The red trace marked ‘Probe SAS’ at the bottom of the figure shows the frequency reference derived from a saturated absorption spectroscopy set-up for the seed beam along the cavity axis. The green trace marked ‘MOT PMT’ shows the signal recorded on the PMT placed at the end of the MOT spatial filter assembly. The dark blue trace marked ‘Cavity PMT’ shows the two-peaked cavity transmission as recorded by a PMT for the upward scan of the probe/seed beam in frequency along the cavity axis.

actively locked to the atomic resonance during the measurements, but is periodically corrected for the frequency drifts. A schematic of the experimental sequence followed in time for the various TTL pulses used for the observation of Rabi splitting is shown in Fig. 4.22.

The observed normal mode splitting as a function of the atom number in the cavity mode is shown in Fig.4.23. We set the cavity frequency to $\Delta_c = 0$, where $\Delta_c = \omega_c - \omega_a$, and record the frequency separation of the lower coupled state from the bare atomic resonance $|F=3\rangle \rightarrow |F'=4\rangle$ as a function of the number of atoms. Here ω_c and ω_a represent respectively the cavity and the atomic frequency. The atom number in the cavity mode was varied between 10,000

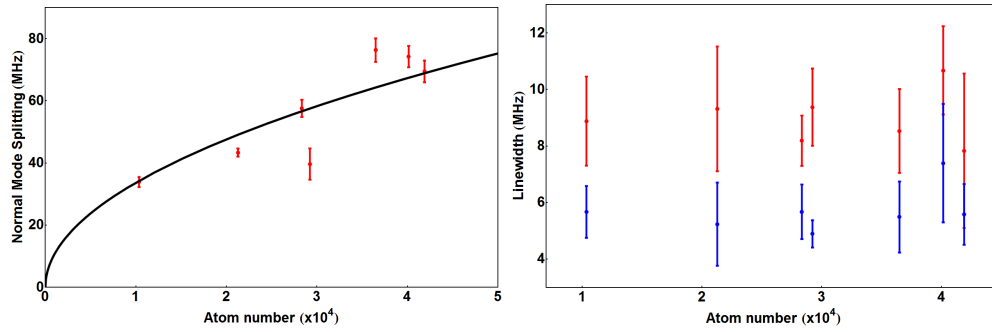


FIGURE 4.23: Left: The multi-atom normal mode splitting as a function of number of atoms present in the cavity mode. The experimental points with error bars are depicted with filled circles (red). The black trace is a square root fit to the data yielding an experimentally measured value of $g_{eff}=0.168\text{MHz}$. Right: The individual peak widths of the normal mode pair of peaks versus atom number is shown. The red points represent the width of the left peak while the blue points represent the width of the right peak for the normal mode pair of peaks.

and 45,000 by changing the MOT cooling and repumper beam intensity while the size of the cold cloud was determined from separately taken cold cloud images in conjunction with the spatially filtered MOT fluorescence signal on a PMT. The dependence of $|\Delta_p|$, where $\Delta_p = \omega_p - \omega_a$, on the number of atoms is well described by a square root, as expected from the Tavis–Cummings model [54]. Here ω_p represents the probe frequency. The cold Rubidium (Rb) atoms can be viewed as a two-level system for the probe laser and the cavity transmission shows a two peaked spectrum at $|\Delta_p| = \pm g_{eff}$ with the peak separation representing the multiatom normal mode (vacuum Rabi) splitting of the composite atom-cavity system.

We also record the width of individual peak for the normal mode pair of peaks versus atom number as shown in Fig.4.23. The full width at half maximum (FWHM) of individual peak for the normal mode pair is theoretically estimated to be $\approx (\kappa + \Gamma)/2$, where κ is the linewidth (FWHM) of the cavity and Γ the spontaneous emission lifetime (FWHM) of the atomic excited state. For our system, the FWHM of individual peak is estimated to be around $\frac{(1.58+6.06)}{2}$ MHz = 3.82MHz. Here 1.58MHz is the linewidth of the transmission peak

recorded when the probe beam is coupled into the cavity mode in the absence of atoms, while 6.06MHz is the natural linewidth of the $^{85}\text{Rb } 5^2\text{P}_{3/2} F'=4$ state. The observed FWHMs for the left and right peaks are $(8.97\pm 0.94)\text{MHz}$ and $(5.70\pm 0.79)\text{MHz}$ respectively. The increase in the width of the peaks can be due to various reasons. One of the reasons for the broadening of the peak at the lower frequency end may arise from the optical pumping into other Zeeman sub-levels of the transition being probed. Further the linewidth of the individual peaks may also depend on the intensity fluctuations arising from polarization instabilities of the single mode fiber that delivers the probe beam into the cavity [2, 55]. The asymmetry in the width of the left and right pair of peaks may arise from the mismatch in the respective detunings of the probe-atom detuning (Δ_p) and the atom cavity detuning (Δ_c) [2, 55]. The mismatch in the respective detunings arise from our inability to actively stabilize the cavity resonance to a desired frequency.

4.12 Conclusion

In this chapter we have essentially introduced the final design and detailed construction of the UHV system. We have characterized the optical cavity and introduced the ion trap with relevant numerical simulations providing the bench mark to characterize its operation. We have further demonstrated the capability of realizing a magneto-optical trap located at the center of the thin wire ion trap while simultaneously ensuring overlap with the spatial mode of the optical cavity. We have further characterized the emission of light from the cold trapped atoms in the MOT coupled into the low order modes of an optical cavity. We have investigated the possibility of line narrowing as a function of total number of atoms in the MOT. However we do not see any evidence of line narrowing reported in the work described in this thesis.

We have also explored the dynamics of the composite atom cavity system by

switching off the MOT repumper beam that depletes the source of light coupling into the cavity modes. In this aspect, we have characterized the timescales associated with the decay of atomic fluorescence as measured in the free space and along the cavity axis in both cases where the cavity is on and off resonance. We have seen that the timescales measured along the cavity axis are lower than those recorded for the free space. We have tried to give a qualitative model which tries to explain the timescales associated with the observations.

We have also demonstrated the ability of our system to enter the strong coupling regime of cavity QED (quantum electro-dynamics) by collective interactions of the atoms in the cavity mode. We have measured the normal mode splitting of the composite atom-cavity system and verified the square root dependence of the observed splitting with the number of atoms in the cavity mode. To conclude, we have built and characterized a versatile instrument comprising of a magneto-optical trap overlapping the mode of an optical cavity which is capable of simultaneously trapping multispecies atoms, ions and molecules given the physics goals laid out in the earlier portions of the chapter.

References

- [1] J. Ye and T. W. Lynn. Applications of optical cavities in modern atomic, molecular, and optical physics. *Advances in Atomic, Molecular, and Optical Physics*, edited by B. Bederson and H. Walther. Academic, Amsterdam, 2003, Vol. 49, p. 1.
- [2] Paul R. Berman. (edited) *Cavity quantum electrodynamics - Advances in atomic, molecular, and optical physics*. New York: Academic Press, (1994).
- [3] William D. Phillips and Harold Metcalf. Laser Deceleration of an Atomic Beam. *Phys. Rev. Lett.* 48, 596-599 (1982).
- [4] Paul D. Lett, Richard N. Watts, Christoph I. Westbrook, William D. Phillips, Phillip L. Gould, and Harold J. Metcalf. Observation of atoms laser cooled below the Doppler limit. *Phys. Rev. Lett.* 61, 169-172 (1988).
- [5] A. Aspect, E. Arimondo, R. Kaiser, N. Vansteenkiste and C. Cohen-Tannoudji. Laser cooling below the one-photon recoil energy by velocity-selective coherent population trapping. *Phys. Rev. Lett.* 61, 826-829 (1988).

-
- [6] C. Salomon, J. Dalibard, W. D. Phillips, A. Clairon and S. Guellati. Laser Cooling of Cesium Atoms below $3 \mu\text{K}$. *Europhys. Lett.* 12 (8), pp. 683-688 (1990).
- [7] E. L. Raab, M. Prentiss, Alex Cable, Steven Chu, and D. E. Pritchard. Trapping of Neutral Sodium Atoms with Radiation Pressure. *Phys. Rev. Lett.* 59, 2631-2634 (1987).
- [8] C. Monroe, W. Swann, H. Robinson, and C. Wieman. Very cold trapped atoms in a vapor cell. *Phys. Rev. Lett.* 65, 1571-1574 (1990).
- [9] C. N. Cohen-Tannoudji and W. D. Phillips. New mechanisms for laser cooling. *Phys. Today* 43(10), 33(1990).
- [10] W. D. Phillips. Laser cooling and trapping of neutral atoms. *Rev. Mod. Phys.* 70 (1998).
- [11] H. J. Metcalf & P. van der Straten. *Laser Cooling and Trapping*. Berlin: Springer (1999).
- [12] M. H. Anderson, J. R. Ensher, M. R. Matthews, C. E. Wieman and E. A. Cornell. Observation of Bose-Einstein Condensation in a Dilute Atomic Vapor. *Science* 269, 198 (1995).
- [13] K. B. Davis, M. O. Mewes, M. R. Andrews, N. J. van Druten, D. S. Durfee, D. M. Kurn, and W. Ketterle. Bose-Einstein Condensation in a Gas of Sodium Atoms. *Phys. Rev. Lett.* 75, 3969-3973 (1995).
- [14] C. C. Bradley, C. A. Sackett, J. J. Tollett, and R. G. Hulet. Evidence of Bose-Einstein Condensation in an Atomic Gas with Attractive Interactions. *Phys. Rev. Lett.* 75, 1687-1690 (1995).
- [15] B. DeMarco and D. S. Jin. Onset of Fermi Degeneracy in a Trapped Atomic Gas. *Science* 285, 1703 (1999).

-
- [16] Andrew G. Truscott, Kevin E. Strecker, William I. McAlexander, Guthrie B. Partridge and Randall G. Hulet. Observation of Fermi Pressure in a Gas of Trapped Atoms. *Science* 291, 2570 (2001).
- [17] Takeshi Fukuhara, Yosuke Takasu, Mitsutaka Kumakura and Yoshiro Takahashi. Degenerate Fermi Gases of Ytterbium. *Phys. Rev. Lett.* 98, 030401 (2007).
- [18] J. D. Weinstein, R. deCarvalho, T. Guillet, B. Friedrich and J. M. Doyle. Magnetic trapping of calcium monohydride molecules at millikelvin temperatures. *Nature* 395 148-150 (1998).
- [19] S. Inouye, M. R. Andrews, J. Stenger, H-J Miesner, D. M. Stamper-Kurn and W. Ketterle. Observation of Feshbach resonances in a Bose-Einstein condensate. *Nature* 392, 151 (1998).
- [20] H. L. Bethlem, G. Berden and G. Meijer. Decelerating neutral dipolar molecules. *Phys. Rev. Lett.* 83, 1558-1561 (1999).
- [21] J. Weiner, V. S. Bagnato, S. Zilio and P. S. Julienne. Experiments and theory in cold and ultracold collisions. *Rev. Mod. Phys.* 71, 1 (1999).
- [22] E. A. Donley, N. R. Claussen, S. T. Thompson and C. E. Wieman. Atom-molecule coherence in a Bose-Einstein condensate. *Nature* 417, 529 (2002).
- [23] J. Herbig, T. Kraemer, M. Mark, T. Weber, C. Chin, H-C. Nagerl and R. Grimm. Preparation of a pure molecular quantum gas. *Science* 301, 1510 (2003).
- [24] S. Jochim, M. Bartenstein, A. Altmeyer, G. Hendl, S. Riedl, C. Chin, J. Hecker Denschlag and R. Grimm. Bose-Einstein condensation of molecules. *Science* 302, 2101 (2003).

-
- [25] M. Greiner, C. A. Regal and D. S. Jin. Emergence of a molecular Bose-Einstein condensate from a Fermi gas. *Nature* 426, 537 (2003).
- [26] C. A. Regal, C. Ticknor, J. L. Bohn and D. S. Jin. Creation of ultracold molecules from a Fermi gas of atoms. *Nature* 424, 47 (2003).
- [27] M. W. Zwierlein, C. A. Stan, C. H. Schunck, S. M. F. Raupach, S. Gupta, Z. Hadzibabic and W. Ketterle. Observation of Bose-Einstein condensation of molecules. *Phys. Rev. Lett.* 91, 250401 (2003).
- [28] J. M. Sage, S. Sainis, T. Bergeman and D. DeMille. Optical production of ultracold polar molecules. *Phys. Rev. Lett.* 94, 203001 (2005).
- [29] T. Khler, K. Gral and P. S. Julienne. Production of cold molecules via magnetically tunable Feshbach resonances. *Rev. Mod. Phys.* 78, 1311 (2006).
- [30] K. M. Jones, E. Tiesinga, P. D. Lett and P. S. Julienne. Ultracold photoassociation spectroscopy: long-range molecules and atomic scattering. *Rev. Mod. Phys.* 78, 483 (2006).
- [31] K-K Ni, S. Ospelkaus, M. H. G. de Miranda, A. Pe'er, B. Neyenhuis, J. J. Zirbel, S. Kotochigova, P. S. Julienne, D. S. Jin and J. Ye. A high phase-space-density gas of polar molecules. *Science* 322, 231 (2008).
- [32] G. Rempe, R. J. Thompson, H. J. Kimble, and R. Lalezari. Measurement of ultralow losses in an optical interferometer. *Opt. Lett.* 17, 363-365 (1992).
- [33] Christina J. Hood, H. J. Kimble and Jun Ye. Characterization of high-finesse mirrors: Loss, phase shifts, and mode structure in an optical cavity. *Phys. Rev. A.* 64, 033804 (2001).
- [34] H. J. Carmichael and B. C. Sanders. Multiatom effects in cavity QED with atomic beams. *Phys. Rev. A* 60, 2497-2504 (1999).

-
- [35] B. Nagorny, Th. Elsasser and A. Hemmerich. Collective atomic motion in an optical lattice formed inside a high finesse cavity. *Phys. Rev. Lett.* 91, 153003 (2003).
- [36] A. T. Black, H. W. Chan and V. Vuletic. Observation of collective friction forces due to spatial self-organization of atoms: from Rayleigh to Bragg scattering. *Phys. Rev. Lett.* 91, 203001 (2003).
- [37] S. Slama, S. Bux, G. Krenz, C. Zimmerman and Ph. W. Courteille. Superradiant Rayleigh scattering and collective atomic recoil lasing in a ring cavity. *Phys. Rev. Lett.* 98, 053603 (2007).
- [38] K. Baumann, C. Guerlin, F. Brennecke and T. Esslinger. Dicke quantum phase transition with a superfluid gas in an optical cavity. *Nature* 464, 1301-1306 (2010).
- [39] Peter Horak, Bruce G. Klappauf, Albrecht Haase, Ron Folman, Jorg Schmiedmayer, Peter Domokos and E. A. Hinds. Possibility of single-atom detection on a chip. *Phys. Rev. A* 67, 043806 (2003).
- [40] M. Trupke, E. A. Hinds, S. Eriksson, E. A. Curtis, Z. Moktadir, E. Kukharenska, and M. Kraft. Microfabricated high-finesse optical cavity with open access and small volume. *Appl. Phys. Lett.* 87, 211106 (2005).
- [41] Igor Teper, Yu-ju Lin, and Vladan Vuletic. Resonator-Aided Single-Atom Detection on a Microfabricated Chip. *Phys. Rev. Lett.* 97, 023002 (2006).
- [42] Roger Gehr, Jurgen Volz, Guilhem Dubois, Tilo Steinmetz, Yves Colombe, Benjamin L. Lev, Romain Long, Jrme Estve, and Jakob Reichel. Cavity-Based Single Atom Preparation and High-Fidelity Hyperfine State Readout. *Phys. Rev. Lett.* 104, 203602 (2010).
- [43] J. Bochmann, M. Mucke, C. Guhl, S. Ritter, G. Rempe, and D. L.

- Moehring. Lossless State Detection of Single Neutral Atoms. *Phys. Rev. Lett.* 104, 203601 (2010).
- [44] J. Goldwin, M. Trupke, J. Kenner, A. Ratnapala and E.A. Hinds. Fast cavity-enhanced atom detection with low noise and high fidelity. *Nat. Commun.* 2:418 doi: 10.1038/ncomms1428 (2011).
- [45] R. J. Thompson, G. Rempe and H. J. Kimble. Observation of normal mode splitting for an atom in an optical cavity. *Phys. Rev. Lett.* 68, 1132-1135 (1992).
- [46] J. J. Childs, K. An, M. S. Otteson, R. R. Dasari and M. S. Feld. Normal mode line shapes for atoms in standing-wave optical resonators. *Phys. Rev. Lett.* 77, 2901-2904 (1996).
- [47] Gessler Hernandez, Jiepeng Zhang, and Yifu Zhu. Vacuum Rabi splitting and intracavity dark state in a cavity-atom system. *Phys. Rev. A* 76, 053814 (2007).
- [48] J. Kleinert, C. Haimberger, P. J. Zabawa, and N. P. Bigelow. Manufacturing a thin wire electrostatic trap for ultracold polar molecules. *Rev. Sci. Instrum.* 78, 113108 (2007).
- [49] G. S. Agarwal and P. K. Pathak. dc-field-induced enhancement and inhibition of spontaneous emission in a cavity. *Phys. Rev. A* 70, 025802 (2004).
- [50] Claude Cohen-Tannoudji, Bernard Diu und Franck Laloe. *Quantum Mechanics*. Wiley-Interscience. 2006.
- [51] Serge Haroche and Jean-Michel Raimond. *Exploring the Quantum : Atoms, Cavities and Photons* (Oxford University Press Inc., New York).
- [52] E. M. Purcell. Spontaneous emission probabilities at radio frequencies. *Phys. Rev.* 69, 681 (1946).

- [53] Peter Horak, Bruce G. Klappauf, Albrecht Haase, Ron Folman, Jorg Schmiedmayer, Peter Domokos and E. A. Hinds. Possibility of single-atom detection on a chip. *Phys. Rev. A* 67, 043806 (2003).
- [54] M. Tavis and F. W. Cummings. Exact solution for an N-molecule radiation-field Hamiltonian. *Phys. Rev.* 170, 379384 (1968).
- [55] J. Gripp, S. L. Mielke, and L. A. Orozco. Evolution of the vacuum Rabi peaks in a detuned atom-cavity system. *Phys. Rev. A.* 56, 3262-3273 (1997).

5

Conclusion

5.1 Summary

In this thesis we present experiments that investigate the interaction of atoms with resonant light utilizing an optical cavity. The cavity is envisioned as a frequency sensitive detector at low light levels. The physics of interactions between atoms (either at room temperature or in the cold regime) and optical cavities of varying finesse, in both the steady state and transient regime, has been discussed and presented in this thesis. A cavity could enable frequency sensitive, non-destructive detection of molecular states by coupling the weak molecular fluorescence over and above the atomic fluorescence, if any, to the mode of the cavity. Experiments with cold atoms interacting with optical cavity modes is a precursor to the experiments to be done with cold molecules in the near future. The experiments reported in this thesis form the key towards our objective of utilizing the optical cavity as a low light level, frequency sensitive detector.

The first chapter motivates the study of experiments that have been reported in this thesis. A few of the long standing issues in the field of cold molecules are the techniques to synthesize cold molecules from cold atoms in large numbers, trapping these molecules for long enough time to conduct useful experimentation and lastly detection of cold molecules. In this context, our goal was to build a hybrid trapping apparatus that enables us to form, trap and detect molecules from cold atoms. Given the problems associated with the detection of molecules in low numbers using conventional imaging techniques such as spatial filtering, we highlight the possibility of using of an optical cavity that could enable the frequency sensitive detection of molecules in low numbers. We then provide a background of low atom number detection using cavities in the context of the Purcell effect. We provide a very brief overview of atom cavity experiments that have been conducted using both hot and cold atoms. We describe briefly the state of the art experiments that have demonstrated low atom number detection utilizing optical cavities in this context. We then outline the physics problems that were investigated in improving our understanding of the atom-cavity system. We finally discuss briefly the experimental investigation of atom-cavity interactions at room temperature and the cold regime.

The second chapter contains a review of the theoretical tools necessary for the experiments reported in this thesis. We start with the basic description of an optical cavity and introduce and explain the physical significance of the terms like finesse, free spectral range, quality factor, etc. of an optical cavity. We next discuss the physical origin of the eigen-modes of a resonator. We then introduce the concept of higher order modes that can be realized in an optical cavity and discuss origin and significance of the Hermite-Gaussian and Laguerre-Gaussian modes in this context. We then move into the atom-cavity interactions and discuss the Jaynes-Cummings model in the context of the quantum theory of a two level atom interacting with a field of a single cavity mode. Using the Jaynes-Cummings model we describe the interaction of a

single atom located at the center of a single mode cavity in both the ideal and in the dissipative regime using an analytical approach. Following this we move into the atomic physics segment for the remaining portion of the chapter. We discuss briefly the atomic properties of the Rubidium (Rb) atom and explain the origin of resolving the spectral lines of Rb using saturated absorption spectroscopy. We then describe the interaction of atoms with static magnetic fields that gives rise to Zeeman effects. We next describe atoms interacting with an external laser field that gives rise to coherent and incoherent processes. In this context we discuss the optical Bloch equations for a two level atom interacting with an external light field. Following this we discuss the AC Stark shifts that arise when the atomic energy levels are perturbed by the electric field of the external light field. We next discuss the spontaneous force that acts on an atom as a result of the incoherent process mentioned earlier. We then discuss the physics of laser cooling and optical molasses and finally conclude with the magneto-optical trap.

The third chapter is documented in the following manner. As a precursor to performing the actual experiments with cold atoms in ultra high vacuum conditions, we tried to see whether we could stimulate light from atoms in a room temperature vapor cell to couple into a cavity mode. In this aspect, we first describe the relevance and context of the experiments reported using a vapor cell placed inside an optical cavity at room temperature. We then briefly review previous research on all optical switches. In the next section we introduce the experimental apparatus, describe the cavity characterization and optical system set-up relevant for negative logic switching, follow it up with the experiments performed in relation to the negative logic switching and conclude with results and discussions. Both steady state and transient changes in the transmitted intensity are recorded for both cases of operation. Following this

we shall present the experimental set-up and results for positive logic switching and compare the results with the negative logic switching experiments discussed in the previous section. In the next section we discuss the physical process behind the operation of the switching mechanism by invoking a simple model. Finally we conclude by discussing the results of both switching experiments in the context of all optical switching utilizing a vapor cell encompassed within an optical cavity.

To summarize, we have demonstrated an all optical switching phenomena in transmission utilizing a Rubidium vapor cell enclosed within a Fabry-Perot cavity. The cavity probe light can be completely extinguished by the control intensity, a fact which is used to demonstrate high fidelity switching of transmitted light through this system. The control light exhibits a threshold power, above which it alters the transmission properties of the cavity. Both steady state and transient processes are experimentally characterized for this system for two different approaches of realizing the optical switch. The physics of this system is discussed within the context of a driven four level system and estimates for the long time scales observed in the transient phenomena are provided using a qualitative model. The key features of this switch are as follows:

- a. The switch operates at close to half the telecom wavelength (1550nm).
- b. The switching mechanism is robust and alignment insensitive.
- c. The power of control light required to affect the transmitted intensity of the resonant seed light through the cavity is shown to be very small.
- d. The all optical switch has no qualitative dependence on the polarization of the probe and switching beams.
- e. The switching mechanism does not require elaborate frequency stabilization of either the cavity resonances or the probe and control fields to relevant atomic transitions to realize the switch.

The fourth chapter is organized in the following manner. We introduce the context and relevance of optical cavities in exploring cold and ultracold molecule formation, cold atom - cold ion interaction and ofcourse the rich physics that can be explored using only cold atoms itself. We next project clearly the physics goals that are of primary interest and the technological issues that need to be addressed in order to realize the stated physics objectives. In the following section we describe the design and construction of the UHV chamber housing the experiment. We point out the key components that have been incorporated to address the physics goals that we want to address. Following this is the subsection where we describe in detail the design, mounting, alignment and characterization of the optical Fabry-Perot cavity, which is the key tool for the experimental observations reported in this chapter. In the next subsection we discuss very briefly the design and construction of the thin wireframe trap that has been mounted overlapping the mode of the optical cavity. We then discuss in detail about the characterization of the spatial filter assembly to detect and image cold atoms in the MOT. We also discuss the imaging set-up developed for detecting light out of the cavity. In the following section we shall move into characterizing the magneto-optical trap (MOT) realized experimentally in the UHV system constructed by us and follow it up with a description of the experimental realization of coupling light from cold atoms trapped in the MOT into cavity modes. Next we focus on the dynamics of atomic population by a periodic modulation on the MOT repumper beam as measured by the photo-multiplier tubes (PMTs) placed along the cavity axis in transmission and the spatial filter assembly to pick up fluorescence from trapped atoms in the MOT. In the next section we shall try to explain qualitatively the dynamics of the atomic population measured by the PMT along the MOT spatial filter axis by an effective simplified four level system using a density matrix approach. Following this section is we shall try to give a qualitative understanding of the

dynamics of the composite atom cavity system using a simplified system of a two level atom in a cavity for the experimental observations. After the discussion on the above two qualitative models, we shall demonstrate the realization of collective strong coupling achieved in the composite atom cavity system through the experimental observation of normal mode splitting for cold atoms trapped in the MOT and located at the mode of the optical cavity. Finally we conclude by summarising the experiments and observations reported in this chapter.

5.2 Future Directions

An interesting problem to address in future in the context of atom-cavity interactions is the possibility of estimating the temperature of cloud of cold atoms trapped in the magneto-optical trap at the center of the cavity. One may use the normal mode splitting to estimate the number of atoms present in the cavity mode. The number of atoms in the cavity mode would decay with time given the fact that the cold cloud starts expanding once the MOT cooling and beams are turned off using acousto-optic modulators (AOMs). Given an initial temperature T of the cold cloud, the rate of expansion of the cold cloud with time can be mapped using the number of atoms present in the cavity mode estimated from the normal mode splitting. One may then compare and contrast the value of temperature obtained by this method with standard temperature measurement protocols such as the release and re-capture method or the time of flight (TOF) method.

Another interesting problem using cold atoms within the optical cavity would be to investigate the changes in the normal mode spectrum of the composite atom-cavity system under the influence of strong static electric fields. As per our initial simulations on the strength of electric field that can be obtained

with the thin wireframe trap, the changes in the normal mode splitting is expected to be ≈ 1 MHz for an electric field gradient of 2kV/cm. This study would be useful in the context of trapping cold polar molecules by static electric fields.

One may also explore the possibility of utilizing the cavity towards production of cold molecules from cold atoms using photo-association techniques. Since the rate of photo-association depends on the intensity of the photo-associating light, one may investigate the changes in the rate of photo-association using light in the cavity mode as compared to photo-association in free space. The intra-cavity intensity is enhanced by a factor $2F/\pi$, where F is the cavity finesse. Thus one may expect to see significant difference in photo-association rates if the photo-association experiment is carried out using the light build-up in the cavity mode.